

An oceanographic study of the cavity beneath the  
McMurdo Ice Shelf, Antarctica.

by

Natalie J. Robinson

Submitted in fulfilment of the  
requirements  
for the degree of  
Master of Science  
in  
Geophysics

Victoria University of Wellington, New Zealand

November 2004



Figure 1: 5am Tutorial

## Abstract

This thesis reports the first observations of currents, temperature and salinity beneath the McMurdo Ice Shelf, Antarctica. They are reviewed and discussed here in conjunction with results of a numerical modelling study used to simulate current flow and to investigate local sediment deposition. The McMurdo Ice Shelf lies behind Ross Island off the Victoria Land coast of Antarctica, and represents the northwest corner of the much larger Ross Ice Shelf. The site will be drilled by the ANDRILL consortium in 2006, passing through the ice shelf, the water column, and 1000 m into the sea floor, to obtain a record of ice shelf and climate history in this area.

This study stems from a site survey carried out in early 2003, for which access holes were melted at two locations on the McMurdo Ice Shelf. Current meters surveyed multiple depths simultaneously during spring tides, and profiles of temperature and salinity were collected through a diurnal tidal cycle at each site. Maximum currents were recorded in the boundary layer at the base of the ice shelf, reaching  $0.22 \text{ m s}^{-1}$  during the flood tide. The salinity and temperature profiles were similar at the two sites, with greater temporal variability observed at the site closer to the open water of McMurdo Sound. Supercooling, due to the pressure-dependence of the *in-situ* freezing temperature, was observed at one of the sites. At the second site, where the draft of the ice shelf was deeper, temperatures corresponding to basal melting were observed.

At a third site on the sea ice at the northwestern edge of the McMurdo Ice Shelf, a current meter surveyed the water column to 320 metres below sea level for 23 days. This allowed comparison of current behaviour through spring and neap tides, and between sub-sea ice and sub-ice shelf environments in the same season. Net throughflow over spring tides at each of the three sites was consistent with transport eastwards from McMurdo Sound along the channel defined by local bathymetry. Profiles of temperature and salinity from beneath the ice shelf were likewise consistent with McMurdo Sound being the source of the observed water masses.

Flow along the sub-ice shelf channel was further investigated using an adaptation of a two-dimensional thermohaline ocean model. Year-long profiles of temperature and salinity from southern McMurdo Sound were used to seasonally force the model, resulting in

---

annual variation in all parameters. The rate of melting decreased monotonically from  $\sim 0.6 \text{ m yr}^{-1}$  at the deep end of the ice shelf, into a region of freezing associated with supercooling closer to the McMurdo Sound end of the domain. This change in regime mirrored the observations from the boundary layer beneath the McMurdo Ice Shelf.

Sediment transport and deposition were investigated, with settling velocities used to represent sediment sizes ranging from biogenic pellets and fine sand through algal flocs to fine mud, particle types known and described from the present day environment. This method of incorporating sedimentation processes gave results similar to observations from surface sediment cores collected beneath the ice shelf. The larger grains were preferentially deposited close to the open water McMurdo Sound source, whereas fine-grained material was entrained into the general circulation and deposited by regions of down-welling. A settling velocity of  $\sim 1 \times 10^{-4} \text{ m s}^{-1}$ , corresponding to a grain size of  $\sim 5 \mu\text{m}$ , defined the boundary between these depositional behaviours.

Characteristics of the water beneath the ice shelf suggest that it had been transported from McMurdo Sound, being modified through interaction with the base of the ice shelf. This pattern of throughflow was also seen in the current meter data, with a strong tidal signal throughout the water column superimposed on the net transport eastward from McMurdo Sound and under the ice shelf. This net flow pattern was supported by the results of the longer-term simulation experiments.

---

## Acknowledgements

Funding for this project was made available through the FoRST grant ‘Antarctic Climate Evolution - Drivers and Consequences’. Logistical support and tidal height data were provided by Antarctica New Zealand.

I have thoroughly enjoyed the time I have spent working on this project, and am grateful for the opportunities afforded me during its course. I wish to thank my supervisors Peter Barrett, Mike Williams and Mark McGuinness, for continually supporting me and getting me past the frustrating bits.

I would like to thank the other members of the Antarctic Research Centre, in particular Alex and Tamsin, for the friendly and productive atmosphere as well as their readiness to answer my questions and help me out wherever possible.

I would also like to thank Lionel Carter, Gavin Dunbar, Steve Monismith and Rob Dunbar for help they’ve given me along the way.

Finally I’d like to thank my parents and my husband for their love and support.

# Contents

<b>1</b>	<b>Introduction</b>	<b>1</b>
<b>2</b>	<b>Data analysis - background</b>	<b>6</b>
2.1	Circulation of McMurdo Sound . . . . .	6
2.1.1	Eastern McMurdo Sound . . . . .	8
2.1.2	Western McMurdo Sound . . . . .	9
2.2	Data collection - Windless Bight, 2003 . . . . .	10
<b>3</b>	<b>Current profile measurements</b>	<b>13</b>
3.1	Sea ice site . . . . .	13
3.2	Ice shelf site #1 - HWD-1 . . . . .	17
3.3	Ice shelf site #2 - HWD-2 . . . . .	22
3.4	General circulation at Windless Bight . . . . .	27
<b>4</b>	<b>Profiles of water characteristics</b>	<b>30</b>
4.1	Ice shelf site #1 - HWD-1 . . . . .	31
4.2	Ice shelf site #2 - HWD-2 . . . . .	35
4.3	Comparison between ice shelf sites and with historical sites . . . . .	39
4.3.1	Profiles at ice shelf sites compared to profiles nearby . . . . .	40
<b>5</b>	<b>Modelling and sedimentation studies beneath Antarctic ice shelves</b>	<b>43</b>
5.1	Description of sub-ice shelf processes . . . . .	44
5.2	Modelling the sub-ice shelf environment . . . . .	45
5.2.1	Supply of mechanical energy . . . . .	45
5.2.2	Prescribed boundary conditions . . . . .	47
5.2.3	Importance of prescribed topography . . . . .	48
5.2.4	Application to McMurdo Ice Shelf at Windless Bight . . . . .	49
5.3	Present sedimentation environment . . . . .	49

---

<b>6</b>	<b>Modelling the thermohaline circulation beneath the McMurdo Ice Shelf</b>	<b>52</b>
6.1	Sub-ice shelf circulation at Windless Bight . . . . .	52
6.1.1	Model description . . . . .	53
6.1.2	Model configuration . . . . .	58
6.1.3	Spin-up phases . . . . .	61
<b>7</b>	<b>Model experimentation</b>	<b>62</b>
7.1	Sensitivity analysis - model dynamics . . . . .	62
7.1.1	Standard settings . . . . .	63
7.1.2	Adjusting horizontal grid size . . . . .	65
7.1.3	Adjusting the timestep length . . . . .	66
7.1.4	Adjusting horizontal diffusion on active tracers . . . . .	70
7.1.5	Summary . . . . .	71
7.2	Sensitivity analysis - sedimentation environment . . . . .	72
7.2.1	Standard settings . . . . .	73
7.2.2	Adjusting initial conditions . . . . .	75
7.2.3	Adjustments to the open boundary source . . . . .	77
7.2.4	Scale of model domain - changing $\Delta Y$ . . . . .	77
7.2.5	Grain size - settling velocity . . . . .	79
7.2.6	Summary and final tests . . . . .	80
7.3	Seafloor configuration experiments . . . . .	81
7.3.1	General features of circulation . . . . .	82
7.3.2	Sedimentation environment . . . . .	86
7.3.3	Conclusions . . . . .	90
<b>8</b>	<b>Summary of this study and comparison of methods</b>	<b>93</b>
8.1	Analysis of data from study sites . . . . .	94
8.2	Modelling study . . . . .	96
8.3	Comparison of methods . . . . .	98
<b>A</b>	<b>Formulation of numerical model</b>	<b>101</b>
A.1	Derivation of vorticity equation in 2-dimensions . . . . .	101
A.2	Extension of two-dimensional channel flow to allow net transport . . . . .	102
A.3	Calculating $\gamma(t)$ - net throughflow . . . . .	104
<b>B</b>	<b>Velocity profiles report</b>	<b>107</b>

<b>C Index of model simulations on CD</b>	<b>141</b>
<b>References</b>	<b>142</b>

# List of Figures

1	5am tutorial . . . . .	i
1.1	Map of McMurdo Sound region . . . . .	2
1.2	Satellite image of Ross Island and B15A . . . . .	3
2.1	McMurdo Sound region with locations of current meter stations . . . . .	7
2.2	Windless Bight area with locations of K042 mooring sites . . . . .	10
2.3	Array of instruments at the two HWD sites . . . . .	11
3.1	Eastwards component of velocity at Sea Ice Site . . . . .	15
3.2	Northwards component of velocity at Sea Ice Site . . . . .	16
3.3	Eastwards component of velocity at HWD-1 . . . . .	18
3.4	Northwards component of velocity at HWD-1 . . . . .	19
3.5	Correlation of $V_e$ from three ADCPs at HWD-1 . . . . .	20
3.6	Correlation of $V_n$ from three ADCPs at HWD-1 . . . . .	21
3.7	Eastwards component of velocity at HWD-2 . . . . .	24
3.8	Northwards component of velocity at HWD-2 . . . . .	25
3.9	Correlation of $V_e$ from three ADCPs at HWD-2 . . . . .	26
3.10	Correlation of $V_n$ from three ADCPs at HWD-2 . . . . .	27
4.1	Timing of hydrological casts at HWD-1 . . . . .	31
4.2	Salinity profiles from HWD-1 . . . . .	32
4.3	Potential temperature profiles from HWD-1 . . . . .	33
4.4	Timing of hydrological casts at HWD-2 . . . . .	36
4.5	Salinity profiles from HWD-2 . . . . .	37
4.6	Potential temperature profiles from HWD-2 . . . . .	38
4.7	Salinity and temperature data from HWD sites and neighbouring sites . . . . .	42
5.1	Map of Antarctica showing the ice shelves . . . . .	43
5.2	Schematic representation of 2-D thermohaline circulation cell . . . . .	44

---

6.1	Map of the McMurdo Ice Shelf showing section of channel modelled . . . . .	53
6.2	Monthly temperature profiles used to seasonally force the model . . . . .	54
6.3	Monthly salinity profiles used to seasonally force the model . . . . .	55
6.4	Flux of heat and salt at the ice-ocean boundary . . . . .	57
6.5	Placement of variables in model domain . . . . .	59
6.6	Standard configuration of seafloor and ice shelf . . . . .	59
7.1	Streamfunction plots from simulation with standard settings . . . . .	64
7.2	$\gamma(t)$ over five year seasonal forcing with different values for $\Delta Y$ . . . . .	65
7.3	Salinity and temperature for simulation with $\Delta Y$ set to 4000 m . . . . .	67
7.4	Streamfunction and temperature for simulation with $\Delta Y$ set to 10,000 m . . . . .	68
7.5	$\gamma(t)$ over five year seasonal forcing with different values for $\Delta T$ . . . . .	70
7.6	Sediment concentrations for standard experiment . . . . .	75
7.7	Sediment accumulation patterns for sand and fine mud sediment . . . . .	76
7.8	Fine mud concentrations: sediment supplied near seafloor . . . . .	78
7.9	Fine mud concentrations: four seasons with $\Delta Y = 10$ km. . . . .	80
7.10	The four domain configurations used in seasonal forcing experiments . . . . .	82
7.11	Plots of variables from standard seasonal forcing experiment . . . . .	83
7.12	Variables from configuration with Basin seafloor . . . . .	85
7.13	Sediment deposition patterns from configuration with flat seafloor . . . . .	88
7.14	Sediment deposition patterns from configuration with basin seafloor . . . . .	88

# Chapter 1

## Introduction

Sediment cores recovered from a number of sites around the Antarctic have revealed the significance of this isolated continent to global climate, and to future climate change (Barrett, 1996). Continuing a 30-year history of detailed study of climate history from offshore drilling, ANtarctic Geological DRILLing (ANDRILL <http://andrill-server.unl.edu>), a multi-national undertaking, will occupy and drill a number of sites around Antarctica. Drilling at the first site, beneath the McMurdo Ice Shelf at Windless Bight, is planned for the 2005-06 summer season.

The attraction of the Windless Bight site is the deep basin formed from the depression of the crust under the weight of Ross Island. It is the most significant feature of the bathymetry there, and has been slowly filling with sediment since its formation. It is hoped that by drilling this record, known to be as thick as 1.2 km in places (Horgan et al., in press), a high-resolution record of the area's climate history can be recovered. The advance and retreat of the ice shelf, marked by changes in the characteristics of the sedimentary layers, is expected to be the most significant signal identified.

Adequate knowledge of the present day ocean circulation is necessary for the interpretation of the record preserved in the layers of deposited material. Of particular importance is relating the flow at the site to regional, and larger, circulation patterns. Direct, simultaneous observations of multiple levels of flow have not previously been made for the ocean cavities beneath any of the Antarctic ice shelves. This means that the understanding of the circulation, which is likely to be significantly influenced by the presence of the ice shelf, is incomplete.

Direct observation of the currents around Ross Island have previously been restricted to

the open water north of the McMurdo and Ross Ice Shelves. Flow beneath the McMurdo Ice Shelf has been surmised from properties of the water exiting into the open water. Current meters have not previously been deployed beneath the McMurdo Ice Shelf, so the cavity represents a significant gap in the knowledge of the overall circulation around Ross Island, which this project aims to fill. Due to logistical considerations, this study was restricted to a short period, timed to match the season for the intended site occupation by the ANDRILL project. The data were collected from two sites on the McMurdo Ice Shelf (see fig. 1.1) during January and early February of 2003.

Multiple levels of data were collected simultaneously from the ocean cavity beneath the McMurdo Ice Shelf. Profiles of temperature and salinity were collected through the access holes created for deploying the current meters. A third study site, on the sea ice at the northern edge of the McMurdo Ice Shelf, was occupied to allow connection between the

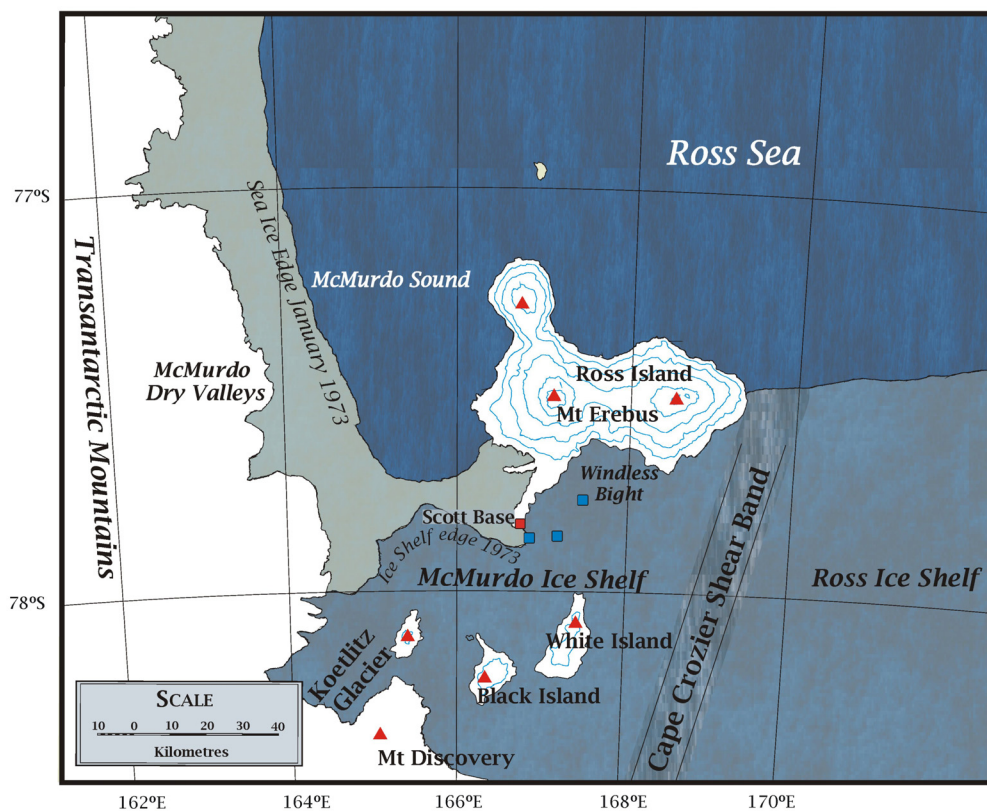


Figure 1.1: McMurdo Sound region showing various locations mentioned in text. Study sites from January 2003 are shown with blue squares (see also figures 2.1 and 2.2) The ‘Cape Crozier Shear Band’ defines the boundary between the McMurdo and Ross Ice Shelves (Whillans and Merry, 1996).

---

new sub-ice shelf observations and the previously studied area of McMurdo Sound. This also allowed comparison between the sub-ice shelf and sub-sea ice environments in the same season.

Data from the three study sites will be described within the context of previous studies in the open water north of the Ross and McMurdo Ice Shelves. The temporal and spatial extent of the study will be increased through the use of a two-dimensional model to represent flow in a channel beneath an ice shelf. The model will also be used to investigate the depositional environment for sediment beneath the ice shelf, with sediment added to the circulation from sources at McMurdo Sound and at the base of the ice shelf.

2003 was a year of unusual ice conditions in McMurdo Sound and the southern Ross Sea, brought about by the presence of the iceberg B15A which grounded north of Ross Island in July 2001 (see fig. 1.2). The possibility that the observed currents were atypical because of the presence of the iceberg is beyond the scope of this study, but has inter-



Figure 1.2: Satellite image of McMurdo Sound region showing the size and location of the iceberg B15A on 27 January 2003, during the time that the study sites at Windless Bight were occupied. Image courtesy of NASA Visible Earth <http://visibleearth.nasa.gov>.

---

esting potential for future study. Calving on the scale which produced B15 and others is expected to occur every 50-100 years (MacAyeal et al., 2002). While infrequent, it is a normal event necessary for maintaining the equilibrium conditions of the Ross Ice Shelf.

## **Thesis outline**

*Chapter 2* outlines the present knowledge of the local circulation from a variety of study types. These include direct current measurements, temperature and salinity measurements as well as biological evidence for sources of the water masses observed there.

In this study, currents were directly observed in front of the ice shelf and beneath the ice shelf using instruments capable of surveying multiple depths simultaneously. The analysis of these data sets is given in *Chapter 3*, followed by a description of the net flow under the McMurdo Ice Shelf from the current meter data. This chapter also includes a comparison of the flow regime for spring and neap tides at the edge of the ice shelf.

Profiles of temperature and salinity were collected from each of the sites on the McMurdo Ice Shelf. These are analysed for layering and variation over a diurnal tidal cycle in *Chapter 4*. The final section of this chapter compares the characteristics beneath the ice shelf with profiles from either side of Ross Island, as well as from deep under the Ross Ice Shelf.

The second major aspect of this study is the extension of the temporal and spatial scope by simulating the sub-ice environment. This is achieved using a two-dimensional model, for which the primary driver of circulation is the thermohaline interaction between the ice shelf and ocean beneath. In this way, several years of variation in a 40-km-long segment of the channel under the McMurdo Ice Shelf can be surveyed. Seasonal forcing is applied using independent, year-long profiles of temperature and salinity from McMurdo Sound. Sediment entrainment and deposition is incorporated as an independent, passive tracer.

*Chapter 5* outlines the various types of modelling currently in use for investigating sub-ice shelf ocean regimes around Antarctica. As part of this chapter a brief overview of the main features of the present sedimentation environment in McMurdo Sound and the Ross Sea is presented.

---

One of the models (Hellmer and Olbers, 1991) is adapted to the McMurdo Ice Shelf environment, with the main component of flow assumed to be along a two-dimensional curved channel of length 40 km. *Chapter 6* describes the formulation of the model, its setup and details of model spinup.

The specific problem for which the model was adapted is described in *Chapter 7*, as well as experiments to test the adapted model's sensitivity to the various parameters. Tests of the model's sedimentation environment, which were run in order to tune towards the present situation, are also described. With understanding of the model's behaviour based on these tests, seasonal forcing experiments were run for seven years of model time with four different domain configurations. Results of these final tests are described in this chapter, including the response of the model dynamics, and the effects on the depositional environment.

The final chapter, *Chapter 8*, summarizes the results from both parts of the study, and brings them together in the context of the regional ocean circulation. The observations of flows beneath the ice shelf, as well as the temperature and salinity profiles, are described with reference to historical observations from nearby sites. Model performance is compared to other sub-ice shelf ocean models, as well as to the observations from the same location. This comparison includes both the current flow and the behaviour of temperature and salinity. The sedimentation environment within the model is described and compared to the short surface sediment cores recovered from the sites on the ice shelf.

*Appendix A* describes the derivation of the vorticity equation from horizontal density gradients within the model, including assumptions involved in restricting flow to two dimensions. This appendix also describes the use and calculation of  $\gamma(t)$ , the net through-flow, which connects the circulation to the pressure gradient between the ends of the domain. *Appendix B* is the presentation of a report on observed velocity profiles from the Windless Bight sites and additional sites at Granite Harbour. This report was created for the design and safe operation of the sea riser which forms the basis of the ANDRILL project. Animations of some of the model experiments, and a full electronic version of this thesis, are on the CD inside the back cover.

# Chapter 2

## Data analysis - background

Due to the difficulties of accessing the ocean beneath the McMurdo Ice Shelf, the circulation within this ocean cavity and the associated sediment depositional environment are not well-understood. Since the area is expected to offer a rich and extensive climate history preserved in the layers of seafloor sediment, understanding the source and subsequent progression of this sediment is necessary for interpretation of past climate from this record.

Beneath the ice shelf, seismic studies have established that a channel between Ross Island and Black and White Islands exists (Horgan et al., in press), formed under flexural deformation during uplift of the archipelago. This channel acts as a trap for sediment deposition and strongly influences the circulation in this cavity.

Ocean flow beneath the ice shelf is influenced by patterns in associated ocean areas, although the ice shelf itself is also likely to significantly influence the sub-ice ocean circulation. The circulation in the open water areas immediately adjacent are fairly well understood, a result of the combination of many short-term data sets from McMurdo Sound and the Ross Sea (see fig. 2.1).

### 2.1 Circulation of McMurdo Sound

The general flow pattern for McMurdo Sound from historical observations has advection of relatively warm water from the north along the eastern side of the sound. Most flow continues to the south, beneath the McMurdo Ice Shelf, with the remainder turning westward across the front of the McMurdo Ice Shelf before mixing with water from beneath the ice shelf to flow northward along the western side of the sound.

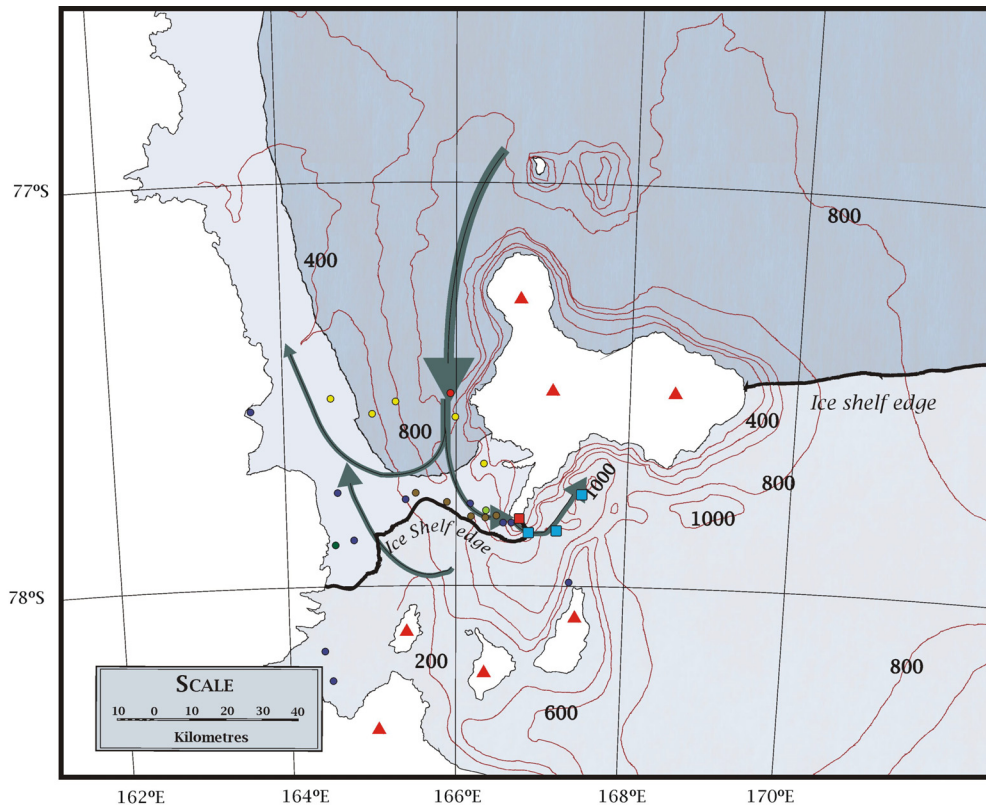


Figure 2.1: Map of McMurdo Sound region with locations of current meter stations mentioned in the text. Historical sites are shown with coloured circles, Gilmour (1963) in yellow, Gilmour (1975) brown, Lewis and Perkin (1985) red, Mitchell and Bye (1985) dark green, Barry and Dayton (1988) dark blue, Barry et al. (1990) pale green. Study sites from January 2003 are shown with blue squares. Also shown are the current flow directions inferred from current meter data at these sites. Bathymetry is shown in meters below sea level, with 200 m contours. For names of main topographic features, see figure 1.1.

This circulation pattern has been deduced from current meter data in conjunction with profiles of temperature and salinity. Most data collection was carried out during the summer, frequently for only a few days at a time. These short-term (1 - 5 days) data sets are able to capture some changes due to diurnal tidal oscillation, but miss longer term variations, e.g., a complete phase shift between the two main components occurs every 13.7 days (Goring and Pyne, 2003). The tidal response is usually the most significant signal observed in time-series current meter data. With data series that are unable to capture a significant portion of the longer-term tidal cycle, knowledge of the complete forcing involved is highly restricted.

The summer bias in observations means that the circulation at other times of the year is less well-known, and observations from these times show some differences (Lewis and Perkin, 1985). These might arise because the driver for thermohaline circulation is the cycle of salt rejection as a result of winter formation and late-summer break-up of sea-ice. Changes on an interannual scale are also likely, as the local regime responds to large scale atmospheric and oceanic forcing (Barry and Dayton, 1988).

### 2.1.1 Eastern McMurdo Sound

The flow in eastern McMurdo Sound consists mainly of a net southward advection of relatively warm water from the Ross Sea. Observations from moored current meters in McMurdo Sound show that flow in the top  $\sim 200$  m of the water column is strongly affected by the diurnal tidal oscillation. This is in contrast to the lower part, where the flow is almost consistently southwards (Barry and Dayton, 1988; Heath, 1977; Barry et al., 1990). This consistent southward flow of warm water at depth results in water column productivity rates being much higher in eastern McMurdo Sound than in the west (Barry and Dayton, 1988). The observed rates are such that these communities must rely on the advection of nutrients from regions far enough north of the sound so as to not be ice-covered or in perpetual darkness during winter (Barry and Dayton, 1988).

Leventer and Dunbar (1988) used the relative proportions of two diatom types in seafloor sediments as an indicator of primary productivity in the water column. They reported proportions of diatoms in the eastern sound indicative of advection from regions of primary production in the open water. In addition, patterns of relative abundances of the two diatom types in cores from the seafloor were observed to be similar throughout the sound. This indicates that, although climate may have changed a little, the general pattern of marine circulation has not changed significantly over the past  $\sim 200$  years.

Mitchell and Bye (1985) observed the water in the eastern sound to have a temperature significantly above its *in-situ* freezing point at all depths. The presence of this relatively warmer water is also supported by the high sea ice melt rate observed by Leventer et al. (1987) and Mitchell and Bye (1985).

A different pattern emerges from October observations. Lewis and Perkin (1985) reported results from moored current meters showing a net northward flow near the edge of the ice shelf, in the opposite direction to the summer observations. They also observed

water throughout McMurdo Sound which, from its measured temperature and salinity, must have been cooled by contact with the ice shelf at depth. Cooled water was also observed by Barry et al. (1990) who, with current meters moored at slightly different depths and for a longer period, concluded that the water tongue was a short-lived cross-current and not indicative of net flow.

There remains some uncertainty as to the direction of flow immediately off Pram Point. Heath (1971, 1977) reported that closer than 2km from the coast flow was out from beneath the McMurdo Ice Shelf, attributing this to the water being sourced east of Ross Island and having travelled beneath the Ross Ice Shelf. Pram Point is the location of highest temperatures and salinities in his study, and he found it curious that water could retain these characteristics after such a long journey beneath the ice shelf. These observations were made over several days, but continuous measurements were only up to seven hours long. It is quite possible that as these measurements captured less than half of the tidal flow oscillation, the net flows could have been in the opposite direction. This would mean that the observed characteristics were of water sourced from the local Hut Point area. Water from here would be more likely to retain its open-water characteristics than it would after a journey beneath the ice shelf.

### 2.1.2 Western McMurdo Sound

The coldest waters are found in the southwestern sound (Barry and Dayton, 1988), a result of water from the eastern and central areas mixing with northward flowing sub-ice shelf waters. Barry and Dayton (1988) reported a mean speed slightly lower than in the eastern sound, and nearly continuous northwards flow. This is also consistent with the observation of platelet ice deposition in the Dailey Islands area, within 5km of the ice shelf edge (Pyne pers. comm).

For western McMurdo Sound, temperatures at all depths are close to the 10m *in-situ* freezing temperature (Mitchell and Bye, 1985), contributing to the very low sea ice melt rates observed (Leventer et al., 1987). These low melt rates result in multi-year sea ice in the vicinity of the Dailey Islands and Koetlitz Glacier (see fig. 1.1), observed by Mitchell and Bye (1985) through the unusually low salinity of the sea ice there. They also suggest that any meltwater observed in this area is probably the result of fresh water surface intrusions from the Hobbs Glacier. Fresh water might also have been sourced from the Blue Glacier or from surface melt of the adjacent ice shelf.

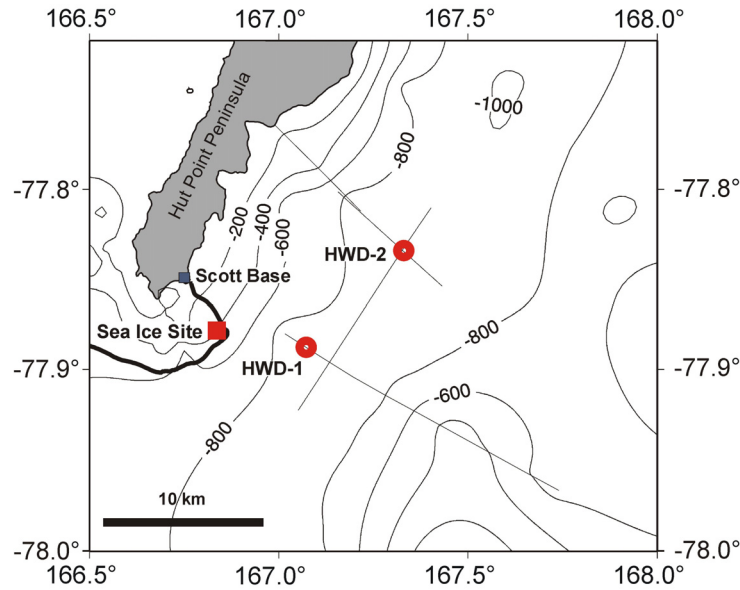


Figure 2.2: Bathymetry map of Windless Bight area showing location of the HWD sites, ‘HWD-1’ and ‘HWD-2’ on the McMurdo Ice Shelf, the Sea Ice Site, and their proximity to Scott Base.

The observed pattern of sea ice break-up is different to that for the eastern sound: in the west, the pack is blown out of the sound still largely intact, with little evidence of *in-situ* melting. The oligotrophic water sourced from beneath the Ross Ice Shelf affects the diatom assemblages in seafloor sediments, which are found to be similar to those of the deep sea. Unlike the eastern sound, they show very little evidence of advection from open, lighted areas (Leventer and Dunbar, 1988).

## 2.2 Data collection - Windless Bight, 2003

Profiles of currents and water characteristics have recently been collected from the sub-ice shelf cavity at Windless Bight on the McMurdo Ice Shelf. During January 2003, a hot water drill (HWD) was used at two sites, HWD-1 and HWD-2, approximately 6 and 12 km from Scott Base (see fig. 2.2), to gain access through the McMurdo Ice Shelf to the underlying ocean and seafloor. At each site, the water column was profiled for velocity using an Inter-Ocean S4 current meter, and for temperature and salinity using a Seabird Conductivity-Temperature-Depth (CTD) profiler, with several casts over the period of one diurnal tidal cycle.

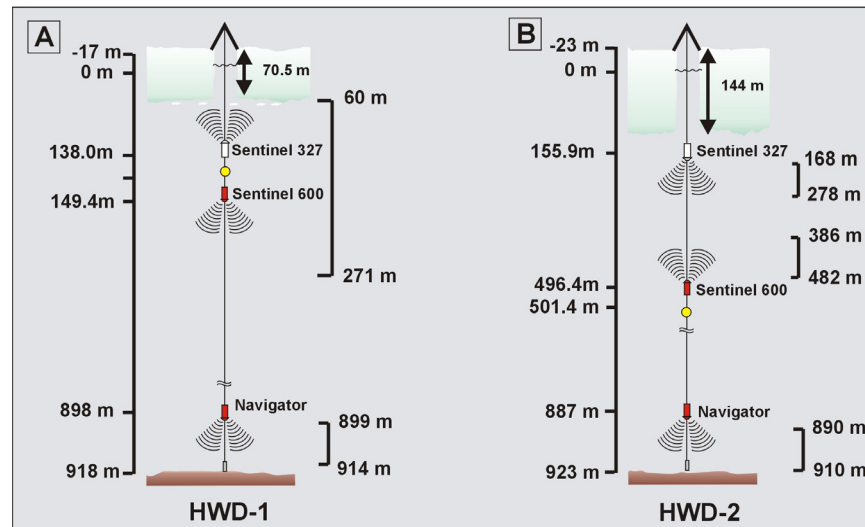


Figure 2.3: Diagram showing the array of instruments at the two HWD sites on the McMurdo Ice Shelf. Depth ranges of the three instruments are also shown in metres below sea level (m BSL).

Longer-term current measurements were taken with three Acoustic Doppler Current Profilers (ADCPs) moored for a few diurnal tidal cycles, approximately covering the peak of spring tide - periods of maximum tidal amplitude. These instruments were able to survey a range of depths simultaneously, and the array was constructed to observe the water column down to 300 m immediately below the ice shelf and also the benthic layer at the seafloor (see fig. 2.3). The Inter-Ocean S4 was included in the moorings for comparison between the different types of instrument (see also Appendix B).

In addition to the two HWD sites, a larger Broadband ADCP was moored from the sea ice at the northern edge of the McMurdo Ice Shelf for a period of 23 days (see fig. 2.2). The 23-day mooring covered close to two spring/neap tidal cycles, capturing this longer-term variation which, for logistical reasons, could not be obtained beneath the ice shelf proper. A check on this instrument soon after initial deployment at 5 m BSL (metres below sea level) revealed that the instrument had become swamped by platelet ice after 9.5 hours, which prevented further data collection. The instrument was redeployed at a depth of 10 m BSL, and produced a continuous record for a further 23 days for all depths between 12 and  $\sim$ 300 m BSL.

The local ice conditions at the time of the site occupation at Windless Bight were un-

usual, in that the sea ice in Southern McMurdo Sound did not break out that year, nor had it broken out the previous summer. The most likely reason for this behaviour was the presence of the large iceberg, B15A (see fig. 1.2), which had calved from the edge of the Ross Ice Shelf and grounded to the north of Ross Island.

The sub-ice shelf currents observed at Windless Bight were probably affected by the presence of mature sea ice which had survived through the summer, but more fundamentally by the presence of the iceberg itself. This is likely to have had a significant effect on the normal circulation patterns around Ross Island, as its draft was sufficient to block the normal flow to a depth of  $\sim 300$  m (Blankenship et al., 2002).

# Chapter 3

## Current profile measurements

Current meter data were collected from beneath the McMurdo Ice Shelf at two sites using an array of three Acoustic Doppler Current Profilers (ADCPs) moored for 2 - 3 days. In addition, a third site at the northern edge of the ice shelf was occupied, at which a single ADCP was moored from the sea ice for 23 days. This provided a data set which was simultaneous with both ice shelf sites. Tidal height data collected at Scott Base were available for indirect comparison between all three sites.

ADCPs are able to survey a range of depths simultaneously. Each instrument sends a pulse of sound energy at regular intervals, and the return signal is collected by four transducers and subdivided temporally, corresponding to different depth bins. The strength of the return signal depends on the concentration of particulate suspended in the water column, but for all moorings this was high enough to produce good data.

Maximum speeds at all sites were found to be around  $90^\circ$  out of phase with the tidal height measured at Scott Base. This phase shift is typically a feature of shallow water where flow is frictionally dominated. That it applies in this case demonstrates that the flow here, constrained beneath ice, is likewise frictionally dominated.

### 3.1 Sea ice site

The sea ice site ( $77^\circ 52.773'$  S,  $166^\circ 50.042'$  E) was occupied with one ADCP for the period 06:28 11 January to 03:48 03 February 2003 (UTC), almost long enough to cover two 13-day tidal phase shifts, and clearly including one neap and two spring tidal periods. An RDI 'Broadband' long-range (154 kHz) ADCP was deployed at this site. It was set up to output data for each 8 m bin between 10 metres below sea level (m BSL) and 490 m

BSL in 10 minute ensembles. Each ensemble output was the average in 3-dimensions of forty-eight measurements collected every 2 seconds at the start of every 10 minute period.

A check on this instrument soon after initial deployment at 5 m BSL (metres below sea level) revealed that the instrument had become swamped by platelet ice after 9.5 hours, which prevented further data collection. The instrument was redeployed at a depth of 10 m BSL, and produced a continuous record for a further 23 days for all depths to  $\sim 300$  m BSL, without apparent platelet ice effect.

The actual depth range was less than anticipated, so that accurate results were obtained only within the range 16 to 320 m BSL. This was approximately half of the water depth at this site. The instrument was not corrected for magnetic declination prior to deployment so the required adjustment of  $145^\circ$ , measured and calculated at the site, was made to the raw data prior to analysis.

Immediately apparent in the data (see figures 3.1 and 3.2) is the consistency in both direction and magnitude of the flow throughout the water column. At spring tide a high degree of diurnal variation can be seen in both eastwards ( $V_e$ ) and northwards ( $V_n$ ) components of velocity, while more consistent SE flow is observed during the neap tide. When averaged over complete diurnal tidal cycles the net throughflow was to the south-east, varying between  $116^\circ$  and  $140^\circ$ , with a mean magnitude of  $0.18 \text{ m s}^{-1}$ .

Behaviour of the water column differed markedly between spring and neap tides. At spring tide the tidal current ellipse was narrow and the degree of variability high, resulting in oscillatory flow within a narrow range of direction. The dominant direction lay parallel to the channel around Ross Island. Spring tide mean current speeds were about average compared to the whole mooring, whereas the net throughflow was very low - only  $0.09 \text{ m s}^{-1}$  compared to  $0.14 \text{ m s}^{-1}$  for the whole mooring. The low throughflow with normal speeds indicates that flow is back and forth along the main axis of oscillation.

Correlation between  $V_e$  in the top and middle sections of the water column (bins at  $\simeq 50$  m BSL, and  $\simeq 280$  m BSL) was highest during the spring tide, obtaining a maximum value of 0.67 during the first spring tide, January 14 - 20, compared to an average of 0.46 for the whole mooring. This indicates that the top and middle sections respond similarly to the spring tide.

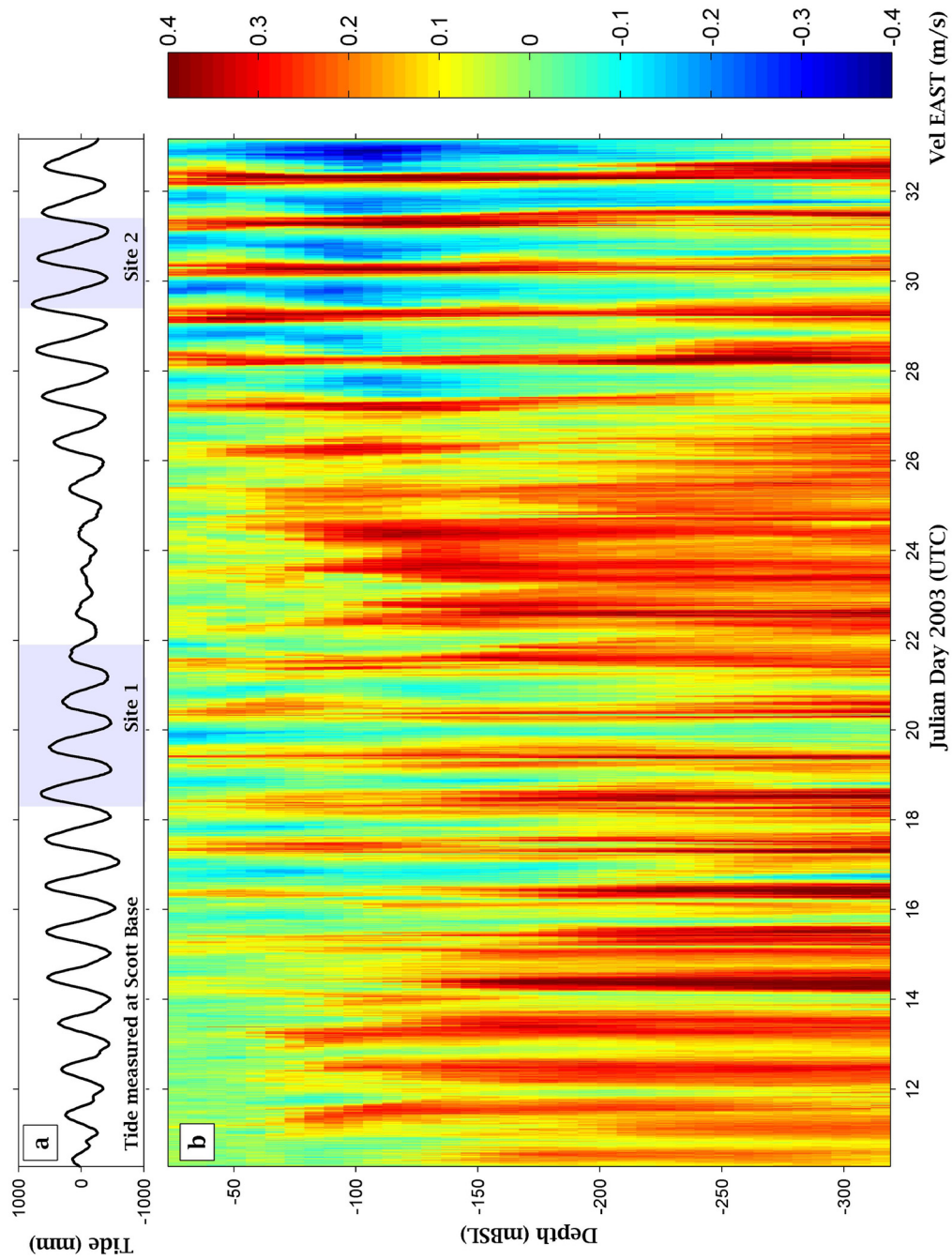


Figure 3.1: Eastwards component of velocity,  $V_e$ , measured at the Sea Ice Site. Time-series (a) shows the tidal height variation at Scott Base, 6km from the site. Time-series (b) is the output from the Broadband Acoustic Doppler Current Profiler (ADCP).

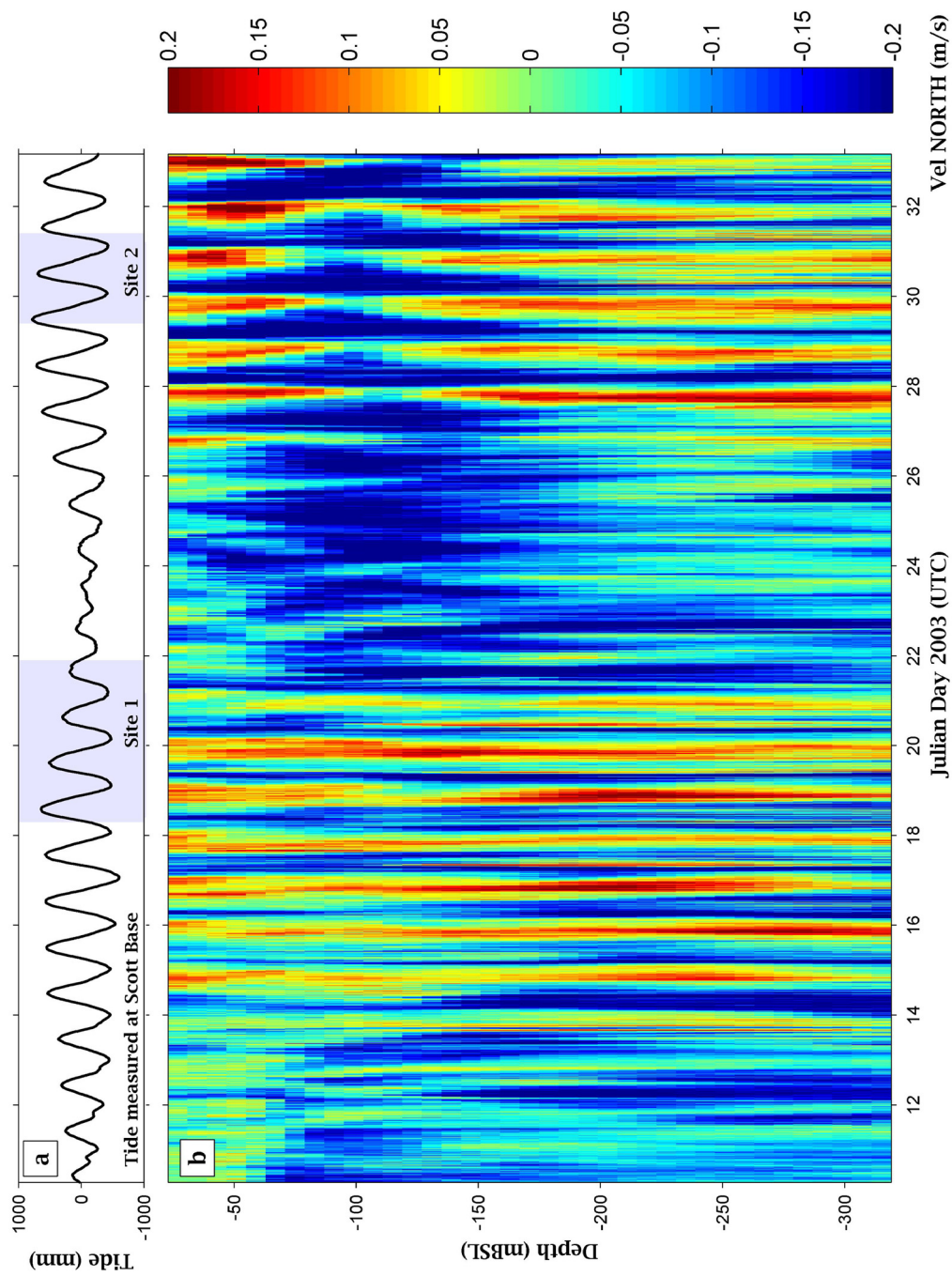


Figure 3.2: Northwards component of velocity,  $V_n$ , measured at the Sea Ice Site. Time-series (a) shows the tidal height variation at Scott Base, 6km from the site. Time-series (b) is the output from the Broadband Acoustic Doppler Current Profiler (ADCP).

During the neap tide, correlation between the top and middle sections of the water column dropped to 0.05,  $\sim 10\%$  of average. The reason for this is their differing responses to the tidal cycle (see figures 3.1 and 3.2). In the top 50 m similar variation in flow direction was observed over the neap tide (days 22 to 27) as observed for the spring tide. Below 50m, particularly for  $V_e$ , the variation reduced over the neap tide resulting in a fairly consistent flow towards the south-east. Hence, the top and middle sections of the water column were observed to behave similarly over the spring tide (high correlation), but quite differently over the neap tide (low correlation).

In spite of this, the net throughflow was highest during neap tide, with a value of  $0.20 \text{ m s}^{-1}$  at  $123^\circ$ . This was due to the mean current speed ( $0.21 \text{ m s}^{-1}$ ) being higher than for the spring tide ( $0.18 \text{ m s}^{-1}$ ), and the consistent direction of flow to the southeast during this period.

## 3.2 Ice shelf site #1 - HWD-1

Three ADCPs were deployed at HWD-1 (Hot Water Drill #1) ( $77^\circ 53.308' \text{ S}$ ,  $167^\circ 05.067' \text{ E}$ ) in an array which surveyed about one third of the water column (see fig. 2.3). The array was deployed and collecting data from 07:50 18 January to 22:10 21 January 2003 (UTC), capturing the peak flow of the spring tide. The total of 86.5 hours was longer than planned, due to a storm event which delayed the recovery of the instruments.

A Sentinel 327 (Sn327), operating at 307.2 kHz at a depth of 138 m BSL, looked up to survey the boundary layer at the base of the ice shelf. A Sentinel 600 (Sn600), also operating at 307.2 kHz, looked down from a depth of 149 m BSL. Twenty metres above the seafloor a Navigator, operating at 614.4 kHz, looked down from 898 m BSL with the aim of capturing the flow structure in the benthic boundary layer, although this was not achieved (See fig. 2.3). With the two Sentinels moored only 10 m apart, they gave an almost continuous record from 60 m BSL to 271 m BSL.

Both Sentinels were programmed to calculate the mean of 200 readings 3 seconds apart to give a measurement every 10 min. A bin size of 4 m was used for the Sn327, but this was increased to 10 m for the Sn600 to achieve greater range. The Navigator was set to record the mean of 175 readings 0.62 s apart at the start of every 5 min period, with a

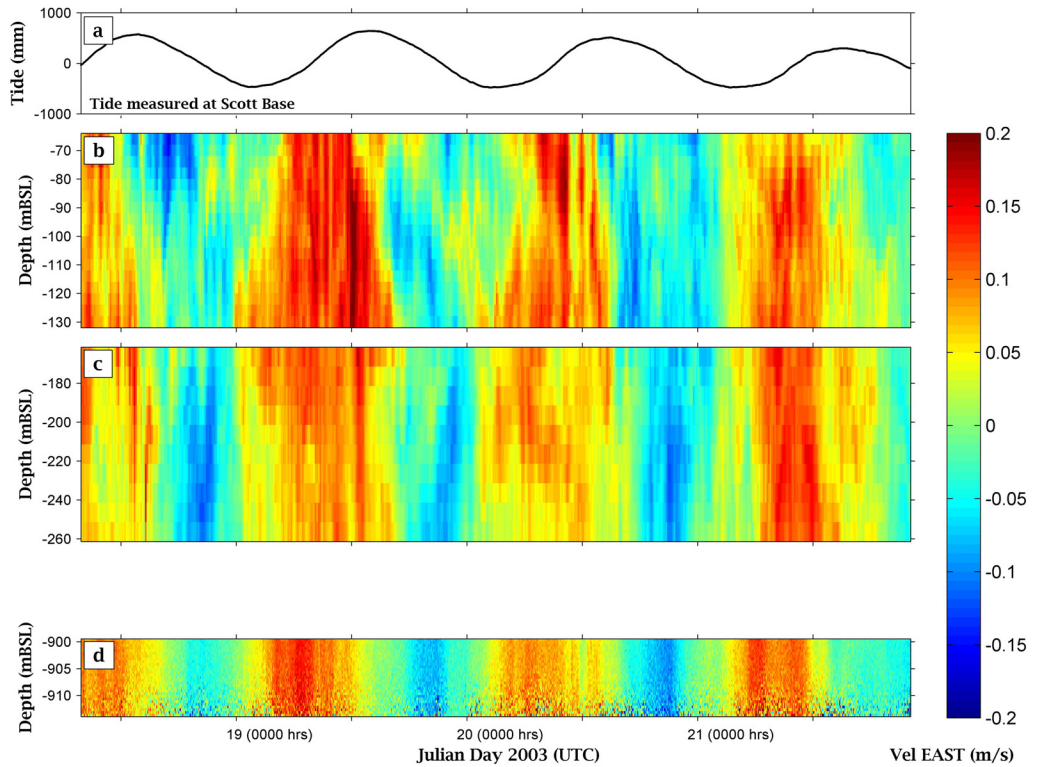


Figure 3.3: Eastwards component of velocity,  $V_e$  measured at HWD-1. Time-series (a) shows the tidal height variation at Scott Base, 6km from the site. Time-series (b), (c) and (d) are the output from the three Acoustic Doppler Current Profilers (ADCPs), Sentinel 327, Sentinel 600, Navigator respectively.

bin size of 0.5 m.

All three instruments were corrected for magnetic declination of  $155^\circ$  prior to deployment, although this was subsequently found to be  $10^\circ$  too great. Rotation of the data to account for this was found to be insignificant, so the additional correction was not used.

Tidal structure could be clearly seen in both  $V_e$  and  $V_n$  components of flow (see figures 3.3 and 3.4), with coherence of the signal through the water column also apparent. Tidal structure was far more prevalent in  $V_e$  than  $V_n$ , indicating oscillating flow along the primary axis of the channel between Ross Island and Black and White Islands. The strongest flows were eastwards on the flood tide with slightly weaker flow westwards on the ebb tide.

A  $90^\circ$  phase difference between the tidal height measured at Scott Base and the speed

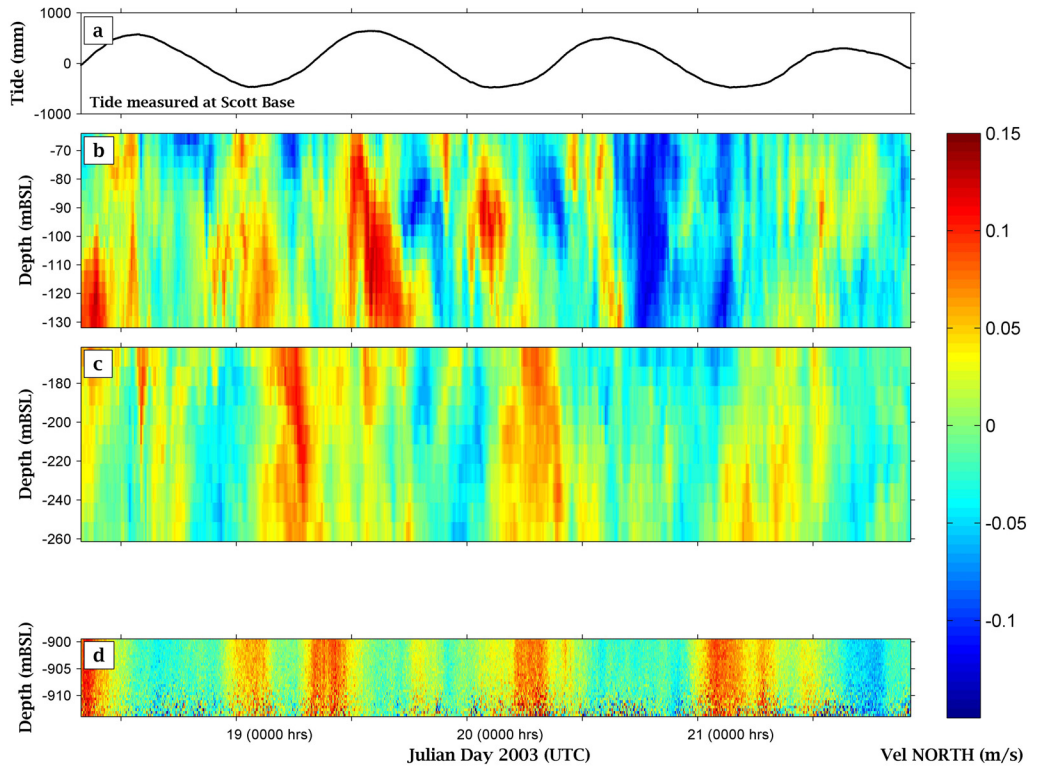


Figure 3.4: Northwards component of velocity,  $V_n$ , measured at HWD-1. Time-series (a) shows the tidal height variation measured synchronously at Scott Base, 6km from the site. Time-series (b), (c) and (d) are the time-series output from the three Acoustic Doppler Current Profilers (ADCPs), Sentinel 327, Sentinel 600, Navigator respectively.

of the upper water column, as measured by the Sn327, was observed in both  $V_e$  and  $V_n$ . Figure 3.5 shows that the maximum correlation of 0.89 between  $V_e$  and tidal height was found with a phase shift of 6 hours (i.e. on the flood tide). The flood tide also coincided with the maximum correlation between  $V_n$  and tidal height (see fig. 3.6), although this was only 0.32. Similarly, the maximum correlation between the tidal height and the Sn600 record was for a phase shift of 6 hours; the two correlations were 0.87 and 0.74 for  $V_e$  and  $V_n$ , respectively.

The behaviour of the lower water column with respect to tidal height was similar, although a slightly longer phase shift of 7 hours was needed to produce the maximum correlation of 0.9 with  $V_e$ , and a phase shift of 9 hours gave maximum correlation of 0.7 with  $V_n$ . Compared to the upper water column, the difference in tidal phase lag represented a shift in maximum correlation away from the flood tide. In addition, the direction of oscillation was closer to north than for the upper water column, perhaps indicating the

different topographic steering of the ice shelf and seafloor.

The tidal signal was dominant in the  $V_e$  component, so that speeds were roughly equivalent for eastwards and westwards flow, and much higher than for either northwards or southwards flow. Flow in the  $V_n$  component, particularly below  $\sim 100$  m, favoured north over south, giving a net flow towards the northeast on the flood tide and towards the west on the ebb, approximately following the contour of the coast of Ross Island at this site. The flow in  $V_n$  observed by the Sn327 immediately beneath the ice shelf was significantly different to the flow observed by the Sn600 below, so it is likely that the structure in  $V_n$  was due to a combination of sea floor topography, and interaction with the ice shelf.

Both the Sn600 and Navigator recorded maximum flows of  $0.18 \text{ m s}^{-1}$ . A significantly higher maximum speed of  $0.22 \text{ m s}^{-1}$  was recorded by the Sn327 in the boundary layer beneath the ice shelf. This indicated an influence from the ice shelf on the speed of the horizontal flow. While a similar effect was expected along the sea floor, the Navigator was

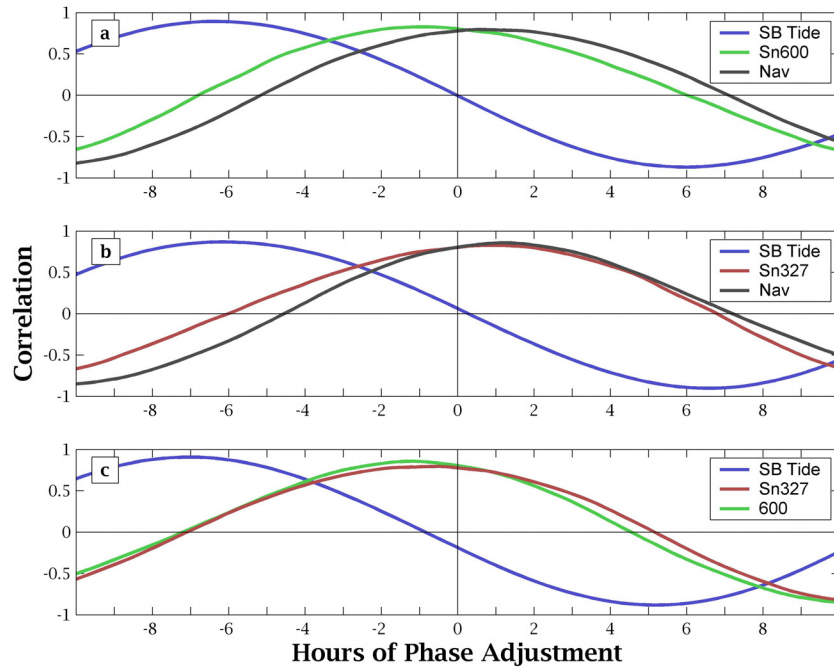


Figure 3.5: Phase-shifted correlation between  $V_e$  from three ADCPs at HWD-1 and the tidal height measured at Scott Base, to determine optimal phase shift. (a) is the correlation between Sn327 and the other data, (b) the correlation between Sn600 and others, and (c) the correlation between Navigator and others.

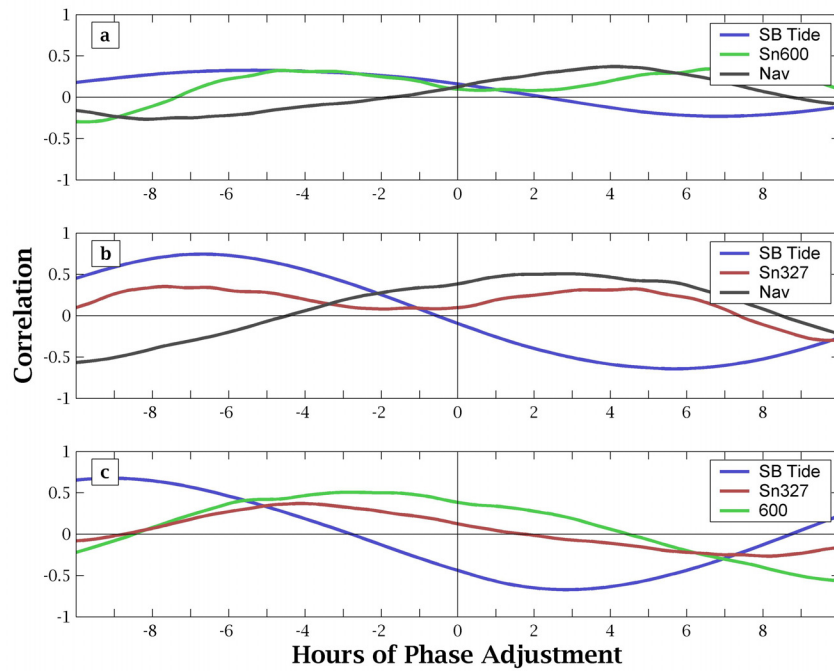


Figure 3.6: Phase-shifted correlation between  $V_n$  from three ADCPs at HWD-1 and the tidal height measured at Scott Base, to determine optimal shift. (a) is the correlation between Sn327 and the other data, (b) the correlation between Sn600 and others, and (c) the correlation between Navigator and others.

moored higher than anticipated, so that boundary flows were not observed at the seafloor for site HWD-1.

Net flow was to the east, although the direction varied down the water column. Averaged over the first three diurnal tidal periods (74 hours), throughflow was  $0.03 \text{ m s}^{-1}$  for each instrument, at  $104^\circ$  for the Sn327, at  $73^\circ$  for the Sn600, and at  $65^\circ$  for the Navigator. This indicates a similar flow throughout the water column, but with some shearing that amounts to  $\sim 40^\circ$ .

This was also evident in the correlation between the three sets of observations when separated into the two velocity components. Compared to the Sn327  $V_e$  record, a shift of -1 hr in the Sn600  $V_e$  achieved maximum correlation of 0.8, whereas as a shift of +0.5 hr in the Navigator  $V_e$  was required to produce the same maximum correlation.

The pattern of correlation was not as clear in the  $V_n$  records of the three instruments.

The maximum correlation between  $V_n$  records was only 0.3, achieved with a +4 hour shift for both the Sn600 and Navigator compared to the Sn327. Compared to  $V_e$ , such low correlation is not significant, and again indicates the high degree of tidal oscillation along the east-west direction, also demonstrating the consistency in the  $V_e$  signal throughout the water column.

For no phase shift, i.e. measurements as recorded, there was little if any correlation between  $V_n$  from the Sn327 and from the Sn600. This was in contrast to the high correlation between the two ADCPs in  $V_e$ , indicating that there was a distinct difference in flow direction between the two instruments, or separate layers, rather than a steady turning in flow direction down the water column.

Time-series' of depth-averaged velocities were compared to the record from the same period at the sea ice site. This was done to determine the lag between the two sites, on the assumption that the tidal height signal took time to propagate to the sites beneath the ice shelf. Far greater correlation ( $\sim 0.8$ ) was found for the depth-averaged  $V_e$  than for  $V_n$ , consistent with flow along the channel as it follows the coast of Ross Island.

The  $V_e$  records of the Sn327 and Navigator appear to lag the ADCP at the sea ice site by about 1 - 1.5 hours, although the Sn600  $V_e$  record appears synchronous with the sea ice record.

### **3.3 Ice shelf site #2 - HWD-2**

The three ADCPs used at HWD-1 were redeployed in a similar array at this site (77°50.111' S, 167°20.209' E). The instruments were moored and collecting data for the period 10:15 30 January to 09:25 01 February 2003 (UTC), again covering the peak of the spring tide. This total of 47.25 hours was close to the planned time of  $\sim 48$  hours - chosen to ensure recovery of the instruments before the hole through the ice shelf refroze.

The increased draft of the ice shelf restricted the deployment of the Sn327, as the pressure rating of its casing was only to 200 m. Therefore the Sn327 was deployed to look down from the base of the ice shelf at 155.9 m BSL. The Sn600 looked up from 496.4 m BSL, and the Navigator looked down from 887 m BSL,  $\sim 30$  m above the sea floor (see fig. 2.3). Again, this position was not deep enough to see the seafloor. With this deployment, an

equivalent proportion of the water column was surveyed at both HWD sites. At HWD-2, the depth ranges of the Sn327 and the Sn600 were not sufficiently close to provide a single, effectively continuous record as before.

Both Sentinels were programmed to collect 150 readings 2 s apart with a mean calculated for every five minute period. A bin size of 10 m was used for the Sn327 and 12 m for the Sn600 in order to gain maximum range. The Navigator was set to record the mean of 130 readings 0.62 s apart at the start of each five minute period with a bin size of 2 m.

All three instruments were corrected for magnetic declination of  $155^\circ$  prior to deployment. As at HWD-1 this correction was subsequently found to be  $10^\circ$  too great, but as with HWD-1 all analysis has been completed with the original correction of  $155^\circ$  applied.

Tidal structure was immediately apparent in  $V_e$  (see fig. 3.7) with a striking consistency of response through the water column. For  $V_n$  the tidal structure was not as apparent, particularly for the Sn327, and the consistency down the water column was also lacking (see fig. 3.8). In both  $V_e$  and  $V_n$  records the flood tide produced maximum velocity, whereas at ebb tide velocity was reduced to near-zero, so that flow tended to the north-east on the flood tide and zero on the ebb. For this site the dominant northeast flow direction again lay parallel to the coast of Ross Island.

The maximum correlation between tidal height and  $V_e$  occurred for a  $\sim 7.25$  hour phase shift (see fig. 3.9), again on the flood tide, which was approximately 1.25 hours ahead of correlations at HWD-1. Conversely, in relation to the tidal height, the  $V_n$  lag (see fig. 3.10) was approximately 2.75 hours behind HWD-1. This difference in behaviour was likely to be due to the much weaker  $V_n$  signal at both sites, as well as the difference in net flow direction.

At this site the response of the bottom part of the water column to the tidal signal appeared similar to mid-water. For  $V_e$  in both the Sn600 and Navigator records the tidal height was  $\sim 7.25$  hours behind, with maximum correlation of 0.91 and 0.90 respectively. The same phase difference, 7.25 hours, produced a slightly higher maximum correlation to the Sn327 of 0.92. The tidal height lags both the Sn600 and Navigator  $V_n$  records by  $\sim 6.25$  hours with maximum correlation of 0.68 and 0.61 respectively - significantly higher than the maximum correlation with the Sn327  $V_n$ , which was 0.51, with only a 3 hour

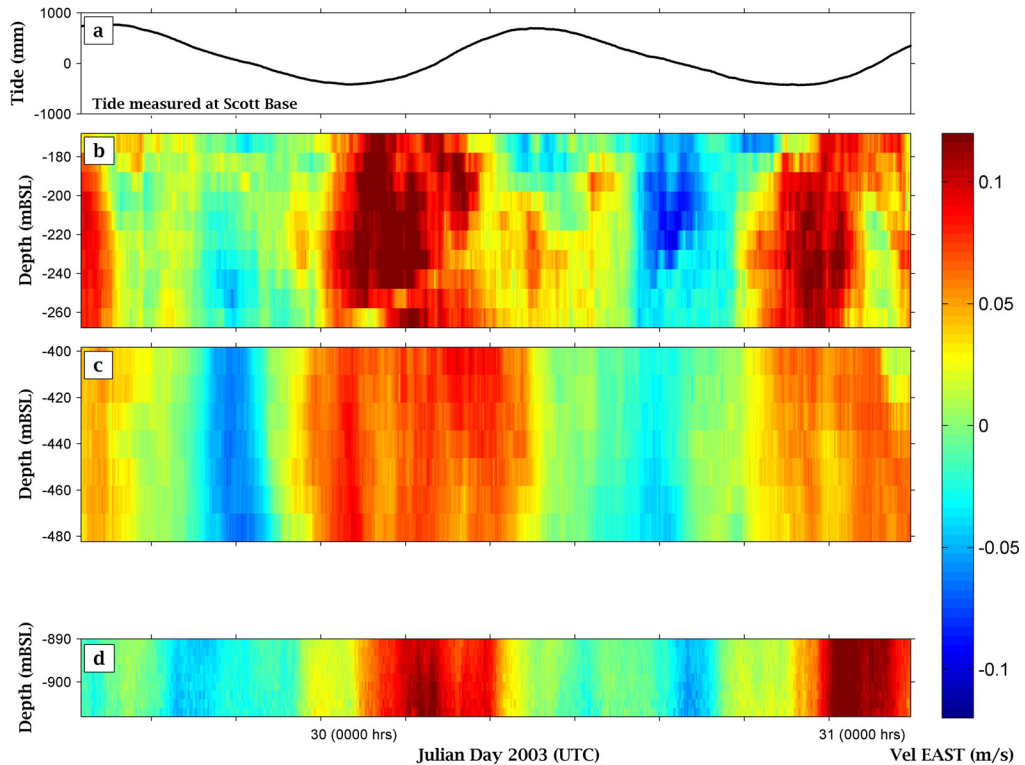


Figure 3.7: Eastwards component of velocity,  $V_e$ , measured at HWD-2. Time-series (a) shows the tidal height variation at Scott Base,  $\sim 12$ km from the site. Time-series (b), (c) and (d) are the time-series output from the three Acoustic Doppler Current Profilers (ADCPs), Sentinel 327, Sentinel 600, Navigator respectively.

phase shift.

At HWD-2, unlike HWD-1, the eastward and westward flows were not of comparable magnitude. While maximum eastward and westward flows were roughly equivalent, the length of time for which these flows were sustained were not equivalent. On the flood tide, flow was towards the east, and was sustained for approximately half of the diurnal cycle. For the ebb tide,  $V_e$  was either towards the west or close to zero, each for one quarter of the cycle.

For the  $V_n$  component, flow was sustained to the north for almost the whole mooring, with flow to the south almost zero: the maximum flow to the south was  $0.06 \text{ m s}^{-1}$ , recorded by the Sn327, compared with  $0.17 \text{ m s}^{-1}$  to the north.

The  $V_e$  and  $V_n$  components of velocity were roughly equivalent, with flow tending closer

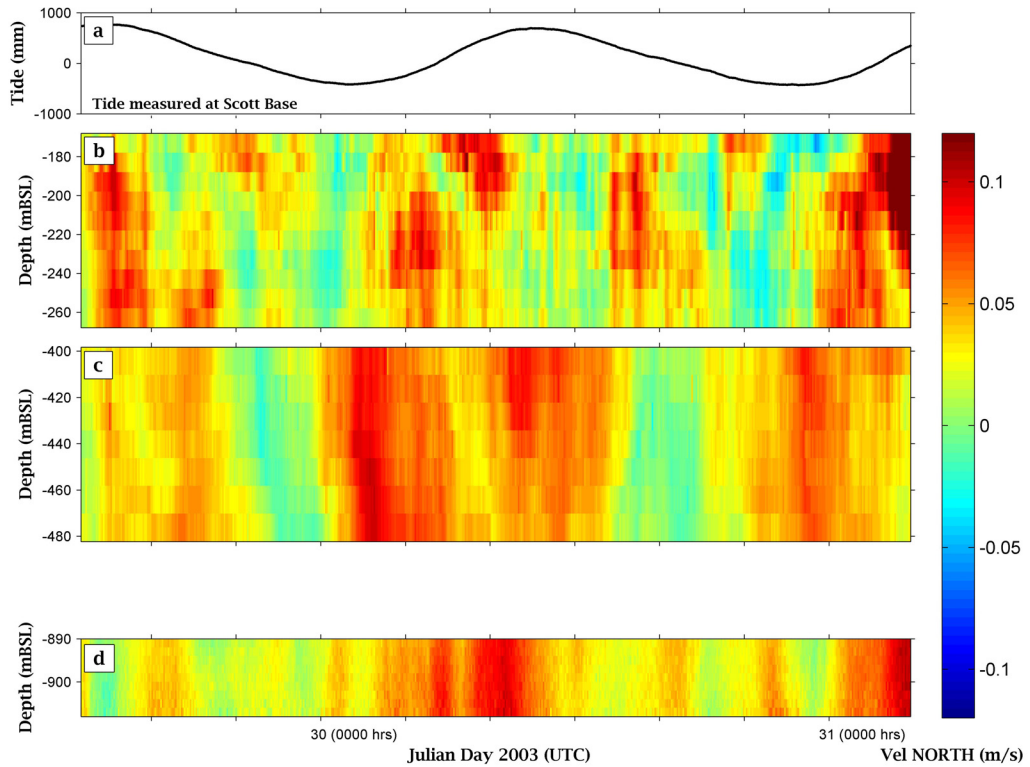


Figure 3.8: Northwards component of velocity,  $V_n$ , measured at HWD-2. Time-series (a) shows the tidal height variation at Scott Base,  $\sim 12$ km from the site. Time-series (b), (c) and (d) are the time-series output from the three Acoustic Doppler Current Profilers (ADCPs), Sentinel 327, Sentinel 600, Navigator respectively.

to north deeper in the water column. Net throughflow over the first complete tidal cycle was  $0.05 \text{ m s}^{-1}$  at  $52^\circ$  for the Sn327,  $0.05 \text{ m s}^{-1}$  at  $39^\circ$  for the Sn600, and  $0.04 \text{ m s}^{-1}$  at  $30^\circ$  for the Navigator.

Although the net throughflow was significantly lower at the base of the water column compared to mid-depth, the peak flows recorded by the Navigator were higher than those recorded by the Sn600 ( $0.15 \text{ m s}^{-1}$  compared to  $0.13 \text{ m s}^{-1}$ ), demonstrating more consistency in mid-water flow.

At site HWD-2, the maximum speed of  $0.21 \text{ m s}^{-1}$  was recorded by the Sn327 near the top of the water column. This was similar to the maximum speed recorded at HWD-1 near the base of the ice shelf, although net throughflow was significantly higher at HWD-2.

Correlation between the instruments down the water column followed a similar pattern

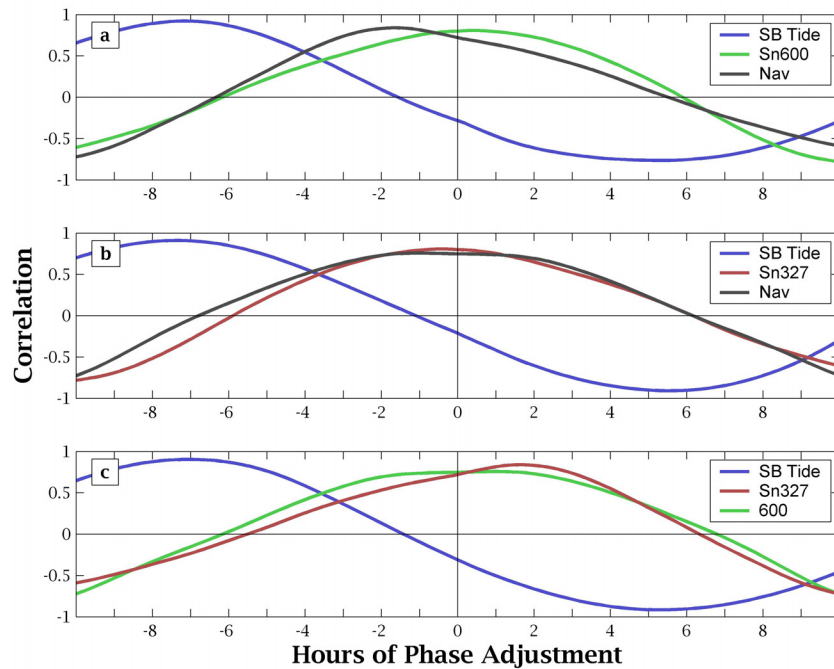


Figure 3.9: Phase-shifted correlation between  $V_e$  from three ADCPs at HWD-2 and the tidal height measured at Scott Base, to determine optimal phase shift. (a) is the correlation between Sn327 and the other data, (b) the correlation between Sn600 and others, and (c) the correlation between Navigator and others. Note that for all instruments, maximum correlation with Scott Base tidal height corresponds to  $\sim 6$  hour shift from maximum, or flood tide.

to HWD-1: Much greater correlation in  $V_e$  ( $\sim 0.8$ ), compared to  $V_n$  ( $\sim 0.5$ ), longer phase shifts evident in  $V_n$ . This difference was caused by the less predictable and weaker response of  $V_n$  to the tidal oscillation throughout the water column at both sites. Again, no phase shift produced very low, if any correlation between the Sn327 and the Sn600 in  $V_n$ , but high in  $V_e$ , demonstrating a real difference in instantaneous flow direction between the two instruments.

Synchronous measurements of velocity from the sea ice site were compared to those from HWD-2, with results similar to the equivalent analysis at HWD-1.  $V_e$  from the sea ice site record lagged HWD-2 by 0.5 - 1.5 hours, with a maximum correlation of 0.94 observed in the Navigator for the shortest phase shift of about half an hour.

For  $V_n$ , the correlation with the sea ice site was primarily negative, consistent with fol-

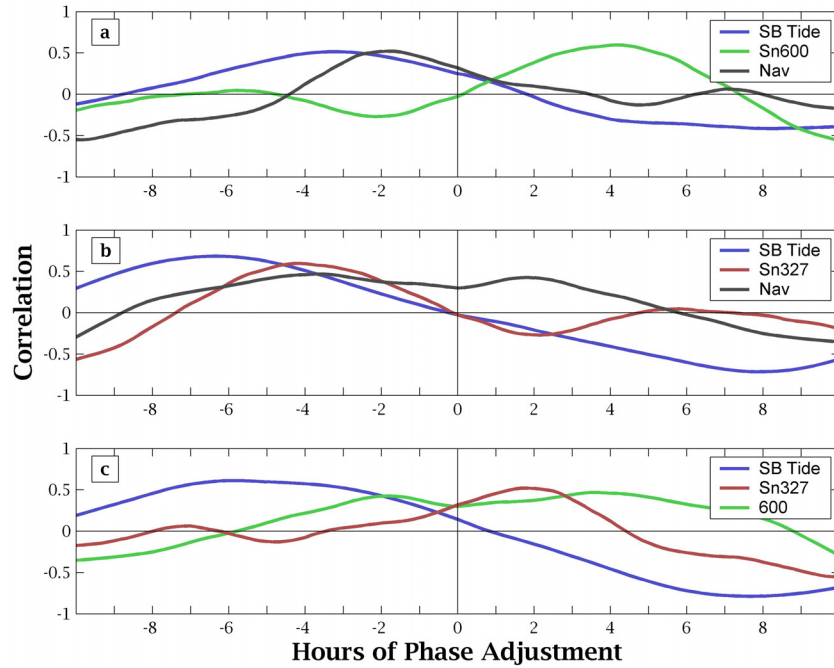


Figure 3.10: Phase-shifted correlation between  $V_n$  from three ADCPs at HWD-2 and the tidal height measured at Scott Base, to determine optimal phase shift. (a) is the correlation between Sn327 and the other data, (b) the correlation between Sn600 and others, and (c) the correlation between Navigator and others.

lowing the coast of Ross Island from McMurdo Sound towards the east. With this general flow pattern, the flow in  $V_n$  could be expected to be southwards at the sea ice site, and northwards at HWD-2, or vice versa. This was particularly clear in the mid-depth record from the Sn600, with a maximum negative correlation of -0.69 for a phase shift about zero.

### 3.4 General circulation at Windless Bight

The moorings at the two ice shelf sites were deployed only over the peak of the spring tides, so that the net circulation can only be described for these periods, and not for other tidal periods. Together, the data revealed a consistent pattern of net throughflow following the channel around Ross Island, and the high correlation through the water column suggests that this pattern was coherent at all depths.

With the change in net throughflow from southeast at the sea ice edge to east then

northeast at the two ice shelf sites, the tidal signal in  $V_n$  was progressively lost, transformed from an oscillating signal as strong as in  $V_e$  at the sea ice site, through to a low but fairly constant flow at HWD-2.

The presence of the ice shelf defining the top of the water column also appears to have had a much greater effect on  $V_n$  than on  $V_e$  when compared to the middle and bottom sections of the water column. The increased variability in  $V_n$  was possibly likely due to the steeper gradient in ice shelf thickness in the N-S direction compared to E-W.

The lower part of the water column at both ice shelf sites had net flow  $\sim 35^\circ$  closer to the north than the top part. This may have been due to the local change in sea floor depth - at 900 m BSL the channel is  $\sim 300$  m deeper than the surrounding area (Horgan et al., in press) - or it may represent a greater proportion of water sourced from the south in the deeper waters.

The net flow pattern that has been established here is effectively in the opposite direction to that taken by the tidal bulge, which propagates around Antarctica anticlockwise, or from east to west in the Ross Sea (Williams and Robinson, 1980). On this spatial scale it is not surprising that the mid-water tidal signal was nearly synchronous between the sea ice and ice shelf sites, which were only  $\sim 10$  km apart.

The lag in the signal reaching the top and bottom layers was most likely due to the mechanics of the situation - either a frictional drag along the horizontal boundaries or the inertia associated with raising and lowering the ice shelf in response to the changing tidal height. A rising ice shelf allows flow of water into the sub-ice cavity, while a lowering ice shelf forces water out from beneath it.

Using the ADCP data from the sea ice site it was possible to compare the flow at spring and neap tides for one site. The flow during neap tide was more consistently towards the southeast than for spring tides. This combined with greater mean current speeds to produce a much higher net transport.

The correlation between the top and middle sections of the water column was greatly reduced during the neap tide - only 0.05,  $\sim 10\%$  of mean correlation. The reason for this was the different responses to the neap tide when the oscillation in flow direction in

the lower section of the water column was reduced, resulting in a consistent flow to the southeast. In contrast, the top  $\sim 50$  m carried similar variation in flow direction as for the spring tides, so that the behaviour of these two sections was quite different during the neap tide.

The currents below the McMurdo Ice Shelf had not been directly measured prior to these observations, but the flow described here is not inconsistent with the flow previously described for McMurdo Sound and the Ross Sea. The flow under the ice shelf appears to be primarily sourced from southern McMurdo Sound, with the direction determined by the shape of the channel between Ross Island and Black and White Islands.

It was previously known that the flow southward down the eastern side of McMurdo Sound separates, with part turning west then north to exit in the north-west of McMurdo Sound. The remaining part, from these observations, flows to the east and into the cavity under the McMurdo Ice Shelf.

The flows into the central sound are known to be temporally variable and it is possible that during the winter season the net flow around Pram Point may reverse, supplying cooled water from beneath the ice shelf into McMurdo Sound.

# Chapter 4

## Profiles of water characteristics

At each of the Hot Water Drill (HWD) sites on the ice shelf, multiple casts of a Seabird Electronics 37-SM CTD (Conductivity-Temperature-Depth) were made over one tidal cycle via the access hole through which the current meters (ADCPs) were deployed. The casts were made as close together as was logistically possible, so that the cycle of cast and subsequent data collection took between 2.5 and 3 hours. The water profile casts and ADCP current meter data could not be collected synchronously, so that any inference drawn to relate them must be made with reference to the tidal cycle.

The CTD measured conductivity, temperature and pressure with an accuracy of  $0.002^{\circ}\text{C}$ ,  $0.0003 \text{ S m}^{-1}$ , and 0.1% of full scale pressure. These were translated into salinity, potential temperature, density and depth in metres below sea level (m BSL), using the Seabird Seaplot software supplied with the instrument. Measurements were made every 5 seconds on a winch wire travelling nominally at  $0.5 \text{ m s}^{-1}$  on both down and up sections of the casts. For analysis, these profiles were interpolated to 1 m depth spacing.

Analysis of the data revealed that anomalously low salinity had been recorded through the ice shelf and in the first  $\sim 200$  m of the water column, so it was assumed that slushy ice had become trapped near the sensors during descent through the ice shelf hole. For this reason, only the upcasts were used in this analysis.

The location of the base of the ice shelf coincided with a sharp transition in salinity, and it was this transition that was used to demarcate the appropriate section of each upcast to be used in analysis. This was consistently within 5 m of the estimated ice shelf draft from routine logging carried out, during the hot water drilling process (Nixdorf and Dunker in Barrett et al. (2004)).

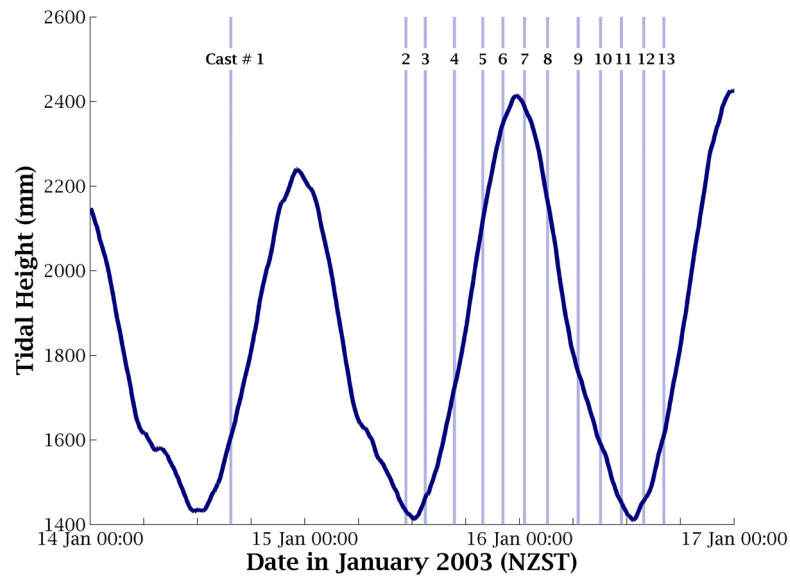


Figure 4.1: Timing of hydrological casts at site HWD-1, with reference to the tidal height measured at Scott Base.

## 4.1 Ice shelf site #1 - HWD-1

A total of thirteen hydrological profiles were collected at HWD-1, covering more than one tidal cycle (see fig. 4.1). The first profile was removed from the analysis because it was collected nearly a day earlier than those following. The range of the characteristics observed were 34.35 to 34.72 psu (practical salinity units) for salinity, and  $-1.942$  to  $-1.876^{\circ}\text{C}$  for temperature.

The structure of the profiles through the water column was fairly constant throughout the tidal cycle, particularly in salinity. At these temperatures, density has a far greater dependence on salinity than temperature, so that for a water column where no static instabilities exist, the salinity profile will increase monotonically to the seafloor. This was observed in every profile (see fig. 4.2) with a rapid increase in salinity over the first  $\sim 200$  m BSL, followed by a more gradual increase to 34.71 psu at the seafloor. Variation was apparent, particularly in the top 200 - 250 m BSL, whereas only minor, short-lived features were observed below this. A progressive increase in salinity was observed in the lower few meters of the hole in the ice shelf. This feature shifted higher as time progressed, implying salt rejection as the hole refroze.

A general structure for the temperature profiles persisted through the series of casts,

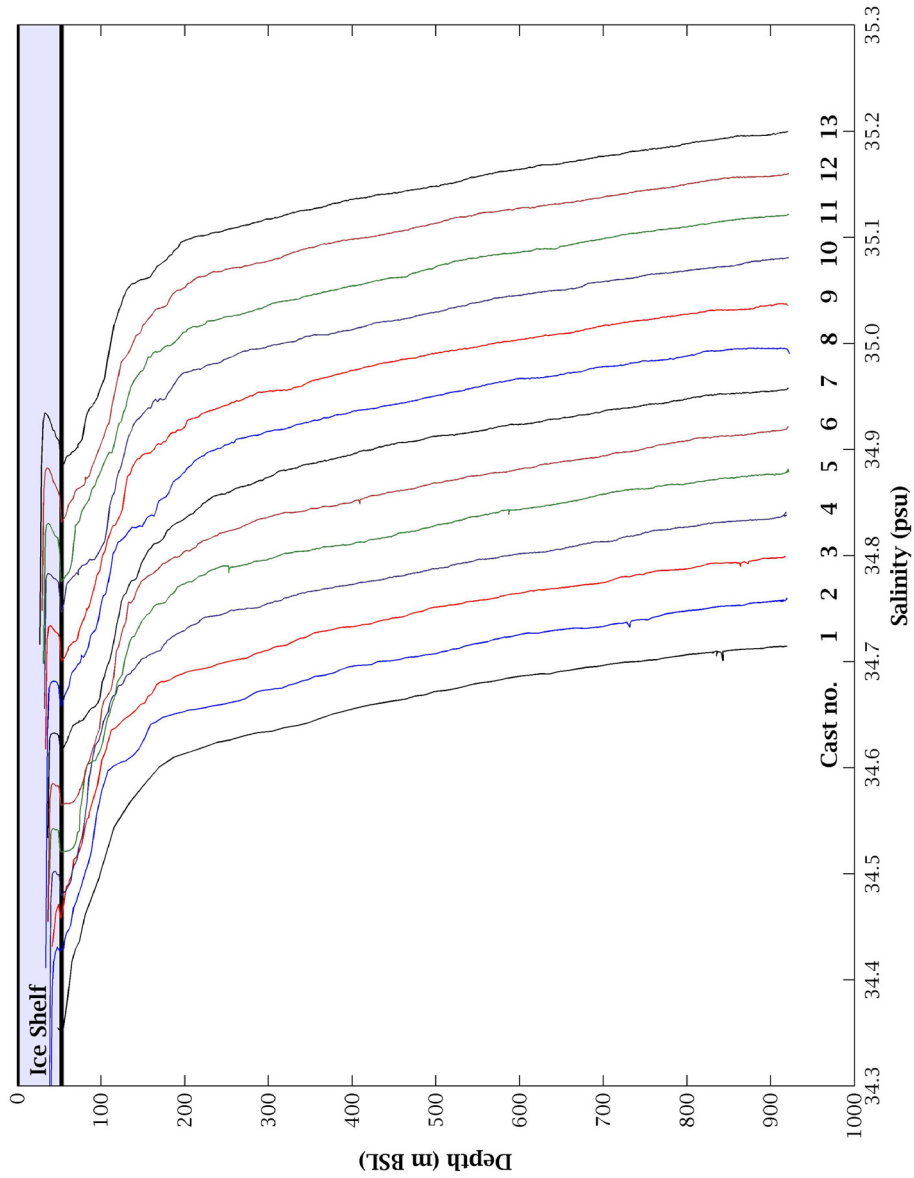


Figure 4.2: Profiles of salinity collected at HWD-1 approximately 2.5 - 3 hours apart. Casts are offset from each other by 0.04 psu, with cast #1 shown with no offset. The casts are coloured differently to aid identification across the boundary at the base of the ice shelf, represented by blue shading. Values shallower than the ice shelf base represent measurements from within the access hole.

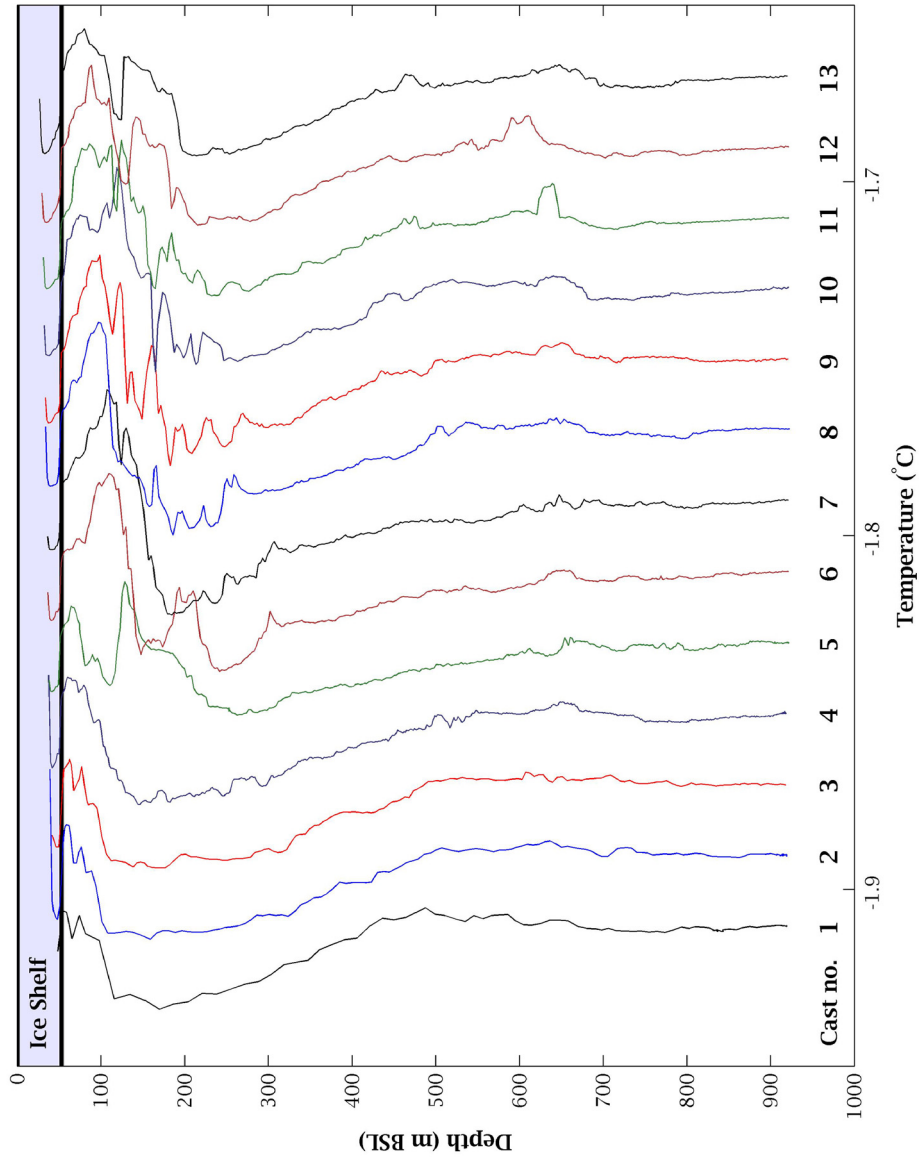


Figure 4.3: Profiles of potential temperature collected at HWD-1 approximately 2.5 - 3 hours apart. Casts are offset from each other by 0.02°C, with cast #1 shown with no offset. The casts are coloured differently to aid identification across the boundary at the base of the ice shelf, represented by blue shading. Values shallower than the ice shelf base represent measurements from within the access hole.

although greater variation than for the salinity profiles was observed (see fig. 4.3). The structure appeared stable over casts #1 to #4, with cast #5 introducing variation to the top 250 m BSL, superimposed on the underlying structure. Features within this layer could be observed evolving with subsequent casts. The variation could not be related to the diurnal tidal cycle, as repetition was not observed in equivalent parts of the cycle. For example, casts #2 and #11 were taken just before low tide, but structure in these two temperature profiles were not related.

The temperature at the base of the ice shelf was, averaged over the 12 casts,  $0.019^{\circ}\text{C}$  below the *in-situ* freezing temperature. This was equivalent to freezing on to the ice shelf at a rate equivalent to  $0.88\text{ m yr}^{-1}$  assuming a linear temperature gradient through the ice shelf, and the top surface of the ice shelf at  $-20^{\circ}\text{C}$ . Assuming no heat flux through the ice shelf, the accumulation rate was equivalent to  $0.80\text{ m yr}^{-1}$ .

Beneath the supercooled boundary layer, a warm tongue of water grew and shrank over the 24 hour period. The depth and extent of this warm tongue changed with each cast, but in general it was as much as  $0.03^{\circ}\text{C}$  warmer than at the base of the ice shelf, deepening over time to  $\sim 200\text{ m BSL}$ . This feature persisted throughout the series of casts, with a lifespan longer than a diurnal tidal cycle. The warm feature was underlain by a cold tongue of water which extended down a further  $\sim 150\text{ m}$ . The coldest water observed was  $-1.94^{\circ}\text{C}$ , within this cold tongue.

Below this, the temperature structure was fairly consistent over the series of profiles, gradually increasing in temperature down to the seafloor at  $-1.91^{\circ}\text{C}$ . A slight cold shift at  $\sim 600\text{ m}$  may have been caused by cool water which had become trapped in the channel, which descends to depths around  $300\text{ m}$  greater than nearby locations (see fig. 2.1). In two consecutive casts - #11 and #12, corresponding to low tide - warm features were observed at the same depth of  $\sim 600\text{ m BSL}$ , which could represent benthic flow from one of the surrounding areas.

The highest salinity water mass, being the densest, was observed at the seafloor. Definitions of High Salinity Shelf Water (HSSW) for the Ross Sea (Jacobs et al., 1985), indicate that the base of the water column was within the temperature range of HSSW. With salinity of  $34.72\text{ psu}$ , this water was too fresh to be identified as HSSW ( $34.78 - 34.89\text{ psu}$ ). The most likely possibility for the formation of the observed water mass is HSSW

from the Ross Sea mixing with fresher water at the surface freezing temperature (see fig. 4.7).

To further investigate the temporal variation of the water masses, the anomalies of each profile were found by comparing temperature and salinity to mean profiles, finding the difference at each 1 m depth interval. The anomalies in the top 300 m of the water column were averaged in 5 m depth bins in order to understand the behaviour of different layers. In general, variations in salinity and temperature were observed to be approximately out-of-phase, and they allowed narrow layers to be identified.

Two examples show this pattern for a typical narrow depth range: A steady rise in temperature was matched by a steady drop in salinity over the flood tide - casts #2 to #7 - for the 45 m thick section from 75 m BSL to 120 m BSL. Similarly, the 40 m thick section from 105 m BSL to 145 m BSL experienced a sharp rise in salinity and drop in temperature evident between casts #7 and #8.

The behaviour of temperature and salinity of casts #8 to #13 were not as highly related, with a steady increase in salinity, but an apparently cooler intrusion in the otherwise steady decrease in temperature. Examining these anomalies in 5 m bins revealed that this departure was due to a large drop in temperature for the short section of the water column between 60 and 100 m BSL, and therefore probably represented a cold intrusion at this depth.

In both temperature and salinity profiles, cast #5 represented a change in behaviour, as it introduced a fresher water feature to replace the saline one, accompanied by a warmer tongue to replace the cooler one. Profiles from this cast were collected in the middle of the flood tide which, extrapolating from the ADCP data analysis, was probably a period of sustained flow to the east or north-east.

## **4.2 Ice shelf site #2 - HWD-2**

Ten profiles of temperature and salinity were collected at HWD-2, covering one diurnal tidal cycle (see fig. 4.4). The range of water characteristics observed at this site were 34.41 to 34.72 psu for salinity and -1.932 to -1.884°C for temperature.

A salinity structure similar to that from the HWD-1 profiles was observed at HWD-2 (see fig. 4.5). Salinity increased almost monotonically to 34.72 psu at the seafloor, with a more rapid increase within  $\sim 200$  m of the base of the ice shelf. A fresher layer appeared at the seafloor in three consecutive casts, casts #6 - #8, representing a period of  $\sim 7 - 9$  hours. This feature is almost certainly a result of instrument error, and possibly represents the instrument having entered the mud at the seafloor at the bottom of the downcast. A fresher signal would have resulted from this for a few metres above the seafloor while the mud was flushed from the cell.

Structure in temperature (see fig. 4.6) was very similar to the structure at HWD-1, with the same underlying pattern of a persistent warm tongue overlying a cold tongue, and gradual increase to  $-1.91^\circ\text{C}$  at the seafloor. The whole structure appeared shifted down by  $\sim 80$  m, compared to HWD-1, corresponding to the deeper draft of the ice shelf at HWD-2. The level of variation was significantly less than at HWD-1, although significant features could be observed evolving over consecutive profiles. For example, the warm feature first observed in cast #5 at  $\sim 300$  m BSL, grew in size and descended through the water column through to the final cast, #10.

At this site, the temperature at the base of the ice shelf was, on average,  $0.052^\circ\text{C}$  above the *in-situ* freezing temperature. This was equivalent to melting at a rate of 2.15 m

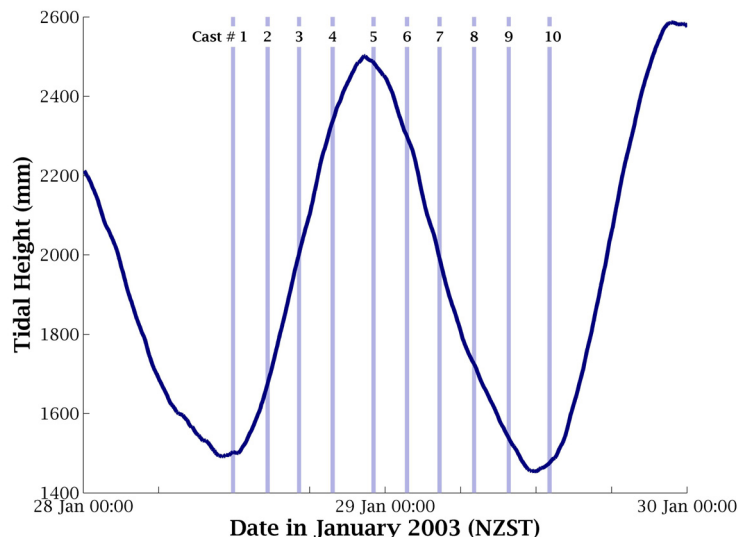


Figure 4.4: Timing of hydrological casts at site HWD-2, with reference to the tidal height measured at Scott Base. The ten profiles collected cover one diurnal tidal period.

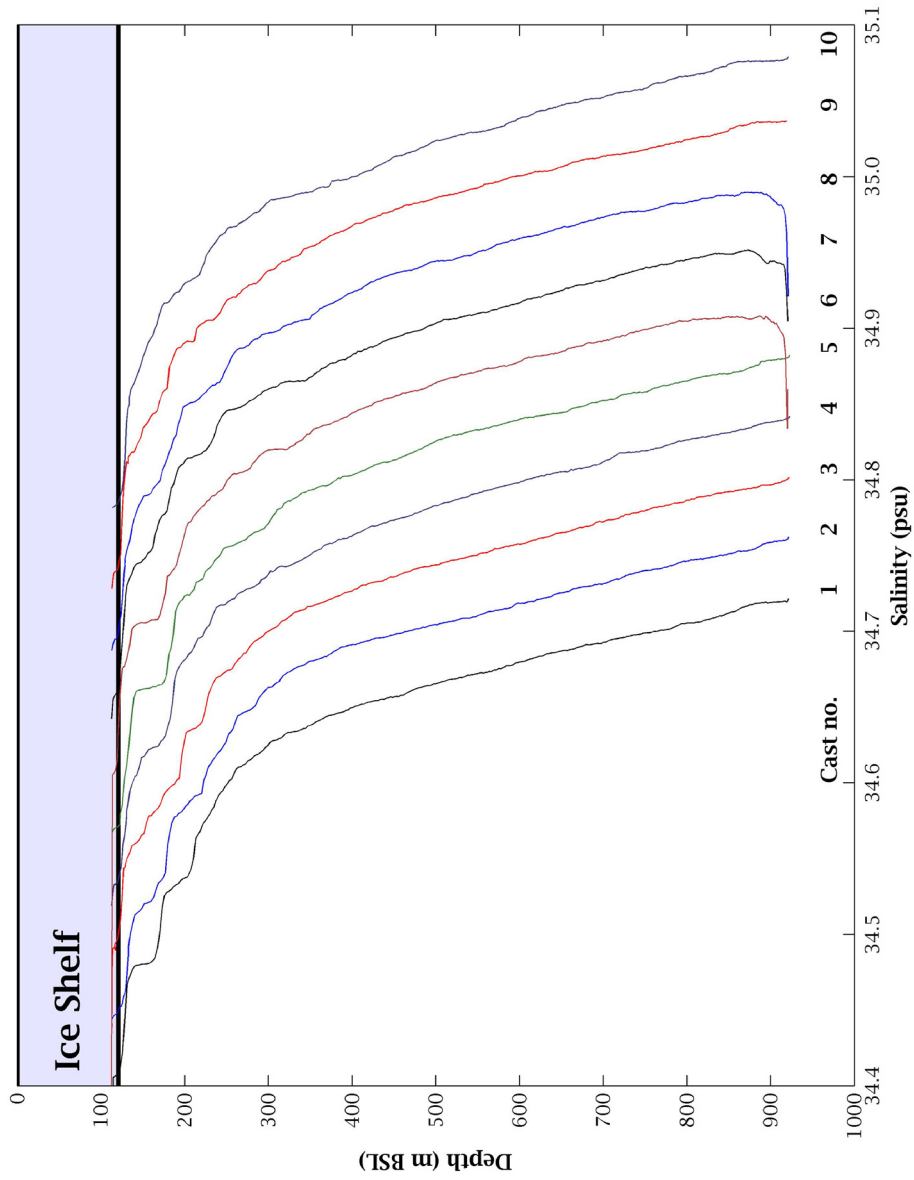


Figure 4.5: Profiles of salinity collected at HWD-2 approximately 2.5 - 3 hours apart. Casts are offset from each other by 0.04 psu, with cast #1 shown with no offset. The casts are coloured differently to aid identification across the boundary at the base of the ice shelf, represented by blue shading. Values shallower than the ice shelf base represent measurements from within the access hole

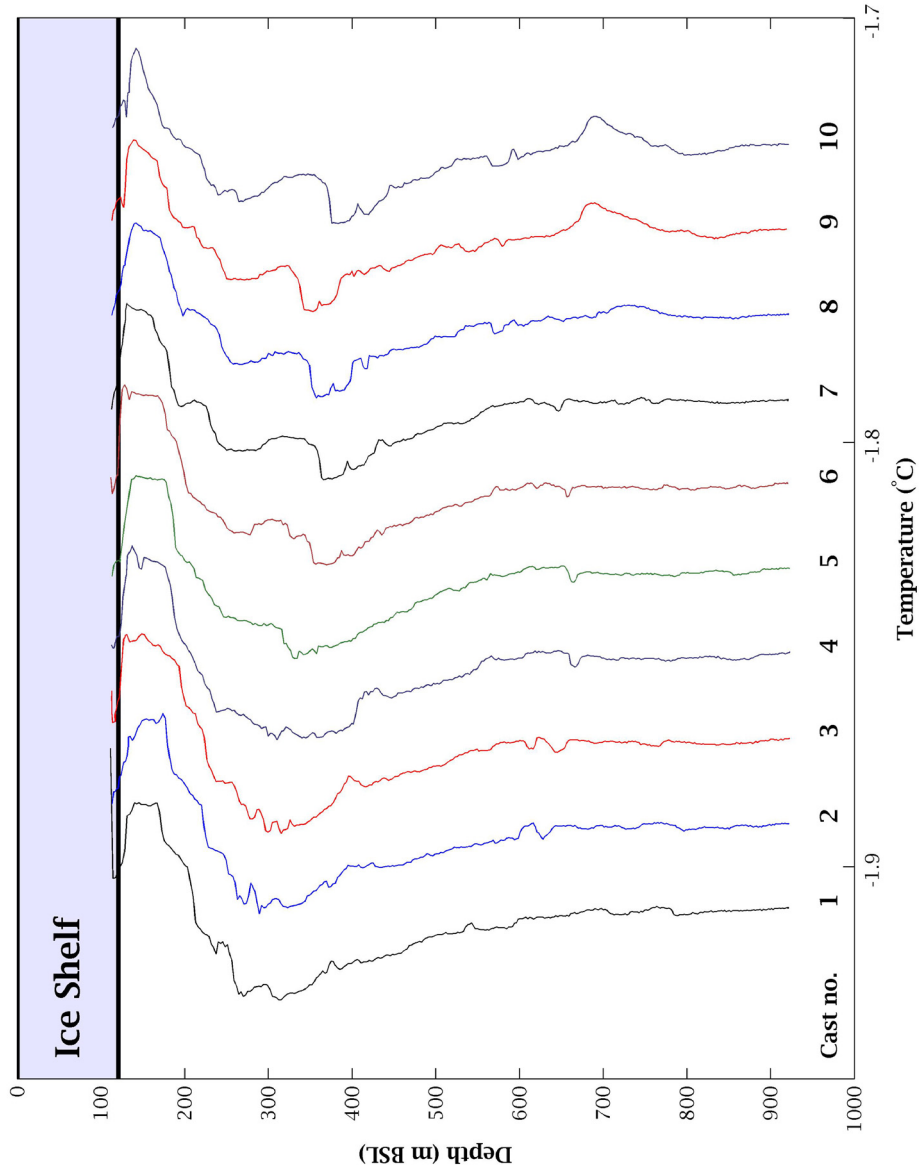


Figure 4.6: Profiles of potential temperature collected at HWD-2 approximately 2.5 to 3 hours apart. Casts are offset from each other by 0.02°C, with cast #1 shown with no offset. The casts are coloured differently to aid identification across the boundary at the base of the ice shelf, represented by blue shading. Values shallower than the ice shelf base represent measurements from within the access hole.

$\text{yr}^{-1}$  assuming a linear temperature gradient through the ice shelf and ice shelf surface temperature of  $-20^{\circ}\text{C}$ . Assuming no heat flux through the ice shelf, the rate of loss was equivalent to  $2.19 \text{ m yr}^{-1}$ .

The variation in temperature and salinity at HWD-2 was not as great as at HWD-1. Several smaller features were identified and were used to observe vertical movement as they were modified in successive profiles. At a depth of  $\sim 700 \text{ m}$ , slightly warmer features were observed in profiles #9 and #10 which, as with the similar warm features at HWD-1, corresponded to a low tide.

The water at the base of the water column for this site again appeared to be HSSW from the Ross Sea (Jacobs et al., 1985) modified by mixing with fresher water at the same temperature.

### 4.3 Comparison between ice shelf sites and with historical sites

The general shape of the temperature and salinity profiles from the two HWD sites were quite similar for all casts, with greater temporal variation observed at HWD-1. Most obviously, the warm tongue beneath the ice shelf was deeper at HWD-2. This was due to the deeper draft of the ice shelf there. Below this, the cooler tongue extended over more of the water column at HWD-2 than at HWD-1, reaching the same temperature at the sea floor. At  $600 - 700 \text{ m}$ , slight warm features mirrored each other at the two sites, appearing in two profiles from each. These were seen in casts #11 and #12 at HWD-1, and casts #9 and #10 at HWD-2, corresponding to low tide at both sites.

The greater range of values, particularly in temperature, observed at HWD-1 indicates this site's closer proximity to an open water source. The distance from HWD-1 to the open water of McMurdo Sound is approximately the length of the tidal excursion, allowing water from beyond the ice front to reach the site within one tidal cycle. In contrast, the distance from the ice front to HWD-2 is approximately twice this length. This implies that the local source of water for the sub-ice shelf cavity is southern McMurdo Sound, with the variation in salinity and temperature first reaching HWD-1, and after subsequent damping reaching HWD-2.

The rates of melting or accumulation at the two sites were significantly different, even though the sites were only  $\sim 8$  km apart. At HWD-1, the average difference between measured temperature and *in-situ* freezing temperature was equivalent to *freezing* onto the ice shelf base at a rate of  $0.88 \text{ m yr}^{-1}$ . A different situation was observed at HWD-2, where the average difference in temperature was equivalent to *melting* at a rate of  $2.15 \text{ m yr}^{-1}$ .

Average basal melt rates for the entire Ross Ice Shelf have been estimated to lie between  $0.12$  and  $0.22 \text{ m yr}^{-1}$  (Holland et al., 2003). The rate of melting observed at HWD-2 was significantly higher than this. This may be attributed to the proximity of the HWD sites to the open water, and the changing gradient of the basal slope, each of which allows for much greater variation in water properties. In addition, the observations at the HWD sites were short, covering one tidal cycle at each, and were made during the height of the Antarctic summer.

Platelet ice was observed at both sites (Nixdorf and Dunker in Barrett et al. (2004)) which, because of its size and shape, was distinct from the slushy ice formed within the access hole. Reflecting the different melt/freeze regimes calculated from the CTD data, the platelet ice observed at HWD-2 was significantly smaller than at HWD-1. It was not clear from the samples of the ice recovered, whether the platelets were formed *in-situ*, or were transported to the site. Platelet ice was also observed in a layer 3 - 4 m thick at the sea-ice site (Barrett et al., 2004).

#### 4.3.1 Profiles at ice shelf sites compared to profiles nearby

The water properties from beneath the ice shelf were compared to the most recently available similar data sets from nearby locations in order to establish their most likely source. For this analysis, only the profiles from HWD-1 were used, as these covered the entire range observed at both sites. CTD data from southern McMurdo Sound ('SMcM' -  $77 - 78^\circ\text{S}$ ,  $165 - 167^\circ\text{E}$ , February 1979) and east of Ross Island ('EoRI' -  $77 - 78^\circ\text{S}$ ,  $168 - 170^\circ\text{E}$ , December 1996 - February 1997, December 1997 - January 1998) were obtained from the National Oceanographic Data Center, <http://www.nodc.noaa.gov> and were viewed using the Ocean Data View (ODV) software available from this website.

Properties of water masses defined for the Ross Sea in Jacobs et al. (1985) as well as the salinity and temperature ranges of another data set was also used in the analysis.

These profiles were from deep under the Ross Ice Shelf, collected through the 'J9' access hole (82°22.5'S, 168°37.5'W), where access to the ice shelf cavity was first obtained during the 1977 - 79 field seasons (Clough and Hansen, 1979; Gilmour, 1979).

As can be seen in figure 4.7, relatively little variation in temperature was observed in the HWD profiles. In contrast, a high degree of variability was observed in the waters from the open water to either side of Ross Island. The variability was restricted to the top 250 m, and with this section of the water column masked, the profiles from both sites closely resembled the HWD profiles.

Using the water mass definitions for the Ross Sea in Jacobs et al. (1985), HSSW was observed at both the SMcM and EoRI locations, but significantly, not at the HWD sites. If flow into the sub-ice shelf cavity was direct and uninhibited from either of these locations, unmodified HSSW should have been observed at the HWD sites, as the depth of the seafloor there is greater than to either the east or west of Ross Island. The water properties from the base of the water column at the HWD sites indicated the presence of HSSW which had been modified by mixing with fresher water at a similar temperature. This can be seen in figure 4.7, where the data from the HWD sites appears quite flat in temperature, with the salinity matching that of HSSW.

It was therefore necessary to look for a sill obstructing the direct flow of HSSW from either the east or west of Ross Island. Such a sill exists at the entrance to the sub-ice cavity at the southern end of McMurdo Sound, while none exists to the east of Ross Island (Davey, 2004). While not conclusive, this does indicate that the water at the base of the sub-ice shelf water column is unlikely to have come from the region to the east of Ross Island, although an unobstructed path exists which would allow its uninhibited flow from there. On the other hand, the sill to the southwest of Ross Island will only block the progression from McMurdo Sound of the densest water, HSSW, and this is the water mass which appears to be missing at the HWD sites. Profiles of the 237 m thick water column at J9, 450 km south of the Ross Ice Shelf front (Clough and Hansen, 1979), revealed thermal structure similar to that observed at the HWD sites. The warm tongue observed beneath the ice shelf at the HWD sites, attributed to their proximity to open water, is missing in the J9 record. Instead, a very cold (-2.16 to -2.14°C) layer existed at the ice shelf base, 380 m BSL, comparable to the tongue observed 200 - 400 m BSL at the HWD sites.

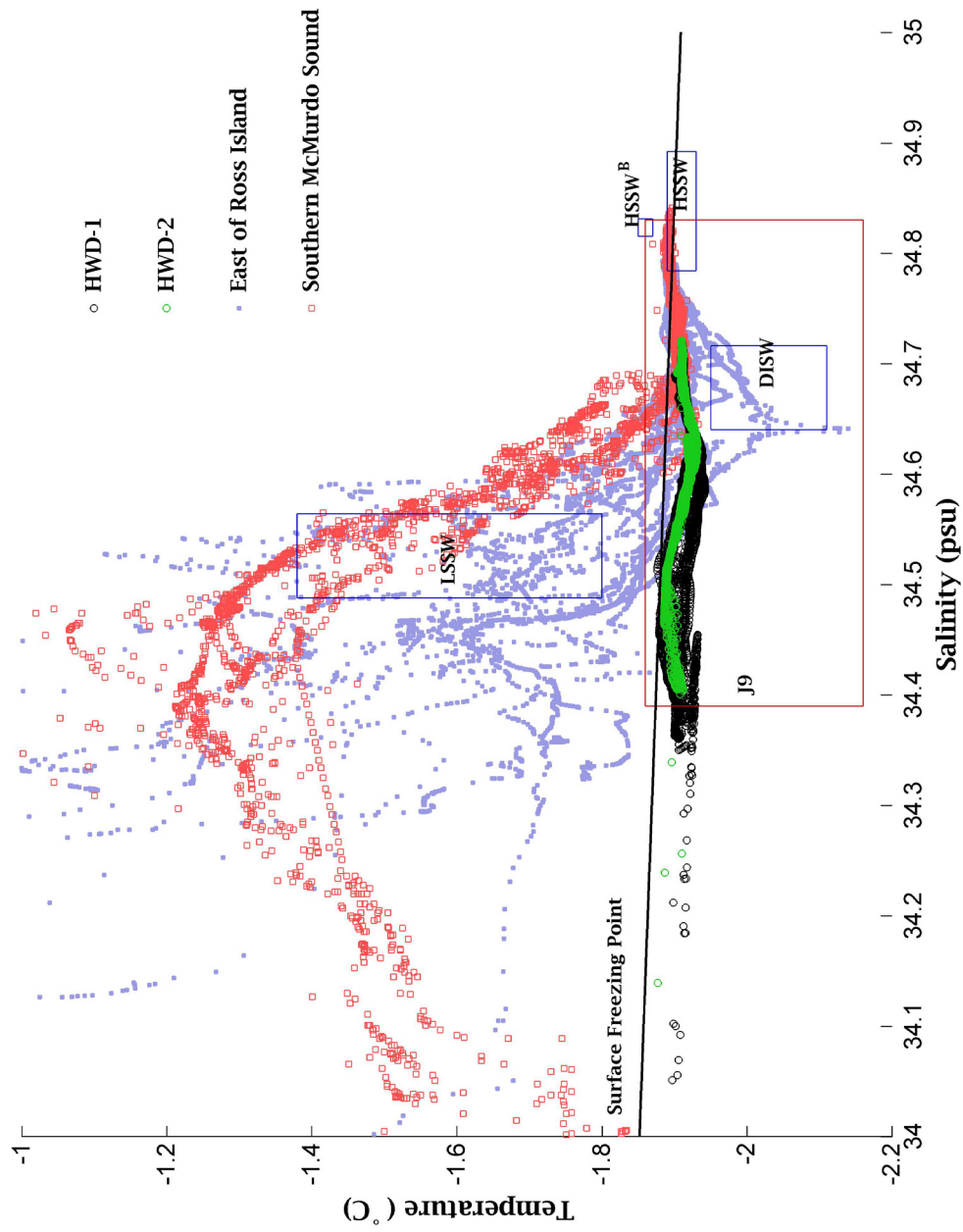


Figure 4.7: Temperature v salinity diagram of data from the HWD sites and nearby locations. Also shown are the relevant water mass definitions for the Ross Sea from Jacobs et al. (1985)

## Chapter 5

# Modelling and sedimentation studies beneath Antarctic ice shelves

Ice shelves form as floating extensions of the Antarctic ice sheet. They are fed by ice streams and glaciers, and sustained by snow accumulation on their surfaces. Ice shelves insulate nearly 40% of the waters on the Antarctic continental shelf from direct atmospheric forcing (see fig. 5.1), creating a unique oceanic environment. The lower boundary layer at the interface of ice and ocean is maintained at the pressure-dependent freezing temperature (e.g., Jacobs et al. (1979)), and allows direct communication between the Antarctic Ice Sheet and the world's oceans.

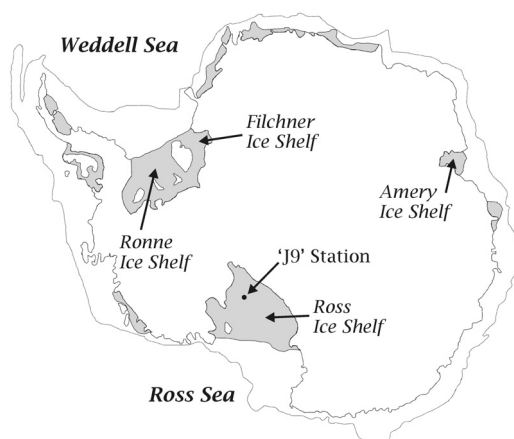


Figure 5.1: Map of Antarctica showing the locations of the major ice shelves, the 'J9' station on the Ross Ice Shelf, and the 1000 m depth contour.

## 5.1 Description of sub-ice shelf processes

Beneath Antarctica’s ice shelves, the thermohaline circulation is effectively a two-dimensional process, which was first described by Robin (1979). In the open water beyond the ice shelves, brine rejection from winter sea ice formation, which effectively doubles the size of the continent is a significant annual signal. This surface brine falls to the seafloor and drains landward following the inland-dipping slope typical of the Antarctic continental shelf. This body of water, called High Salinity Shelf Water (HSSW), is one of the world’s densest water masses. HSSW has been observed in a layer from 500 metres below sea level (m BSL) to the seafloor at site ‘J9’, 450 km from the front of the Ross Ice Shelf (Clough and Hansen, 1979).

Having retained the surface freezing temperature, this water mass is able to melt ice at depth, due to the pressure dependence of the freezing temperature. At the grounding line, where the draft of the ice shelf is deepest, the temperature gradient between the HSSW and the ice shelf base is greatest, so the highest melt rates will occur there (see fig. 5.2).

The newly formed meltwater is buoyant so it flows up the basal slope, retaining the *in-situ* freezing temperature from its formation. As it flows up the slope, it is replaced by ambient seawater, which has the potential to insulate the ice shelf from further melting by HSSW. Vertical mixing by some mechanism (described in section 5.2.1), allows HSSW

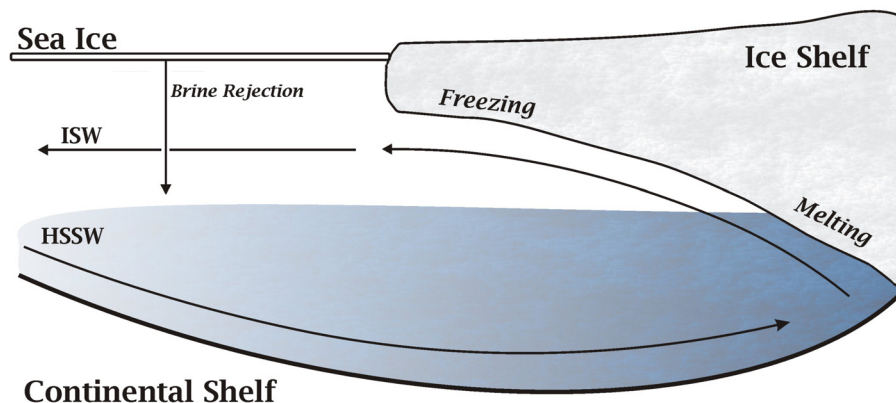


Figure 5.2: Schematic diagram showing the distribution of melting and freezing associated with sub-ice shelf two-dimensional thermohaline circulation. After figure 2b in Robin (1979).

to again come into contact with the ice shelf to resume melting.

Meltwater continues up the ice shelf base, all the while mixing with the HSSW below, until it is neutrally buoyant. At this point, it detaches from the ice shelf and flows out in a plume towards the ice shelf edge, where it can be identified as Ice Shelf Water (ISW) by its temperature, which is below the surface freezing temperature.

ISW has been observed exiting the sub-ice cavities of many Antarctic ice shelves. The signature of ISW can be maintained during distribution into Antarctic coastal waters, and therefore its production is an important feature of any model of the sub-ice shelf circulation.

## 5.2 Modelling the sub-ice shelf environment

The sub-ice shelf cavities of Antarctica have not been extensively studied through direct observation because of access difficulties. Modelling of these environments offers a convenient method of understanding sub-ice processes. Many models, some of which are described below, have been created and applied to this unique environment in an attempt to capture significant features of the ocean circulation beneath the ice.

### 5.2.1 Supply of mechanical energy

In the formation of ISW, a source of mechanical energy is required to drive vertical mixing and allow warm, dense water to come into contact with the ice shelf. As the sub-ice shelf ocean is isolated from direct atmospheric forcing, alternative methods have been investigated in various models.

#### **Shear from tidal currents**

One alternative source of the required energy, investigated by Scheduikat and Olbers (1990), is the small-scale turbulence created at the seafloor and ice shelf base by shear from the tidal currents. Tidal signals are able to propagate beneath the ice shelves, because they float freely on the ocean.

Scheduikat and Olbers (1990) used a 2-layer model, consisting of a turbulent layer immediately below the ice shelf overlying a laminar bottom layer. The characteristics of this bottom layer were maintained with temperature and salinity representative of HSSW,

so that the layer was an infinitely large reservoir of heat and salt. Later this was extended to a 3-layer model, which allowed a homogeneous intermediate layer and also a more realistic representation of the bottom layer with the introduction of turbulence there.

Their experiments showed that the intensity of the tidal currents was of secondary importance for producing melting at the ice shelf base. Of greater importance was the time-variability of the forcing, with a general increase in melt rate for higher variability in the forcing.

The degree of time-variability in the turbulent kinetic energy (TKE) could be controlled with the prescribed shape of the tidal current ellipse. This is determined by the magnitude and ratio of the horizontal velocity components averaged over the tidal cycle,  $U_0$  and  $V_0$ . With isotropic forcing, ( $U_0 = V_0$ ), the two-layer model resulted in an accumulation rate of  $1.3 \text{ cm yr}^{-1}$ . This was shown to be insensitive to changes in both input parameters and, more significantly, the intensity of the tidal forcing.

Once anisotropic forcing ( $U_0 > V_0$ ) was introduced, a cycle of entrainment and detrainment resulted, with a period half that of the tidal forcing. During entrainment, TKE was used to bring warm, salty water up into contact with the ice shelf. Once the available TKE was too low for this to continue, detrainment began, during which the upper layer cooled, but still caused relatively high rates of melting. As the time-variability of tidal forcing was increased, this alternating scheme intensified, resulting in even higher melt rates.

### **Density Gradients**

In considering the unique environment beneath the ice shelves, Hellmer and Olbers (1989) used the interactions at the ice-ocean boundary to drive circulation. Melting and freezing at the ice shelf base created horizontal density gradients, sufficient to drive thermohaline circulation.

The main focus of their study was the cavity beneath the Filchner Ice Shelf (FIS) (see fig. 5.1), using the assumption that the significant part of the flow was along a channel defined by bathymetry and ice shelf topography. This assumption eliminated lateral flow, and restricted density gradients to two-dimensions. The net sub-ice shelf circulation in the model was the result of inflow conditions and the thermohaline processes at the ice shelf

base. To achieve this, where flow was directed into the model region, temperature and salinity values were prescribed from observational profiles obtained close to the ice edge. Otherwise, water characteristics were allowed to exit, unmodified, from the model domain.

The importance of the ice-ocean interaction is highlighted by the fact that time-independent forcing was able to reproduce the major features of the circulation - transport of warm water from the open ocean to the grounding line, high rates of melt at the grounding line decreasing monotonically toward the open boundary, and plumes of ISW exiting from the sub-ice cavity at depth. (Robin, 1979; Jacobs et al., 1979; Jenkins, 1991; MacAyeal, 1985; Scheduikat and Olbers, 1990)

## 5.2.2 Prescribed boundary conditions

### Formulation of processes at the ice-ocean interface

Holland and Jenkins (1999) investigated the importance of having a realistic representation of the flux of heat and salt across the ice-ocean boundary. The processes can be fully described with three equations in three unknowns - melt rate, temperature and salinity at the ice-ocean interface - but can be simplified to 1- and 2-equation formulations.

The one-equation formulation was the result of assuming that relaxation towards the freezing point happens instantaneously. This assumption allowed for no distinction between water properties of the boundary layer, and the ocean beneath. The melt rate was not directly calculated, but was derived from the change in temperature of the mixed layer. An undesirable aspect of this formulation was that derived melt rates were sensitive to prescribed parameters, of which the time-step was the most significant.

A two-equation formulation allowed direct calculation of the melt rate, but was based on the unrealistic assumption that salinities of the interface layer and the ocean beneath were identical. Although unable to directly calculate the temperature at the interface, this formulation produced heat fluxes across the boundary in agreement with measurements made beneath sea ice. The analogous formulation, based on the assumption that the temperature of the boundary layer is identical to that of the ocean beneath, was likewise unable to diagnose salinity at the interface.

Hellmer and Olbers (1989, 1991), reviewed in section 5.2.1, used the full 3-equation formulation with the assumption that the transfer of heat and salt across the boundary can

be described by exchange velocities which remain constant in time. Holland and Jenkins (1999) describe a more complex system which allows these to be calculated as functions of the frictional velocity - a system which was developed for use in modeling ocean circulation beneath sea-ice. However, they point out that the method of adopting constant transfer coefficients (Hellmer and Olbers, 1989, 1991; Scheduikat and Olbers, 1990) produced acceptable results because the coefficients chosen were based on representative rms velocities.

### **Inflow conditions - seasonal forcing at the open boundary**

Hellmer and Olbers (1989) were able to reproduce the major features of the circulation by prescribing measured temperature and salinity profiles at the open boundary, and coupling these to processes at the ice shelf base. Even with no seasonal forcing, the appearance of ISW at the ice edge was cyclic, with the period determined by prescribed topography and inflow conditions. Once seasonality was added, the appearance of ISW took on the periodicity of the inflow conditions, with the resulting pattern of surface water properties being described as an Ice Shelf Edge Oscillator.

The results were similar in Hellmer and Olbers (1991) - an extension of the earlier model to encompass the Filchner and Ronne Ice Shelf (FRIS) cavities and the ventilation channel between the two. Seasonality was added in the form of a small amplitude in the salinity profiles, which varied the density gradient. This allowed detachment of ISW from the ice shelf base at depth and inflow of warmer water into upper levels, helping to sustain the steep density gradient. The depth of outflowing ISW varied seasonally at the open boundary, between the depths of the base of the ice shelf and mid-depths. As a result, the temperature and salinity of the surface waters at the ice front cycled seasonally - reminiscent of the Ice Shelf Edge Oscillator of Hellmer and Olbers (1989).

### **5.2.3 Importance of prescribed topography**

The prescribed shape of the study region, which, for a two-dimensional simulation is limited by the ice shelf base and seafloor, has the potential to affect the circulation greatly. The base of the ice shelf is generally modelled with a smooth upwards slope in a direction away from the grounding line. This mimics the thinning of ice shelves seaward of the grounding line. A typical slope of 1:1000 is used in Hellmer and Olbers (1989, 1991). The basal slope promotes the upwards flow of the buoyant meltwater, helping to drive the circulation and its subsequent appearance as ISW at the ice edge. The depth

to which ISW may be observed is clearly limited by the ice shelf draft at the ice shelf edge.

At station 'J9', 450 km from the front of the Ross Ice Shelf (see fig. 5.1), HSSW was observed in the whole water column below 500 m BSL (Clough and Hansen, 1979). This has led to the assumption in some models (Hellmer and Olbers, 1989; Scheduikat and Olbers, 1990) that this is typical of the entire sub-ice shelf cavity. In these models, prescribed seafloor topography is particularly important, as where the water depth is shallower than 500 m BSL, there is no HSSW in the model, and hence no source for basal melting.

#### **5.2.4 Application to McMurdo Ice Shelf at Windless Bight**

The bathymetry of Windless Bight is dominated by a trough 300 m deeper than the surrounding areas (see fig. 2.1). The trough lies north of Black and White Islands, and parallels Hut Point Peninsula, Ross Island. The flow in this area is effectively constrained along a two-dimensional path between the islands, which has been modelled as a curved, two-dimensional vertical slice, with the upper boundary defined by the ice shelf topography. The slope of the ice shelf base was increased to 1:100, to reflect the steeper topography near the ice shelf front.

The ice shelf thickens along the channel, so that the two-dimensional thermohaline model of Hellmer and Olbers (1991) is appropriate for this setting. The time-scale of the variation in seasonally forced experiments was used for investigation of the sediment depositional environment within the model.

### **5.3 Present sedimentation environment**

Windless Bight is known to be floored with sediment over 1000 m thick (Horgan et al., in press). The present accumulation there is very slow with rates of  $0.02 \text{ mm yr}^{-1}$  and  $0.06 \text{ mm yr}^{-1}$  observed at the hot water drill sites, HWD-1 and HWD-2 respectively (Barrett et al., 2004). These rates are comparable with sites in the deep basins off the Victoria Land Coast (Domack et al., 1999).

Comparisons of the surface sediment cored through the HWD holes (Barrett et al., 2004), with cores from the open waters of McMurdo Sound and the Ross Sea (Dunbar et al., 1985, 1998) show similar proportions of biogenic sediment (10 to 30% opaline silica), the rest being terrigenous and mostly clay and silt. This is consistent with the observations

that the net current flow is  $0.03 \text{ m s}^{-1}$  from the open waters of McMurdo Sound to the east-northeast beneath the McMurdo Ice Shelf.

The general circulation pattern on the Ross Sea continental shelf results in the concentration of fine grained sediment in its southwestern sector (Dunbar et al., 1985). The deeper water of this region allows greater deposition of the fine grained material here, since basins act as traps for the sediment, and the slower currents generally observed at depth allows the material to drop out.

Sediment trap studies show that the bulk of the fine-grained material in McMurdo Sound is deposited by means of ‘algal flocs’ (Dunbar et al., 1998), which settle somewhat faster than the individual grains. The flocs are generally broken up on deposition, so that the size of the settling particles, and hence their settling velocities, cannot be measured directly. Dunbar et al. (1998) noted that seasonal floral and isotopic signatures are preserved down to the sea floor in places, and they inferred not more than 100 km of horizontal transport for this material. This maximum distance corresponds to settling at  $30 \text{ m d}^{-1}$ , with the fastest settling by this method estimated at  $120 \text{ m d}^{-1}$ .

Fecal pellets are the other main type of material deposited in McMurdo Sound, with highest fluxes occurring during the summer. Contributing up to 70% of the mass deposited (Dunbar et al., 1998; Langone et al., 2003), they are even more locally derived, with estimated horizontal transport of 4 to 50 km. These distances have been calculated from settling velocities of 60 to  $400 \text{ m d}^{-1}$  (Dunbar et al., 1998).

High sediment flux events through the top- and mid-water column are dominated by physical processes which disturb the water column. From a year-long mooring in the southwestern Ross Sea, Langone et al. (2003) reported that the onset of significant flux events, indicated by transmissometry data, coincided exactly with large changes in temperature and salinity in late summer (February/March). This demonstrated that high flux events are triggered by predominantly physical processes, and are able to affect significant portions of the water column simultaneously.

Flux at depth is consistently higher than near-surface flux (Dunbar et al., 1991, 1998; Langone et al., 2003), and is roughly equivalent to the amount of material delivered to the seafloor (Dunbar et al., 1998). Dunbar and Leventer (1987) estimated that the mid-

and deep-water fluxes of 500 to 1000 mg m<sup>-2</sup> d<sup>-1</sup> correspond to accumulation of 1 to 4 mm yr<sup>-1</sup>.

The observed rate of sediment accumulation at Windless Bight (Barrett et al., 2004) is two orders of magnitude lower than this, and may be a consequence of sediment bypassing Windless Bight or post-depositional solution. The surface sediment in both the Ross Sea and beneath Windless Bight includes a small percentage of coarse sand and small pebbles.

Preliminary provenance studies of surface sediment from the two Windless Bight cores, show a mix of grains of basaltic, sedimentary quartz, dolerite, and metasedimentary origin, indicating ultimate sources of both the local McMurdo volcanics and the rocks of the Transantarctic Mountains. In the open waters of McMurdo Sound and the Ross Sea, these are attributed to ice-rafting (Barrett et al., 1983; Dunbar et al., 1985), but their occurrence in sediments beneath Windless Bight has yet to be satisfactorily explained.

## Chapter 6

# Modelling the thermohaline circulation beneath the McMurdo Ice Shelf

The presence of an ice shelf at the top of the water column profoundly affects the circulation of the ocean beneath. The base of the ice shelf forms a solid boundary, insulating the ocean from direct atmospheric forcing but providing forcing of a different type through the exchange of heat and salt across the ice-water interface.

Being on average around 300 m thick, the Antarctic ice shelves presents a significant, and for the most part prohibitive, barrier to direct observation of the water column beneath. With only a modest observational database available, numerical modelling has, to date, been the principal means of understanding the physical processes controlling sub-ice shelf circulation.

### 6.1 Sub-ice shelf circulation at Windless Bight

The flow at Windless Bight is dominated by a curved submarine channel which follows the south coast of Ross Island. A two-dimensional model oriented along the axis of the channel was used to capture the significant features of flow there (see fig. 6.1). The sub-ice shelf thermohaline ocean model (Hellmer and Olbers, 1991), developed for the Filchner Ice Shelf ocean cavity, was adapted for the McMurdo Ice Shelf cavity. It was designed to incorporate annual forcing over a number of years, and was also used for investigating the depositional environment.

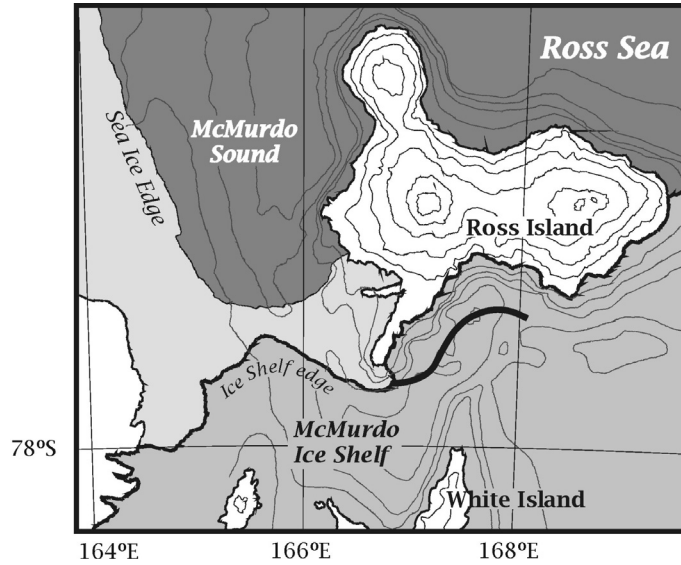


Figure 6.1: Map of the McMurdo Ice Shelf showing the section along the channel (solid black line) which was the model domain.

The McMurdo Ice Shelf thickens in a direction parallel to the channel axis, so this model, designed for a vertical slice perpendicular to the ice front, was appropriate for investigating throughflow. The model was forced at the open boundaries using profiles of salinity and temperature (see figures 6.2 and 6.3), based on year-long observations from southern McMurdo Sound (Littlepage, 1965).

### 6.1.1 Model description

Large-scale motion of the sub-ice ocean was described by the Boussinesq and hydrostatic approximations to the momentum balance equation (for full details see appendix A). Horizontal gradients in the normal component and Coriolis terms were neglected due to the restriction to two-dimensions. Thermohaline processes at the ice shelf base were coupled to the sub-ice shelf circulation using the imposed condition of a boundary layer of water at the ice-ocean interface at the *in-situ* freezing temperature.

The circulation was governed by the vorticity equation in the  $y/z$  plane,

$$\Psi_{zzt} + (v\Psi_{zz})_z = g\rho_y + A_H\Psi_{zzyy} + A_V\Psi_{zzzz}, \quad (6.1)$$

where the streamfunction,  $\Psi$ , was defined in terms of the velocity components  $v$  and  $w$  by

$$v = \Psi_z \text{ and } w = -\Psi_y. \quad (6.2)$$

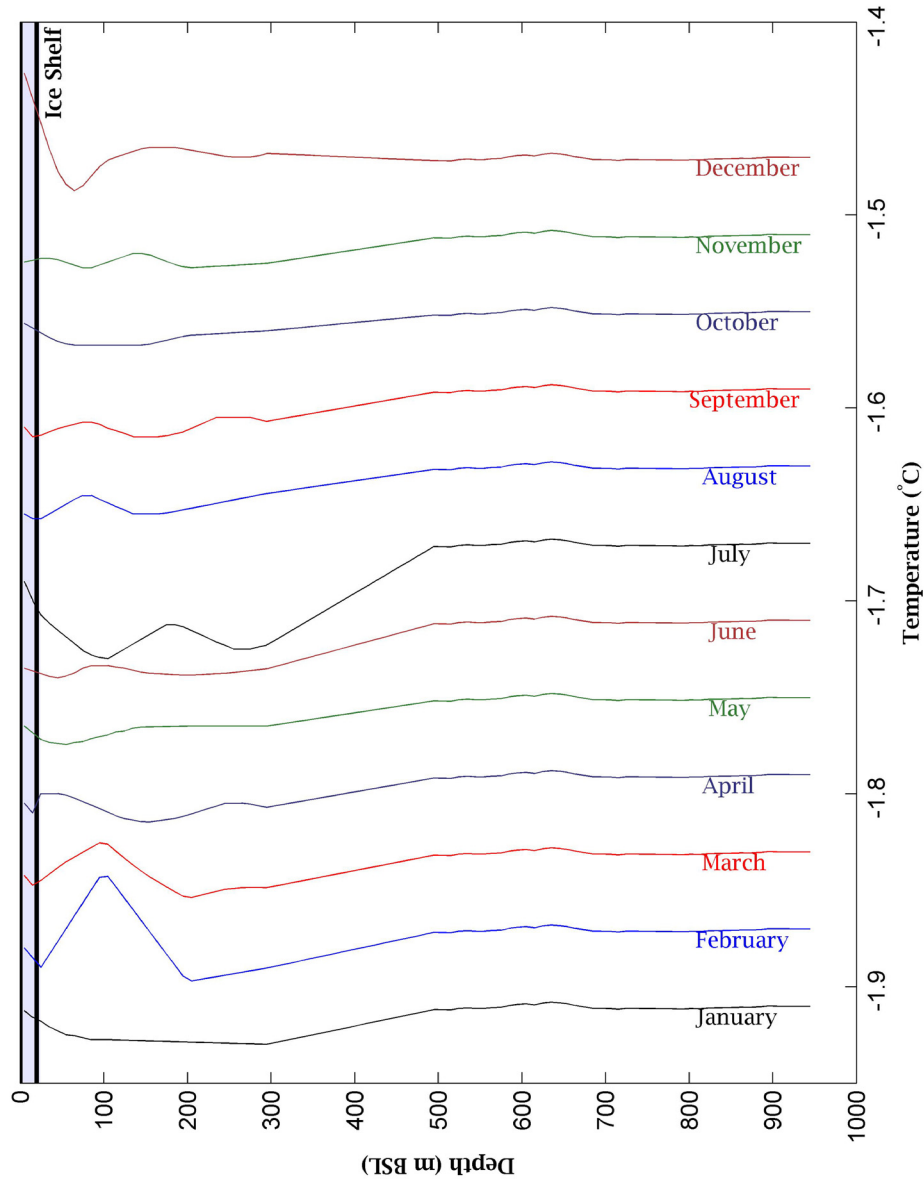


Figure 6.2: Monthly temperature profiles used to seasonally force the model at the western end of the domain, adapted from Littlepage (1965). The average of these profiles was used to apply constant forcing at the eastern end of the domain deep under the ice shelf. Profiles are offset from each other by 0.04°C, with no offset for the January profile. Temporal variation is restricted to the top 500 m, with the draft of the ice shelf at the McMurdo Sound end of the domain shown in blue.

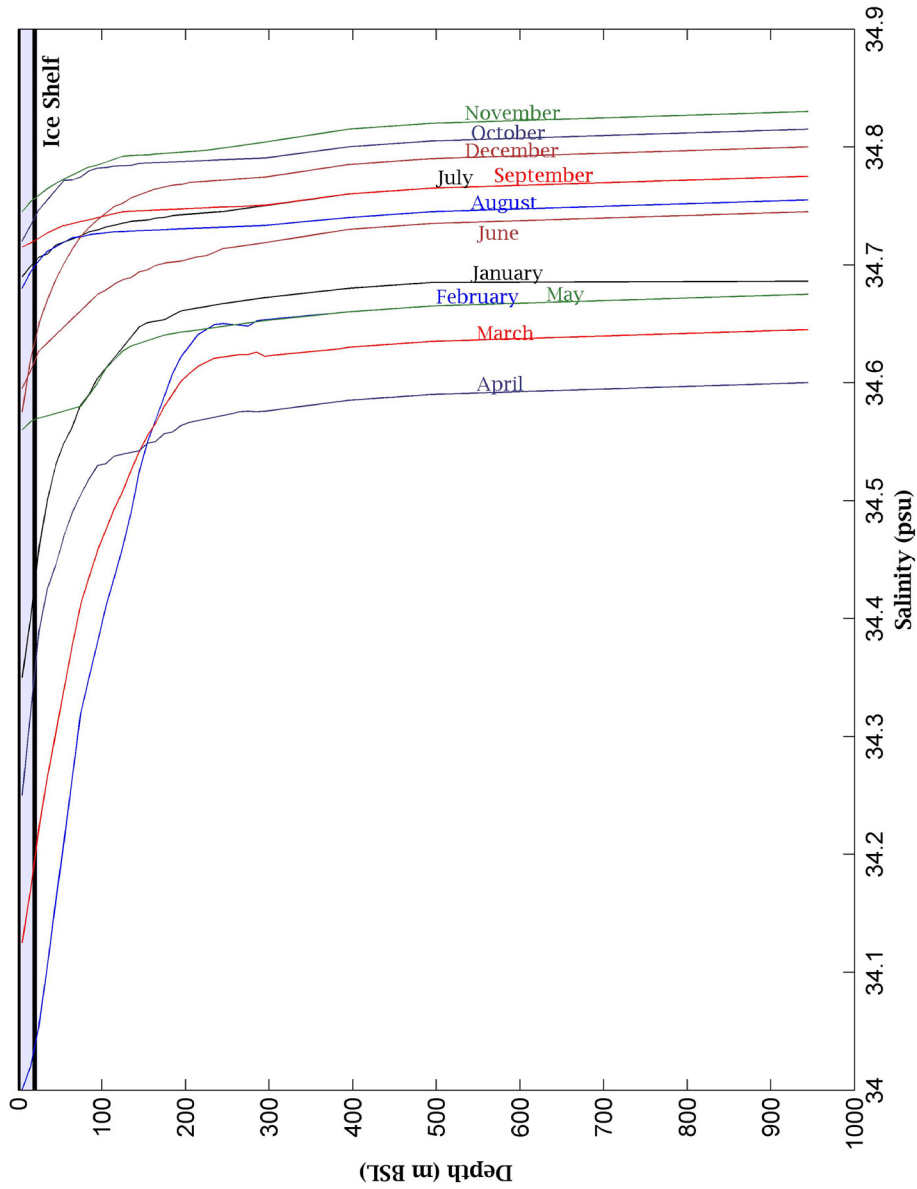


Figure 6.3: Monthly salinity profiles used to seasonally force the model at the western end of the domain, adapted from Littlepage (1965). The average of these profiles was used to apply constant forcing at the eastern end of the domain deep under the ice shelf. Profiles are not offset from each other showing the changing salinity structure resulting from sea ice formation. The draft of the ice shelf at the McMurdo Sound end of the domain is shown in blue.

$A_H$  and  $A_V$  were the horizontal and vertical diffusivities, accounting for sub-grid scale turbulence. The term  $g\rho_y$  represented the density torque, coupling the thermohaline processes to the horizontal density gradients. Within this baroclinic formulation, it was the horizontal density gradients which generated vorticity and initiated thermohaline circulation in the model.

The streamfunction was separated into its circulating part,  $\theta$ , and throughflow part,  $\phi$ , which were solved for separately, i.e.  $\Psi = \theta + \phi$ . These parts represented homogeneous and non-homogeneous streamfunctions, uncoupled via the relationship  $\Psi_z = 0$ .  $\theta$  satisfied equation 6.1, with homogenous boundary conditions and interior terms.

$\phi$  was also the solution of equation 6.1 with inhomogeneous boundary conditions and zero interior terms. Along the seafloor,  $\phi$  was set to zero, and at the ice shelf base,  $\phi = \gamma(t)$ . The function  $\gamma(t)$  represented total transport through the channel and incorporated the pressure gradient between the open ends of the domain (see Appendix A). It was through application of  $\gamma$  at the boundary that the pressure gradient between the channel ends was incorporated into the circulation.

Active and passive tracers were described by

$$X_t + (vX)_y + (wX)_z = K_H X_{yy} + K_V X_{zz} + C \quad (6.3)$$

where  $X$  represented potential temperature, salinity or sediment concentration, and  $K_H$  and  $K_V$  were horizontal and vertical eddy diffusivities.  $C$  represented convection, modelled by a vertical mixing scheme which removed all static instabilities within the water column in a single pass (Rahmstorf, 1993).

The ice shelf was assumed to be in a steady state. Although within the model, rates of melting or accumulation were calculated, these amounted to less than 1 m per year, so the variation in ice shelf thickness was not taken into account. In addition, no account was taken of the lateral movement from the seaward advance of the ice shelf, typically of the order of 100 m yr<sup>-1</sup> for Antarctic ice shelves.

### Flux of heat and salt at the ice-ocean boundary

The exchange of heat and salt between ice and ocean was an integral part of the dynamics, creating the initial horizontal density gradients at the interface (see fig. 6.4). This

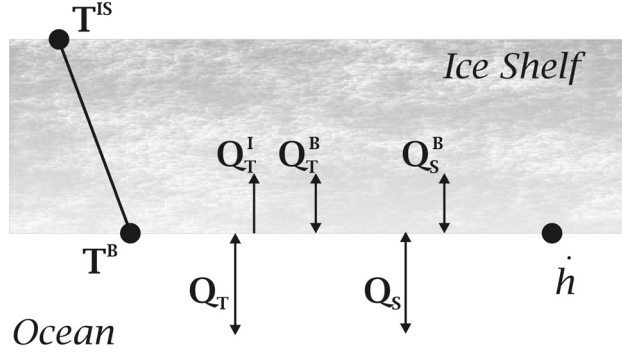


Figure 6.4: Schematic diagram showing heat and salt fluxes across the ice-ocean boundary. After figure 1 in Hellmer and Olbers (1989).

boundary layer was assumed to be at the *in-situ* freezing point ( $T^F$ ), based on observations from the central Ross Ice Shelf at the ‘J9’ station (Jacobs et al., 1979).

The pressure-dependent freezing point at the ice shelf base was expressed as a function of salinity ( $S^B$ ) and pressure ( $p$ ):

$$T^F = aS^B + b + cp \quad (6.4)$$

with constants  $a = -0.057^\circ\text{C}$ ,  $b = 0.0939^\circ\text{C}$  and  $c = -7.64 \times 10^{-2} \text{ }^\circ\text{C MPa}^{-1}$ , following Foldvik and Kvinge (1974).

The heat balance across the ice-ocean interface was described by

$$Q_T - Q_T^B - Q_T^I = 0, \quad (6.5)$$

where  $Q_T$  was the total heat flux across the boundary, and was proportional to the temperature difference between the ice shelf base ( $T^B$ ) and ocean ( $T^W$ ). It was parameterised by,

$$Q_T = \rho_w c_{\rho w} \gamma_T (T^B - T^W) \quad (6.6)$$

(Welander, 1977), where  $\rho_w$  was the sea-water density,  $c_{\rho w} = 4000 \text{ J kg}^{-1} \text{ }^\circ\text{C}$  was the heat capacity of sea-water at  $0^\circ\text{C}$  and  $\gamma_T$  was the turbulent heat exchange coefficient, taken as  $10^{-4} \text{ m s}^{-1}$ .

$Q_T^B$  was the amount of heat lost by the ocean due to melting of glacial ice ( $\dot{h} < 0$ ), or gained due to the formation of ice within the water column ( $\dot{h} > 0$ ), and was paramet-

erised by

$$Q_T^B = \rho_i L \dot{h}, \quad (6.7)$$

where  $\rho_i = 920 \text{ kg m}^{-3}$  was a mean density for glacial ice,  $L = 3.34 \times 10^5 \text{ J kg}^{-1}$  was the latent heat of fusion, and  $\dot{h}$  was the accumulation rate.

$Q_T^I$  represented the molecular heat conduction through the ice, for which a linear temperature profile through the ice was assumed.

$$Q_T^I = \rho_i c_{\rho i} \kappa \frac{T^{IS} - T^B}{D}, \quad (6.8)$$

where  $c_{\rho i} = 2000 \text{ J kg}^{-1} \text{ }^\circ\text{C}^{-1}$  was the heat capacity of ice,  $\kappa = 1.54 \times 10^{-6} \text{ m}^2 \text{ s}^{-1}$  was the thermal diffusivity of ice at  $-20^\circ\text{C}$  (Hobbs, 1974),  $T^{IS}$  was the temperature at the surface of the ice shelf and  $D$  was the thickness of the ice shelf.

The balance of salt across the interface, neglecting the molecular diffusion through the ice, was described by

$$Q_S = Q_S^B \quad (6.9)$$

in which  $Q_S$  was the total flux across the boundary and  $Q_S^B$  was the flux caused by melt-water or brine rejection. These were given by

$$Q_S = \rho_w \gamma_S (S^B - S^W) \text{ and } Q_S^B = \rho_e S^B \dot{h} \quad (6.10)$$

where  $\gamma_S = 5.05 \times 10^{-7} \text{ m s}^{-1}$  was a turbulent salt coefficient,  $S^B$  was the salinity in the boundary layer at the base of the ice shelf, and  $S^W$  was the salinity of the ocean.

All equations were solved numerically by a finite difference scheme with forward differences in time and centred differences in space. One-sided differences were used at horizontal and vertical boundaries.

### 6.1.2 Model configuration

The variables were placed in space on a special grid (see fig. 6.5), which was modified slightly from the configuration used in Hellmer and Olbers (1989, 1991). The edge of the domain was defined by streamfunction values, with the condition that  $\theta = 0$  along solid boundaries. Horizontal and vertical velocities vanished along solid boundaries, and flow across the open boundaries was taken to be strictly perpendicular to the boundary, so

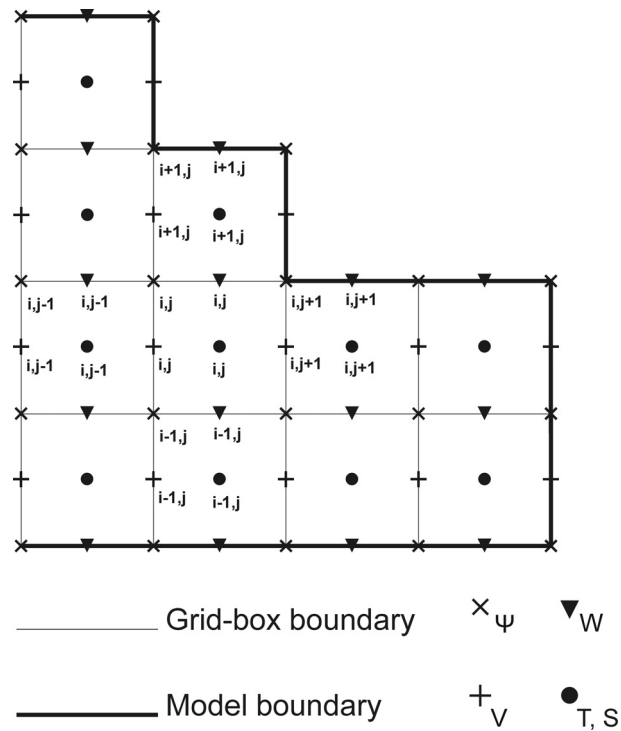


Figure 6.5: The variables  $v$ ,  $w$ ,  $\Psi$ ,  $T$  and  $S$  staggered in the  $y/z$  plane.

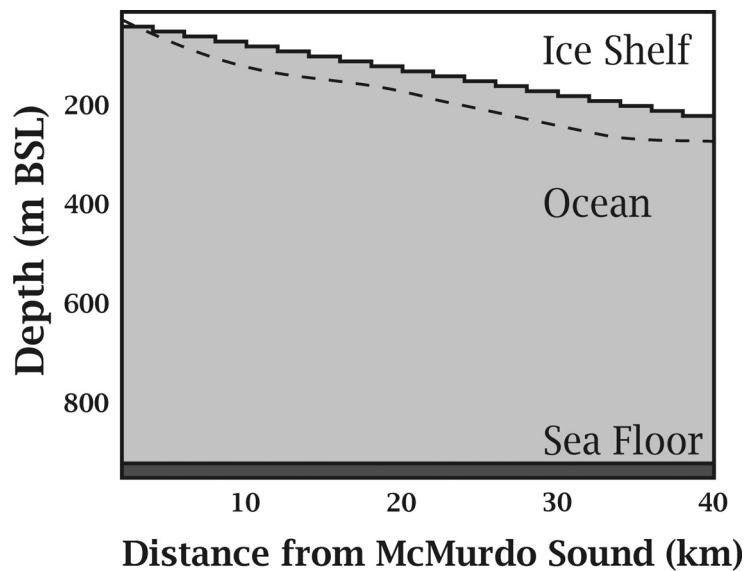


Figure 6.6: Plot of standard configuration for model experiments. Resolution of horizontal and vertical steps can be seen with sloped ice shelf in white at top. The approximate topography of the ice shelf is shown with the broken line. Sea bed is shown in darker grey at the bottom of the figure.

that no vertical velocity component existed there.

Spatial increments  $\Delta Y$  and  $\Delta Z$  were constant over the entire domain. The standard channel length was 40 km long, extending eastwards from McMurdo Sound (see fig. 6.1). At the McMurdo Sound end of the domain, the ice shelf draft was 20 m, with the water column extending for a further 900 m below this. The slope of the ice shelf was 1:200, much steeper than that used in Hellmer and Olbers (1991), reflecting the proximity to open water, and the generally steeper basal slope near the front of ice shelves. The basal slope of the ice shelf and seafloor topography were approximated by steps having the resolution of  $\Delta Y$  and  $\Delta Z$  (see fig. 6.6).

The observed ice shelf topography is shown in figure 6.6. Where the modelled ice shelf draft is deeper, more meltwater will be produced by the model, and vice versa, due to the pressure dependence of the *in-situ* freezing temperature. Where the modelled ice shelf base is not as steep as the observed topography, the buoyancy-driven transport of this meltwater is slower, with lower velocities there.

The domain was open, allowing exchange with the ocean, at both ends. For flow directed out of the domain, water was unmodified as it exited. Where flow was directed into the domain, boundary profiles of temperature and salinity were forced towards the profiles prescribed just outside the boundary. This was achieved through adjusting the profiles on the boundary by an amount proportional to the existing difference across the boundary.

Seasonal variation was applied by varying the temperature and salinity profiles at the McMurdo Sound end of the domain. For flow directed into the model domain, the boundary profiles were smoothed towards the seasonally varying profiles by

$$\frac{\partial X}{\partial t} = \frac{1}{\alpha}(X - X_{forcing}) \quad (6.11)$$

where  $X$  was the boundary profile for temperature or salinity,  $\Delta T$  was the timestep, and  $\alpha$  was the restoring time. Relatively strong forcing -  $\alpha \equiv 4$  days - was applied there in order to create strong seasonal signals within the domain. Constant profiles were used to weakly force at the eastern end, deep under the ice shelf. Weak forcing -  $\alpha \equiv 16$  days - was applied there simply to keep domain values reasonably close to average profiles. This level of forcing reflects the lack of observational data from this part of the Ross Ice Shelf. This also allowed the model greater freedom to respond to seasonal variation from the McMurdo Sound end.

The prescribed air temperature at the top of the ice shelf, was constant over the whole domain at  $-20^{\circ}\text{C}$ , following Hellmer and Olbers (1989) and Schwerdtfeger (1970).

### **6.1.3 Spin-up phases**

The first of two spin-up phases ran for one year of model time, during which the model domain was completely self-contained with no exchange of water properties across the open boundaries. The ocean was initially set with a homogeneous temperature and linear vertical gradient in salinity to ensure a stable water column. All other variables were set to zero, so that the ocean was initially at rest. During this first year, model dynamics were able to adjust to fluxes of heat and salt at the ice-ocean boundary, setting up the basic thermohaline circulation.

During the second phase, the vertical boundaries were opened and the interior domain forced towards average McMurdo Sound profiles of temperature and salinity from both ends of the domain. This phase lasted for ten years of model time, resulting in a stable, self-consistent environment from which to begin experiments (Chapter 7).

# Chapter 7

## Model experimentation

The model was developed to explore current flow along a broad, 40-km-long channel, in 900 m of water beneath the McMurdo Ice Shelf (described in section 6.1.2). The dependent parameters in this model were tuned to provide results to match appropriate, independent data sets. Spatial increments (10 m cells) in the vertical direction allowed resolution of ice shelf and sea floor topography, while the 2 km cell size in the horizontal provided a distance over which the types of sediment recovered from the site can be transported. The seasonal forcing experiments each ran for several years, using a relatively long timestep of 30 minutes with restoring equivalent to 4 days at the western end of the domain.

### 7.1 Sensitivity analysis - model dynamics

Initially, the model sensitivity to various parameters was tested. The tests were based on a standard experiment following the spin-up phases (see previous section), with five years of seasonal forcing for the configuration of a sloped ice shelf and flat sea floor (for monthly profiles used to force the model see figures 6.2 and 6.3).

In most cases, the net throughflow,  $\gamma(t)$ , was used diagnostically to test the sensitivity of the model to the parameter under consideration.  $\gamma(t)$  was defined so that positive  $\gamma$  represented transport through the channel from the western end to the eastern end. Successful tests showed seasonal variation in  $\gamma(t)$  after about one year. For many tests, the first year involved a rapid adjustment to the seasonal forcing, resulting in reduced, or possibly negative, throughflow in the channel, and large fluctuations in the active tracers, temperature and salinity.

### 7.1.1 Standard settings

A standard experiment was set-up as a comparison for subsequent tests. The values assigned for the standard experiment are shown in table 7.1, and were used as default settings for every experiment. (For animations of this experiment see ‘*Standard Experiment*’ on the CD inside the back cover.)

In the standard model,  $\gamma(t)$  settled into a seasonal cycle after one year. This is demonstrated by an annual pattern of peaks and troughs. The average value for  $\gamma(t)$  was  $\sim 1.0 \text{ m}^2 \text{ s}^{-1}$ , with a peak-to-peak amplitude  $\sim 1.5 \text{ m}^2 \text{ s}^{-1}$ . The range of temperature and salinity values seen within the model domain ( $-1.94$  to  $-1.91^\circ\text{C}$  and  $34.60$  to  $34.80$  psu) was much narrower than the range of values in the boundary forcing, which was  $-1.97$  to  $-1.87^\circ\text{C}$  and  $34.00$  to  $34.83$  psu. The freshest water created by the model was due to interaction between ice shelf and ocean in the deepest part of the cavity, producing meltwater, rather than directly from the profiles used to force the model at the open boundary.

Table 7.1: Standard settings used for experiments testing the sensitivity of the model dynamics to various parameters

$K_H$	$K_V$	$\Delta Y$	$\Delta Z$	$\Delta T$	$\alpha_L$	$\alpha_R$
( $\text{m}^2\text{s}^{-1}$ )	( $\text{m}^2\text{s}^{-1}$ )	(m)	(m)	(mins)	(days)	(days)
$1 \times 10^2$	$1 \times 10^{-4}$	2000	10	30	28	112

A continuous flow of fresh meltwater up the base of the ice shelf was formed, causing a circulation cell of anticlockwise flow to develop at the ice shelf base (see fig. 7.1). This cell indicated that the flow of the lighter meltwater up the base of the ice shelf was replaced by water drawn into the domain at deeper levels. The cell changed size several times each year, in general dominating the domain over the spring-early summer months and receding during winter. The cell was always present to a distance of at least 16 km from the western end of the domain. The deeper parts of the domain fluctuated between clockwise and anticlockwise cells three times annually, allowing a shear zone in the horizontal velocity to develop annually at  $\sim 150 - 300$  m.

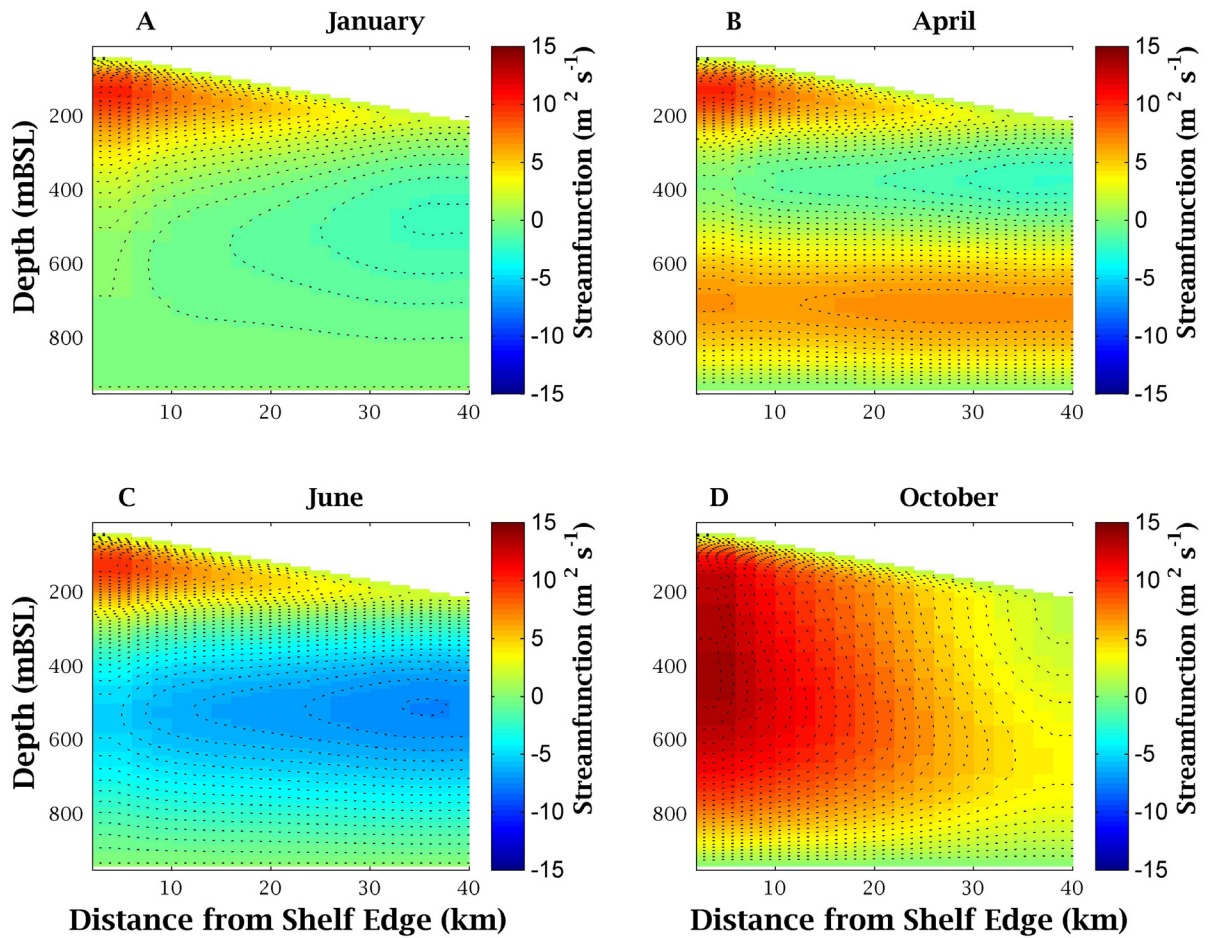


Figure 7.1: Plots of streamfunction values at different times of the year from the simulation with standard settings. Flow was parallel to contour lines, with clockwise flow indicated by blue streamfunction values, anticlockwise with red. The circulation cell which transported fresh meltwater up the base of the ice shelf was persistent throughout the year, for all experiments.

The tail of the anticlockwise cell, at the deep end of the ice shelf, gave rise to a nearly continuous downward flow at this position. This became a location where temperature and salinity signals moving along the base of the ice shelf were allowed greater access to the domain beneath, and where sediment was transported down to be deposited at the sea floor.

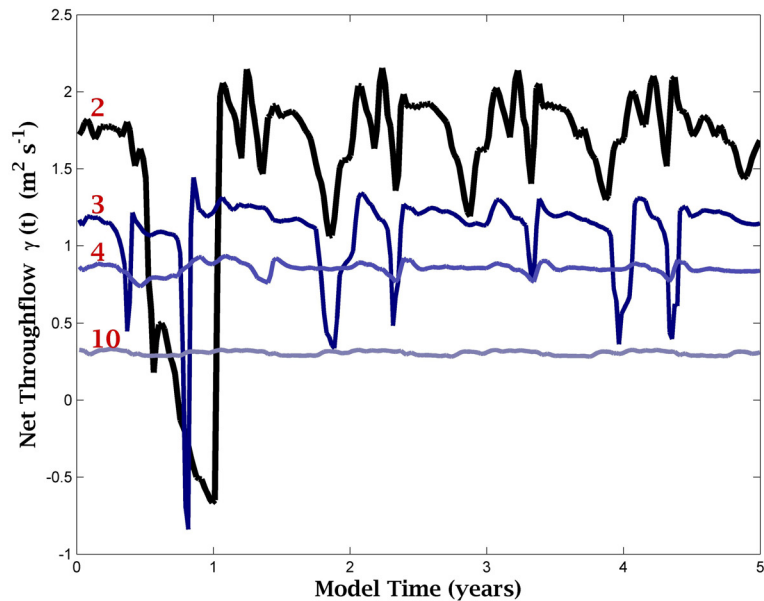


Figure 7.2: Variation in  $\gamma(t)$  over five years of seasonal forcing for different horizontal grid sizes. The prescribed length of  $\Delta Y$  for each run is shown in red in km.

### 7.1.2 Adjusting horizontal grid size

With all other parameters fixed, the standard value for  $\Delta Y$  of 2000 m was close to the resolution limit obtainable. Altering  $\Delta Y$  affected the horizontal resolution and changed the domain configuration by changing the basal slope of the ice shelf and the length of the channel. When  $\Delta Y$  was set to either 1000 m or 1500 m, increasing the horizontal resolution, the model became highly unstable, and introduced errors within one week of model time.

Setting  $\Delta Y$  to 3000 m, 4000 m or 10,000 m (experiments 2, 3 and 4 on the CD) generally had the effect of increasing stability in proportion to the increase in  $\Delta Y$ . The seasonal signal became established earlier in the first year with increasing values of  $\Delta Y$ . This was easily seen in the record of net throughflow,  $\gamma$  (see fig. 7.2), and in salinity and temperature.

For  $\gamma(t)$ , the stability increased with greater  $\Delta Y$  and variability decreased. When  $\Delta Y$  was increased to 10,000 m, an intricate pattern of peaks in  $\gamma(t)$  repeated annually, but the peak-to-peak amplitude of this seasonal variation was only  $\sim 0.04 \text{ m}^2\text{s}^{-1}$ , compared to  $\sim 1 \text{ m}^2\text{s}^{-1}$  for the standard setting. At the same time, the average net throughflow decreased

from  $\sim 1.5 \text{ m}^2\text{s}^{-1}$  for the standard simulation to  $\sim 0.31 \text{ m}^2\text{s}^{-1}$  for  $\Delta Y = 10,000 \text{ m}$ .

The increased stability was also seen in the position of the melt/freeze boundary at the base of the ice shelf. In the simulation where  $\Delta Y = 3000 \text{ m}$ , the location of this boundary ranged between 18 and 30 km from the western end of the channel, but was consistently located at 80 km for  $\Delta Y = 10,000 \text{ m}$ . This was due not only to the more stable domain, but also to the reduced resolution in the horizontal direction.

The cell of anticlockwise circulation was again present for  $\Delta Y$  set to 3000 m, 4000 m, and 10,000 m. For each increase in  $\Delta Y$ , it was stable to a greater distance under the ice shelf, although the size of the increase did not appear to be proportional to the increase in  $\Delta Y$ . This indicated that the primary factor in the length of this cell was the depth of the ice shelf, and to a lesser extent, its basal slope.

Seasonal signals in salinity and temperature were better defined with increased grid size, although they followed a slightly different pattern. With  $\Delta Y$  set to 3000 m, a rapid cooling event occurred within the first year, with the subsequent warming overlain by a very slight seasonal variation. With  $\Delta Y$  set to 4000 m the seasonal signal in salinity propagated throughout the entire domain, while the temperature signal affected only the top 300m of the water column (see fig. 7.3). This demonstrated the greater effect that salinity has on density at these temperatures.

For the simulation with  $\Delta Y$  set to 10,000 m, significantly greater access to the lower half of the domain was allowed, for signals transported in along the base of the ice shelf. This resulted in a very clear seasonal signal in both temperature and salinity, with the varying water masses introduced at the western end (McMurdo Sound) to flow across in the top  $\sim 300 \text{ m}$ , before being swept downwards at  $\sim 160 \text{ km}$  from McMurdo Sound, to fill the lower half of the domain, replaced by new water from the open boundary (see fig. 7.4). With  $\Delta Y$  set to 10,000 m, another interesting seasonal feature was introduced. Once per year, a short-lived event occurred, appearing in the vertical velocity,  $w$ , as stripes of positive and negative values. They functioned as large convection cells, spatially periodic, recurring every 20 km, or every second grid cell.

### 7.1.3 Adjusting the timestep length

The length of the timestep significantly affects the volume of experiments that can be run in the time available. There is a necessary trade-off between the processing speed and the

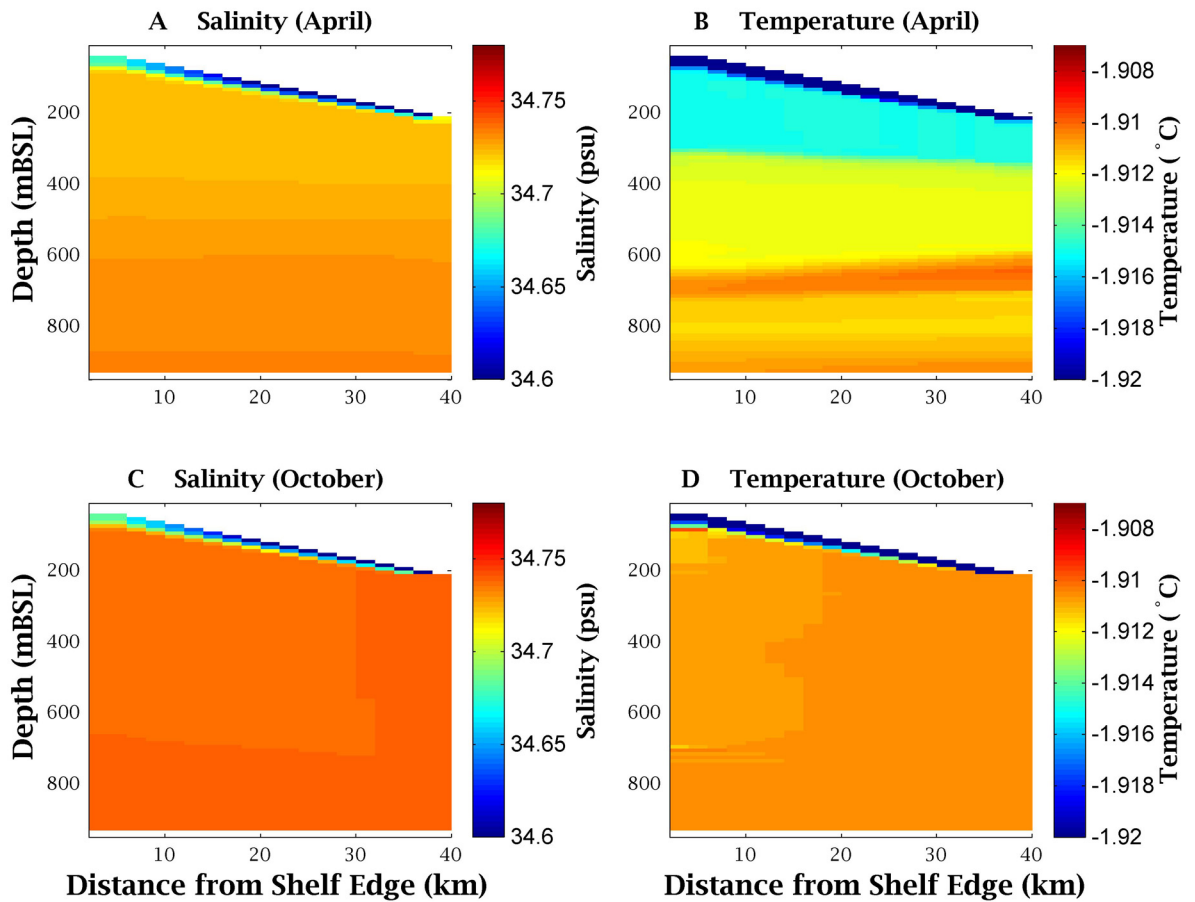


Figure 7.3: Plots of salinity and temperature from the simulation with  $\Delta Y$  set to 4000 m. The layering in temperature (April) resulted from a cool signal being drawn into the domain at the beginning of winter. This clear stratification, missing in salinity, demonstrated the effects of temperature and salinity on density, with vertical gradients in salinity maintained only for a monotonic increase towards the seafloor. Following a further six months of circulation (October), both temperature and salinity were well-mixed throughout the domain. The flow of fresh meltwater up the base of the ice shelf persisted throughout all experiments.

temporal resolution, to ensure that key aspects of the circulation are reproduced. The Courant-Friedrichs-Lewy (CFL) condition (Courant et al., 1928) must also be met - that is, the time step should be sufficiently short that any signal may not be transported a distance of greater than half the cell size, in either the horizontal or vertical directions. A timestep of 30 minutes met this condition, was easily understood in terms of the model output, and allowed up to 8 years of model time to be comfortably run.

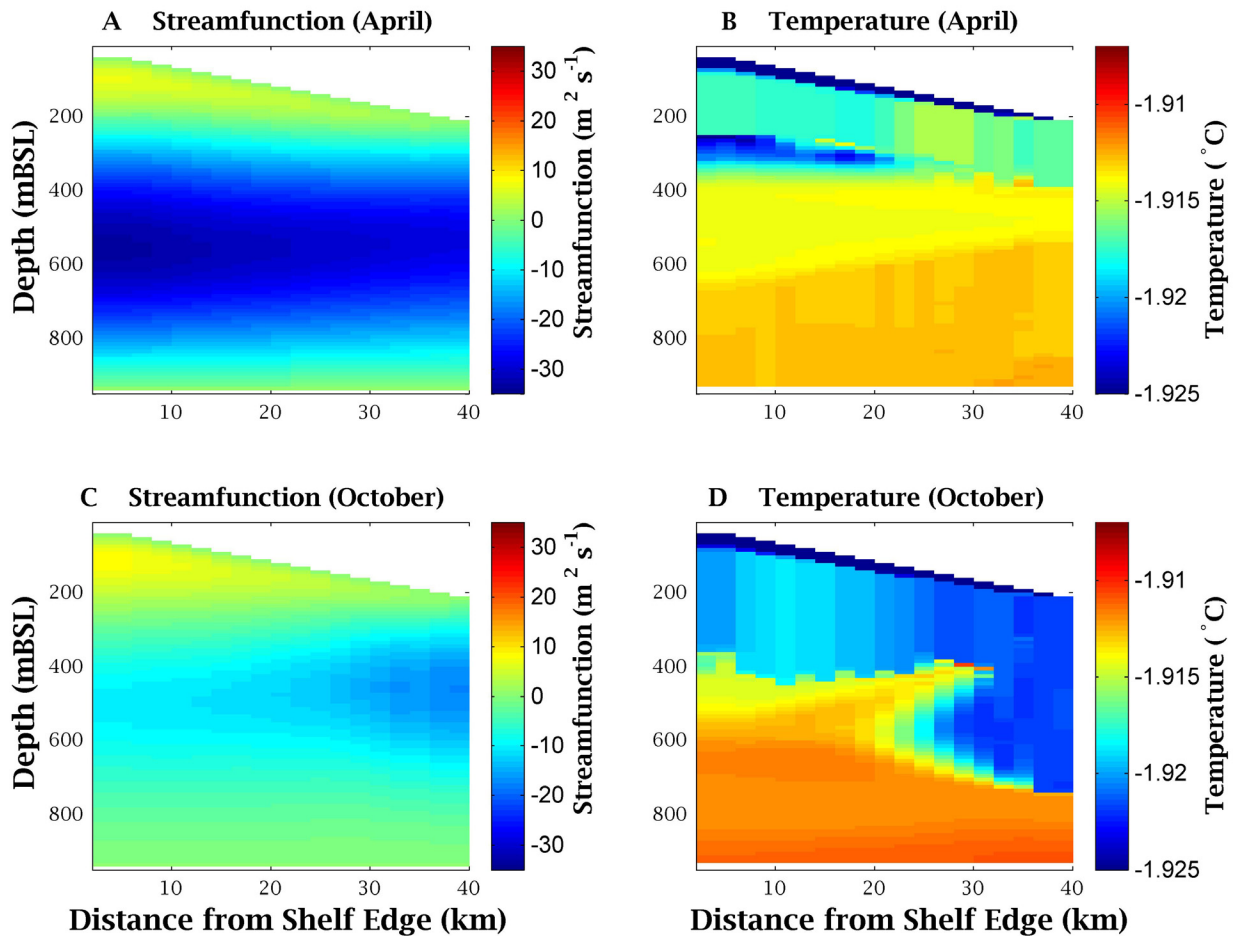


Figure 7.4: Plots of streamfunction and temperature from the simulation with  $\Delta Y$  set to 10,000 m for April and October. For much of the year, the flow structure was similar to that seen here in April. The seasonal signal in temperature was particularly apparent in this simulation. (Animations of this simulation are available on the CD, ‘Experiment 4’, inside the back cover.)

Because the model was unable to sustain a timestep of 1 hour for more than a week of model time, the timestep was adjusted downwards from the standard of 30 minutes, to 5, 10, 15 and 20 minutes. ( $\Delta T$  set to 5 and 15 minutes are experiments 5 and 6 on the CD.) In general the scale of variation was reduced with a smaller timestep, seen particularly in  $\gamma(t)$  (fig. 7.5), for which the peak-to-peak amplitude of variation was only  $0.004 \text{ m}^2 \text{ s}^{-1}$  for  $\Delta T = 5 \text{ min}$ . The average value of  $\gamma(t)$  in the last four years varied in proportion with  $\Delta T$ , and reduced to  $\sim 0.28 \text{ m}^2 \text{ s}^{-1}$  for the smallest timestep, compared with  $\sim 1 \text{ m}^2 \text{ s}^{-1}$  for the standard setting.

The reduced variation was seen in all other variables: the melt/freeze boundary tended to drift less with decreased  $\Delta T$ , but for all  $\Delta T$  adjustments, remained at  $\sim 10$  km from the western end of the domain. The reduced variation in the streamfunction allowed the positive circulation cell below the ice shelf to remain stable for greater distances with reduced values of  $\Delta T$ .

The generally reduced variation is ultimately caused by a weaker signal in temperature and salinity being drawn into the model domain through the open boundary at the west end of the domain. The simulations with  $\Delta T$  of five and ten minutes were so stable that there was virtually no adjustment in the first year - the seasonal signal was evident from  $t_0$  - the beginning of the 5 year, seasonal forcing simulations.

The reason for the reduced variation was that, with shorter  $\Delta T$ , only slight adjustments were required in the parameters for each iteration of the model. This meant that horizontal density gradients, the mechanism by which vorticity was generated in the model, were small, since adjustments were calculated and applied more frequently. Within the constraints of the model, the restoring force at the open boundary was the most realistic means of gaining access to, and increasing horizontal density gradients. Since the restoring force was held constant, vorticity was diminished through this feedback, thereby reducing variation in all of the model's variables.

### **Adjusting timestep and restoring force**

To explore this phenomenon, a further set of tests were run with  $\Delta T$  of 10 mins and successively faster restoring. As expected, all variables exhibited greater variation, with seasonal signals in temperature, salinity and  $\gamma(t)$  of greater amplitude apparent after the first year. The relationship between amplitude of variation and restoring force was not strictly linear, as the variation did not reach the same scale as for original settings, even when the restoring force and timestep were set in similar proportions. The increased variability did not have an affect on the average value of  $\gamma(t)$ , demonstrating that longer-term trends were unaffected by short-term forcing.

For  $\Delta T$  of 30 mins, appropriate for seasonal forcing, restoring at the open boundary at 28 days, produced variation in the model that was stable, but close to the sustainable limit. A timestep of 1 minute, in combination with restoring equivalent to 12 hours was found to result in variations in temperature and salinity similar to hydrological observa-

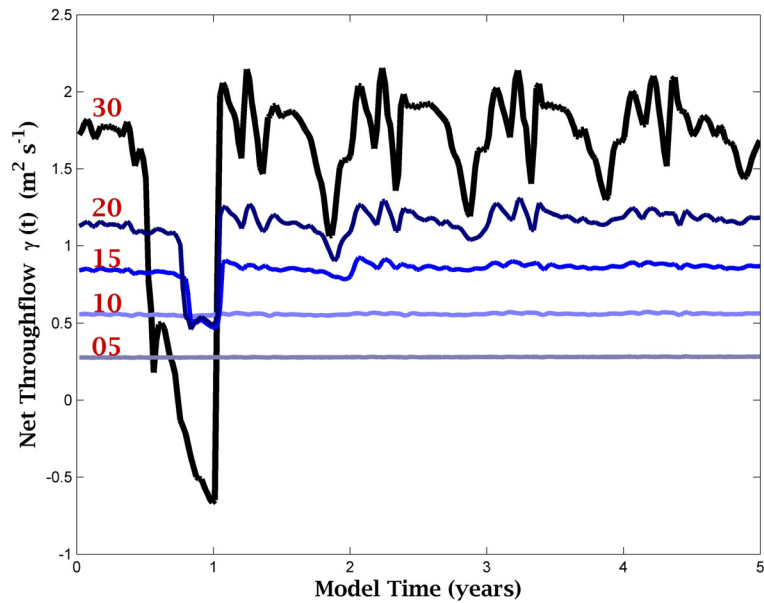


Figure 7.5: Variation in  $\gamma(t)$  over five years of seasonal forcing for different timestep length. The prescribed length of timestep in minutes for each run is shown in red.

tions at the site, and comparable, although on a narrower scale, to the seasonal variation. This demonstrated that, with sufficiently strong forcing, the model was able to adequately recreate aspects of the present thermohaline regime at the site.

#### 7.1.4 Adjusting horizontal diffusion on active tracers

Diffusion in numerical models takes the place of turbulence occurring on scales not resolvable within the model configuration. The stable level of horizontal diffusion on active tracers was higher in this model than in Hellmer and Olbers (1991), so an attempt was made to reduce it to a similar level (experiment 7 on the CD).

Reduced diffusion generally reduced the amplitude of variation in all variables, but it also reduced stability. Set to 50% of the original, seasonal variation took 3 years to set up and was clearly seen in the final two years. Set to 70% however, errors were introduced, causing the model to crash after  $\sim 1$  year of the experiment. A larger reduction, down to 10% of the original allowed the seasonal signal to establish itself within the first year, but the amplitude increased with each succeeding year, until the model crashed after  $\sim 4$  years. These results indicate that the original level of diffusion, having been tuned with the other parameters, was appropriate for the type of forcing and the timestep used.

### Adjusting horizontal diffusion and restoring force

To compensate for the reduced level of diffusion, the strength of forcing at the open boundary was reduced by increasing the restoring time (experiment 8 on the CD). For half the standard rate of diffusion and twice the restoring time compared to standard, the seasonal pattern was found to become stable after one year, and  $\gamma(t)$  averaged about the same value as with standard settings. Seasonal changes in all variables were very slight, so that seasonal variation was able to be seen only on very limited scales. Temperature and salinity scales were reduced to  $\sim 10\%$  of original, and no seasonal drift for the melt/freeze boundary was seen.

#### 7.1.5 Summary

The model was tested by varying the parameters that affect the dynamics, which were originally set to produce the greatest variation sustainable within the model. As a result, the standard values of the various interrelated parameters created behaviour in the model more desirable than was achieved by altering any one value. For this reason, in the subsequent five year seasonal forcing experiments, parameters have been left at their standard values.

In all experiments, a cell of anticlockwise circulation existed at the base of the ice shelf throughout the model year. This cell was caused by, and in turn, maintained, the continual transport of fresh meltwater up the sloped base of the ice shelf. Increased stability was produced through smaller timesteps ( $\Delta T$ ), which resulted in smaller horizontal density gradients and less seasonal variation in tracers, or by increasing the cell size at the expense of spatial resolution. No limit was found for increasing the size of  $\Delta Y$ .

The attempts to reduce the level of horizontal diffusion, making the circulation more dependent on advection and convection, also had the effect of reducing stability, although not in a predictable manner: Reduction to 50% of the standard value was viable, while reduction to either 10% or 70% was not. Since the stability was unpredictably related to the level of diffusion, the standard level was maintained. The value of  $1 \times 10^2 \text{ m}^2 \text{ s}^{-1}$  applied is at the lower end of values observed in the ocean, which range from  $1 \times 10^2 \text{ m}^2 \text{ s}^{-1}$  to  $1 \times 10^5 \text{ m}^2 \text{ s}^{-1}$  (Apel, 1987). The value of  $1 \times 10^{-4}$  taken from Hellmer and Olbers (1989, 1991) for vertical diffusion of tracers, is likewise within the observed range of  $3 \times 10^{-5}$  to  $2 \times 10^{-2} \text{ m}^2 \text{ s}^{-1}$  (Apel, 1987).

The location of the melt/freeze boundary was found to be quite sensitive to the model dynamics as these were altered with succeeding parameter changes. When the resulting seasonal variation was high, the position of the melt/freeze boundary shifted in relation to the seasonal variation, located deeper under the ice shelf in winter and shallower during summer. When resulting seasonal variation was low, the melt/freeze boundary appeared to remain in place. While the location shifted more with increased seasonal variability, the average position was unaffected.

With the standard settings, the model was found to have long-term stability. Following the initial adjustment to the seasonal forcing of salinity and temperature in the first year, the seasonal pattern in all variables was highly evident. A clear annual pattern was established in the net throughflow, during the second year, and was faithfully reproduced in each subsequent year.

## 7.2 Sensitivity analysis - sedimentation environment

The second set of tests investigated the various aspects of sediment transport and deposition in the model. Parameters were adjusted, with the aim of tuning towards the current sediment transport environment as observed at the field sites (Barrett et al., 2004).

Sediment was incorporated into the model as an additional tracer, treated as a mass concentration per unit volume. Sediment was treated in the same way as for salinity and temperature except that no account was made of any density differences that may have arisen as a result of the suspended material. This assumption was valid because of the low concentrations of sediment used, so that the model dynamics were completely unaffected by the addition of this passive tracer. The settling velocity, indicative of grain size, was applied each timestep by shifting calculated concentrations down through the water column at an appropriate rate.

Sediment deposition could not be accurately modelled due to insufficient resolution in the vertical direction. Instead, sediment entering the cell immediately above the seafloor was ‘captured’ and ‘collected’, then removed from the model domain. This operation is analogous to a moored sediment trap. An accumulation rate was derived from the rate of sediment ‘capture’, using the relationship established with previous experimental work (see section 5.3).

Initially, the only source of sediment in the sub-ice cavity was from the open water in McMurdo Sound. Later an additional source was introduced, representing flux from the melting ice shelf. The concentration of sediment released was determined by the rate of melting at the ice shelf base using the relationship:

$$\text{Sediment released} = \dot{h} \Delta A \Delta T \lambda_{IS}, \quad (7.1)$$

where  $\dot{h}$  is the basal melt rate,  $\Delta A$  is the basal area over which  $\dot{h}$  applies, and  $\Delta T$  is the timestep. The concentration of sediment within the ice shelf,  $\lambda_{IS}$ , was assumed to be continuous and constant. It was adjusted so that this source produced  $\sim 5\%$  of the mass of sediment deposited at the seafloor, the upper limit of sediment potentially derived from the ice shelf surface, observed at the Windless Bight sites (Barrett et al., 2004).

### 7.2.1 Standard settings

Four distinct sediment types were included in the model. Each was characterised by concentration in the water column, and a settling velocity corresponding to grain size. Grain sizes of  $3\phi$  ( $\equiv \frac{1}{8}$  mm) and  $8\phi$  ( $\equiv \frac{1}{256}$  mm) were used, with two different treatments for each in all of the scenarios. With the expectation that results could be scaled to better represent the real situation, initial tests (*'Standard Experiment'* on the CD) were run with standard settings applied to all types (see table 7.2).

Settling velocities were set at  $1 \times 10^{-3}$  m s $^{-1}$  and  $7 \times 10^{-6}$  m s $^{-1}$  for the  $3\phi$  and  $8\phi$  grain

Table 7.2: Initial values prescribed for testing of sediment transport and deposition within the model

Initial value	Zero everywhere
Profile at open boundary	$1 \times 10^{-3}$ g m $^{-3}$ to 300m
Amplitude of oscillation at open boundary	$1 \times 10^{-3}$ g m $^{-3}$
Level of horizontal diffusion	$1 \times 10^2$ m $^2$ s $^{-1}$
Level of vertical diffusion	$1 \times 10^{-4}$ m $^2$ s $^{-1}$
$\Delta Y$	2 km

sizes respectively, following Gibbs et al. (1971) for water at 0°C and 34‰. Of the water characteristics trialled by Gibbs et al. (1971), these were closest to those found in the model.

Sediment was supplied seasonally via a sinusoidal signal to the top 300 m at the open boundary at McMurdo Sound. The amplitude of the variation was equivalent to the average profile (see table 7.2), applied so that the maximum concentration coincided with the warmest temperatures, or summer conditions. Both types were drawn into the model domain in 3 pulses per annum, taking up the first ~6 months. This behaviour corresponded to the independent behaviour of the model dynamics. The domain was largely emptied of sediment each year over the winter season, consequently, a clear seasonal cycle was observed in the deposition of both sediment types.

The experiments began with the domain empty of sediment, so that while the model responded to the boundary forcing, relatively low levels of deposition were seen. After the first year, the average annual accumulation remained consistent throughout the remaining four years of the model run.

Being much finer, and having a sufficiently low settling velocity, the  $8\phi$  sediment was carried along with the general circulation and flowed into the domain in a band immediately below the ice shelf (see fig. 7.6). Interactions with vertical boundaries produced anomalous deposition peaks in the cells immediately adjacent to the boundaries (see fig. 7.7). In addition, a peak in deposition was seen towards the eastern end of the domain. This was due to the drawing down of material in a persistent convection cell located at the end of the base of the ice shelf. A clear seasonal signal in deposition rate was seen at both ends of the ice shelf, with the central regions receiving relatively little accumulation throughout the year.

The settling velocity of the  $3\phi$  grains had a greater affect on their behaviour than the circulation. This is clearly seen in the smooth drop-off in accumulation rate with increasing distance from the open water at McMurdo Sound (see fig. 7.7). Again, a slight peak in deposition due to interaction with the open boundary was identified, but only at the McMurdo Sound end of the domain. Although the sediment was supplied to only the top 300 metres below sea level (m BSL) of the model domain, peak concentrations were observed at depths ~400 to 500 m BSL (see fig. 7.6), demonstrating the effect of the

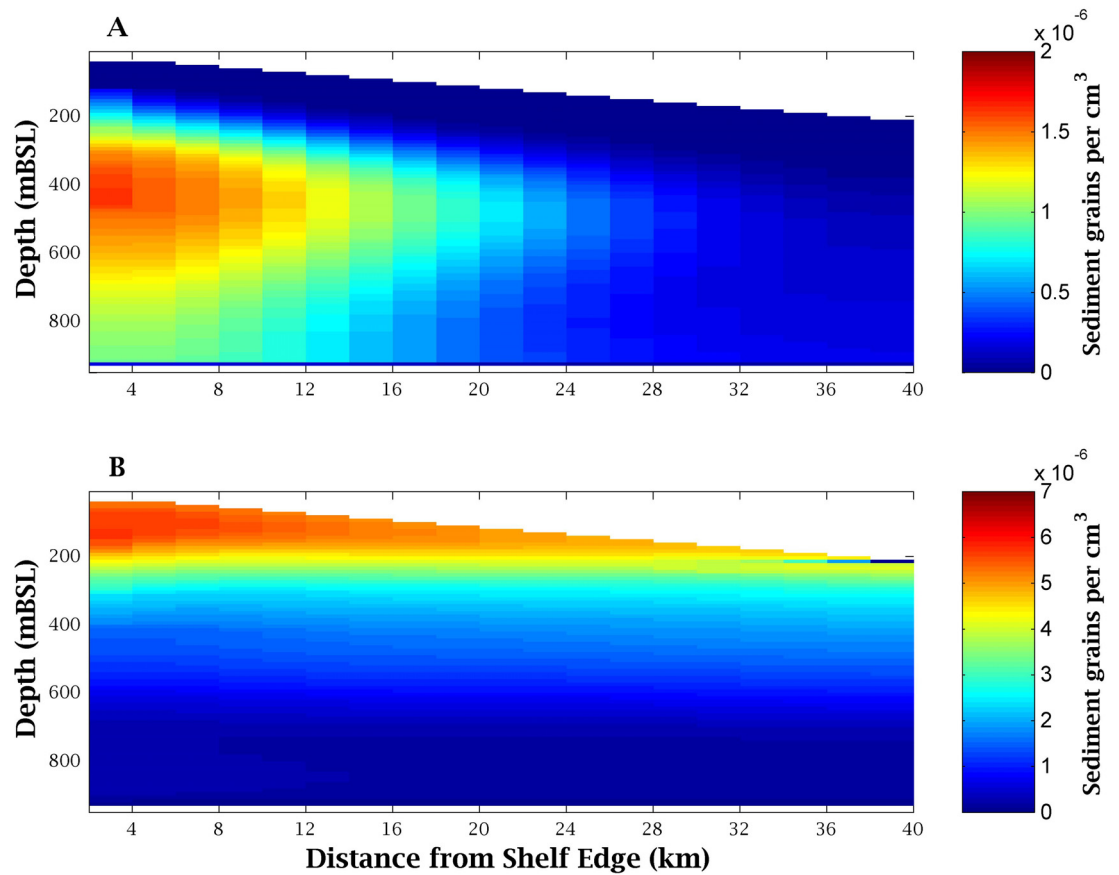


Figure 7.6: Concentrations of (A) fine sand ( $3\phi$ ) and (B) fine mud ( $8\phi$ ) material in the water column after initial spin-up of the standard experiment. Each is sourced from McMurdo Sound, outside the western boundary, and supplied to the top 300 m of the water column. The locations of peak concentrations for each demonstrate their different responses, determined by their settling velocity, to the circulation within the domain interior.

higher settling velocity.

### 7.2.2 Adjusting initial conditions

To test how quickly sediment concentrations within the domain stabilised, positive anomalies were imposed on the environment at the start of the experiments. These were found to result in a proportional increase in sediment deposition within the first year. The deposition pattern was affected by the grain size: for the larger,  $3\phi$  grains, highest deposition occurred immediately below the initial anomaly. The smaller,  $8\phi$  grains were suspended in the water column and carried, so that the deposition of the initial anomaly was spread

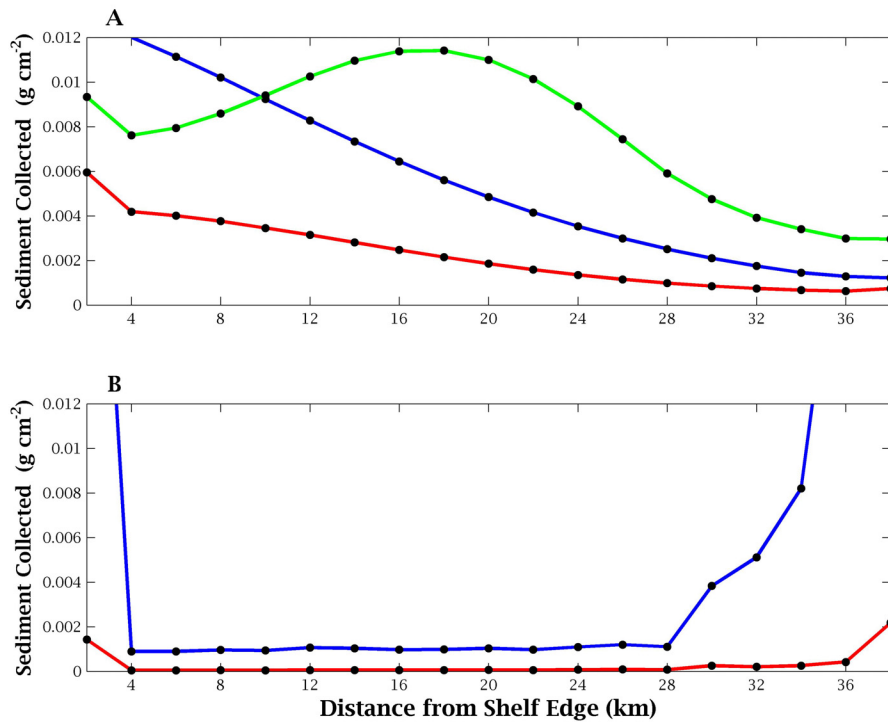


Figure 7.7: Total accumulation of (A) sand ( $3\phi$ ) and (B) fine mud ( $8\phi$ ) material after five years of model simulation. Each is sourced from McMurdo Sound (west of shelf edge), supplied to the top 300 m of the water column. The red line shows the deposition in the standard experiment, green is from the experiment with a large initial anomaly, and blue is from the experiment with sediment supplied throughout the depth of water column. In panel (B), green and red lines lie in the same place.

over the seafloor of the entire domain (see fig. 7.7).

In separate experiments, the accumulation was reset to zero after one and two years of spin-up time, with the aim of capturing seasonal variation in the deposition pattern. Similar results were seen for resetting after one and two years, indicating that a single year was sufficient to allow sediment concentrations to stabilise.

Initial anomalies were absorbed by the model circulation within the first year - no trace of the higher concentration was apparent after about four months. These two effects were both taken to imply that whatever initial conditions were imposed, sediment concentrations within the model domain were stable after one year. In subsequent experiments the first two years were used to allow the sediment concentration within the domain to

stabilise, after which time the sediment traps were ‘opened’ by resetting the sediment accumulation to zero.

### 7.2.3 Adjustments to the open boundary source

The standard sediment profiles for McMurdo Sound supplied sediment to only the top 300 m of the water column, the approximate depth to which primary open water productivity occurs in the Ross Sea. In an attempt to replicate the high sediment fluxes near the seafloor reported by Dunbar et al. (1998) and Langone et al. (2003), the open water source of sediment was extended to cover the whole water column (experiment 9 on the CD). The sediment was able to enter the sub-ice shelf cavity only when it was drawn in by the model’s general circulation pattern. By this means entrainment of sediment into the upper section of the water column occurred over three quarters of each year, corresponding to between early-summer and the end of winter.

Entrainment into the lower section of the model domain occurred in the fourth quarter (spring), as dictated by the seasonal changes in flow direction. In general, even though the original seasonality of the sediment source was maintained, the effect of the seasonal circulation led to the deposition patterns of both  $3\phi$  and  $8\phi$  sediment types losing seasonality, as sediment was drawn into the domain and subsequently deposited throughout the year (see fig. 7.8).

With a source near the seafloor and the higher settling velocity of the  $3\phi$  grains, little time was available for the transport of these grains to deep within the cavity, so that accumulation within the domain was faster near the open boundary. In contrast, the settling velocity representing the  $8\phi$  grains was sufficiently low as to allow entrainment into the water column. In the main, these grains were deposited only after having traversed the width of the model domain and then entering the region of down-welling at the deep end of the ice shelf.

When only a shallow benthic layer of sediment was made available via the open boundary profiles, a substantial contribution to the deposition from this source was seen. The material could only be transported into the domain with inflowing velocities, so this indicated that, at periods throughout the year, intense benthic flows were experienced.

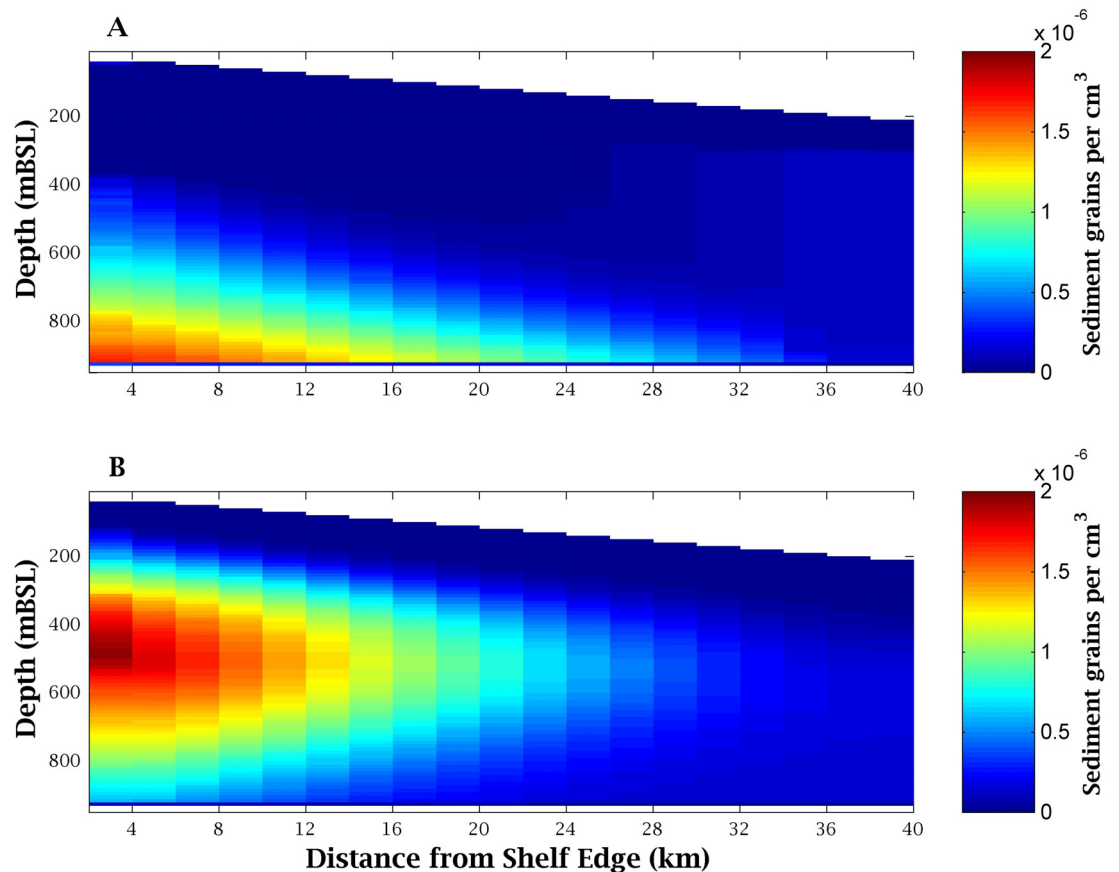


Figure 7.8: Fine mud ( $8\phi$ ) concentrations for different times of the year from the simulation in which additional sediment was supplied near the seafloor. (A) represents the pulsing seen in three quarters of the year (summer through winter), while (B) represents the 4<sup>th</sup> quarter (spring). Sediment was drawn into the domain near the seafloor during the period in which none was drawn into the upper levels. This explains the loss of seasonality in the annual sediment deposition.

#### 7.2.4 Scale of model domain - changing $\Delta Y$

The effect of lengthening the horizontal scale of the model domain on sediment transport and deposition was investigated using  $\Delta Y = 3000$  m, 4000 m or 10,000 m (experiments 2, 3 and 4 on the CD). Extending the length without adjusting other parameters had the effect of changing the shape of the domain, particularly with the shallower basal slope of the ice shelf (see section 7.1.2 for changes in the general circulation). The two different grain sizes were found to respond quite differently to this change.

For the larger,  $3\phi$  grains, little change from the standard experiment was seen, as the

grains dropped out of the water column quickly, and were therefore relatively unaffected by the modified circulation. The deposition gradient, away from McMurdo Sound, was enhanced by increasing the supply of sediment near the seafloor. The proximity to the seafloor provided even less time for sediment to be transported further into the domain.

In these experiments, the fine-grained sediment functioned as a passive tracer, and behaved in the same manner as temperature for the same set of experiments (see section 7.1.2). When  $\Delta Y$  was extended to 10,000 m significant access to the lower portion of the water column was achieved, with an apparent clockwise flow of sediment. It entered in the top left and cleared the domain by exiting at bottom left (see fig. 7.9). The deposition pattern was strongly affected, with a more even spread across the entire width of the domain. The region of greatest deposition remained towards the deep end of the ice shelf, maintained there by a region of down-welling.

### 7.2.5 Grain size - settling velocity

In the standard experiments grain sizes of  $3\phi$  and  $8\phi$  were used. These were the two sizes most commonly found in the surface sediments recovered from Windless Bight. These were not representative of all of the sediment recovered from there, so other settling velocities were trialled to test behaviour of intermediate grain sizes (see experiments 10, 11 and 12 on the CD). The settling velocity was successively decreased from  $1 \times 10^{-3} \text{ m s}^{-1}$ , to represent grain sizes decreasing from  $15 \mu\text{m}$  (Gibbs et al., 1971). Two distinct settling regimes were identified, with the change occurring at  $\sim 1 \times 10^{-4} \text{ m s}^{-1}$ , equivalent to  $\sim 5 \mu\text{m}$ , which lies between  $7$  and  $8\phi$ .

Settling velocities faster than  $1 \times 10^{-4} \text{ m s}^{-1}$  resulted in higher deposition at the open water end of the domain, with a smooth drop-off towards the far end. Seasonality was apparent in the deposition cycle, and significant deposition was observed within the first year.

Settling velocities slower than  $1 \times 10^{-4} \text{ m s}^{-1}$  allowed the sediment to become entrained in the water column, so that a very different pattern was observed. Deposition was concentrated at either end of the domain and was associated with the region of down-welling at the far end. Seasonality of sediment concentration decreased with prescribed settling velocity, and less and less deposition occurred within the first year. A lower limit of  $1 \times 10^{-6} \text{ m s}^{-1}$  ( $\cong 2 \mu\text{m}$ ) was found, below which the differences in circulation or deposition of

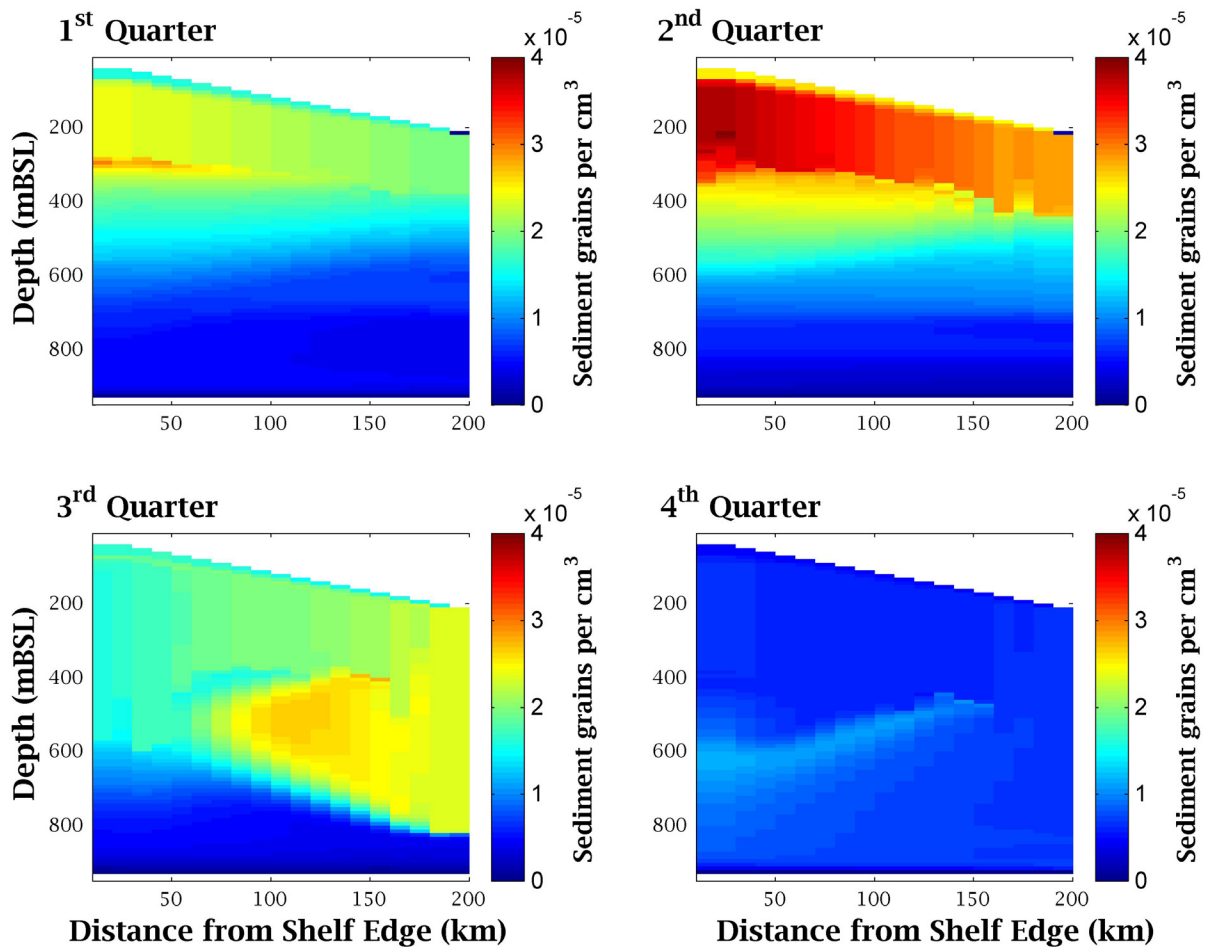


Figure 7.9: Concentrations of fine mud ( $8\phi$ ) for four quarters of one year with  $\Delta Y = 10,000$  m, showing the seasonal clockwise progression. Sediment was drawn into the domain near the base of the ice shelf during spring and summer (1<sup>st</sup> and 2<sup>nd</sup> Quarters). It then was drawn down near the deep end of the ice shelf during autumn (3<sup>rd</sup> Quarter) to exit bottom left in winter (4<sup>th</sup> Quarter). (Animations of this simulation are available on the CD (as ‘Experiment 4’), inside the back cover.)

sediment were indistinguishable between successively smaller sediment types.

### 7.2.6 Summary and final tests

These experiments were run to test behaviour of the various aspects of sedimentation within the model. Results from these tests were used to tune the behaviour in subsequent seasonal experiments towards the key features observed at Windless Bight and in McMurdo Sound (see section 5.3).

The sedimentation environment was found to be highly sensitive to settling velocity. Two significantly different regimes were identified, with the change occurring for a settling velocity  $\sim 1 \times 10^{-4} \text{ m s}^{-1}$ . This corresponded to a grain size of  $\sim 5 \text{ }\mu\text{m}$  (Gibbs et al., 1971), or between  $7\phi$  and  $8\phi$ .

For the standard experiment, the depositional pattern was found to be seasonal for both  $3\phi$  (large) and  $8\phi$  (small) grain sizes, with the annual cycle marked by a decrease in deposition over the winter months. This seasonality was progressively lost as the grain size was reduced, because the smaller grains stayed in suspension longer, and were available for deposition throughout the year.

Supplying sediment near the seafloor at the open boundary also reduced the seasonality in the sediment deposition. This was mostly due to the seasonal cyclicality of the flow direction, with intense inflows able to transport high concentrations of sediment into the domain. The intense inflows at the seafloor during winter compensated for the simultaneous reduction in inflow higher in the water column. By this process, intense inflows occurred throughout the year, although with changes in depth, so that sediment was present within the model domain, and could be deposited, throughout the year.

### 7.3 Seafloor configuration experiments

Seasonal forcing experiments were carried out to investigate the response of the model dynamics and sedimentation environment to four different seafloor configurations. With each configuration, the standard slope of the ice shelf was maintained, but combined with stylised bathymetry. The four domain configurations were as shown in figure 7.10. The experiments ran for seven years of model time, each made up of twelve, 30-day months.

The standard method of creating seasonal variation within a model of this type is to vary boundary profiles of temperature and salinity by applying an annual sinusoidal signal to each. Year-long observations from McMurdo Sound (Littlepage, 1965) revealed seasonal variation in both temperature and salinity which did not fit this assumption. The general pattern was high variation during summer months, restricted to the top of the water column (to  $\sim 400\text{m}$ ), and flat response over the 5 - 6 months of the winter season.

From the year-long set of observations, temperature and salinity profiles were created

representing monthly average profiles to be used to force the model at the open boundary. The temporal variation was then reduced, imitating the observed dampening of signals with distance from the open water (see chapter 3). To avoid uneven transitions between average monthly profiles, smoothing between successive profiles was achieved using proportional application of each.

### 7.3.1 General features of circulation

Several features of the circulation were seen in all of the experiments, and were largely the same as those for the standard experiment in section 7.1. These were typically associated with the basal slope of the ice shelf and the interactions at the ice-water interface.

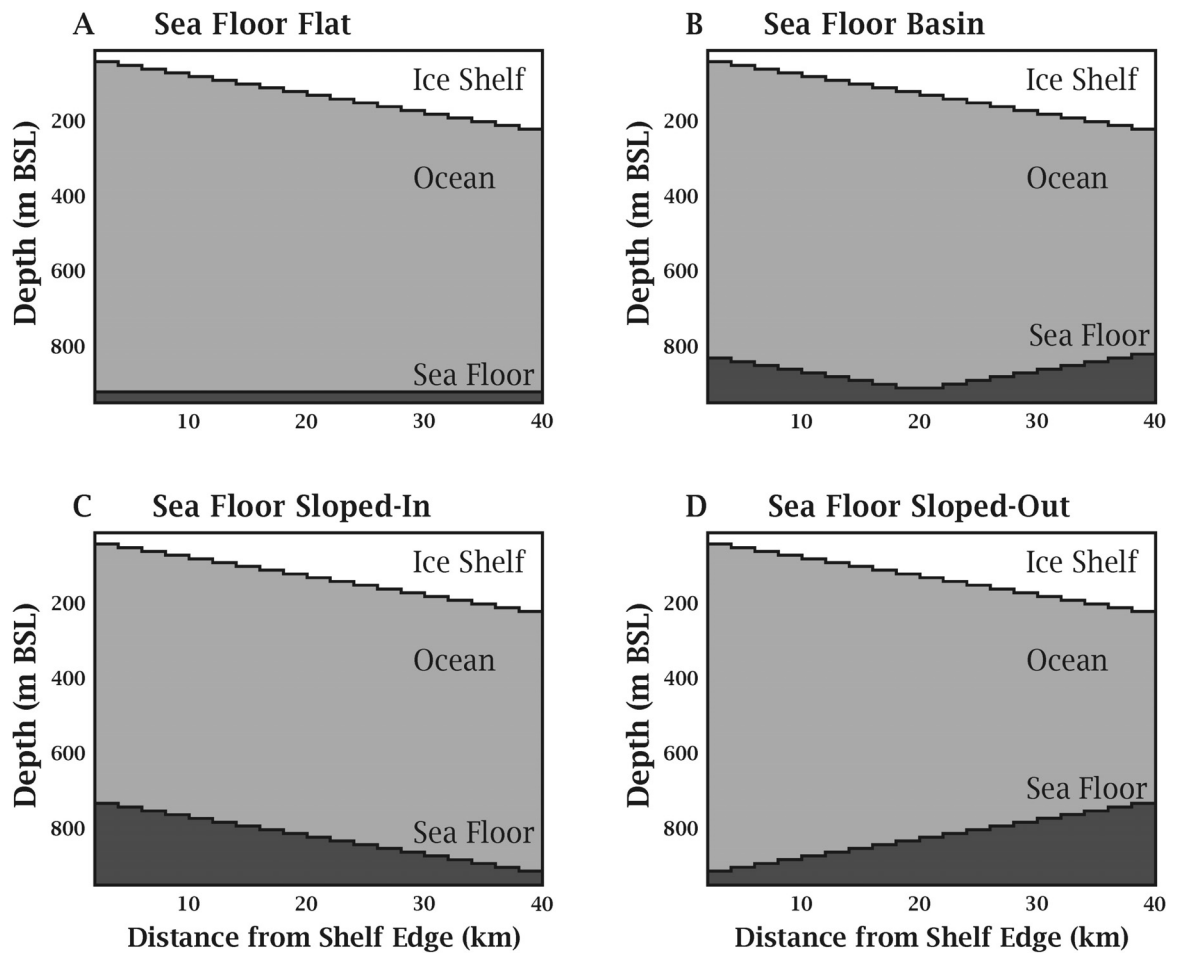


Figure 7.10: The four domain configurations used for seasonal forcing experiments. Seafloor and ice shelf slopes are 1:200, using a 1:1 ratio of  $\Delta Y:\Delta Z$ . Short names for these configurations used in the text are (A) SF-Flat, (B) SF-Basin, (C) SF-Sloped-In and (D) SF-Sloped-Out.

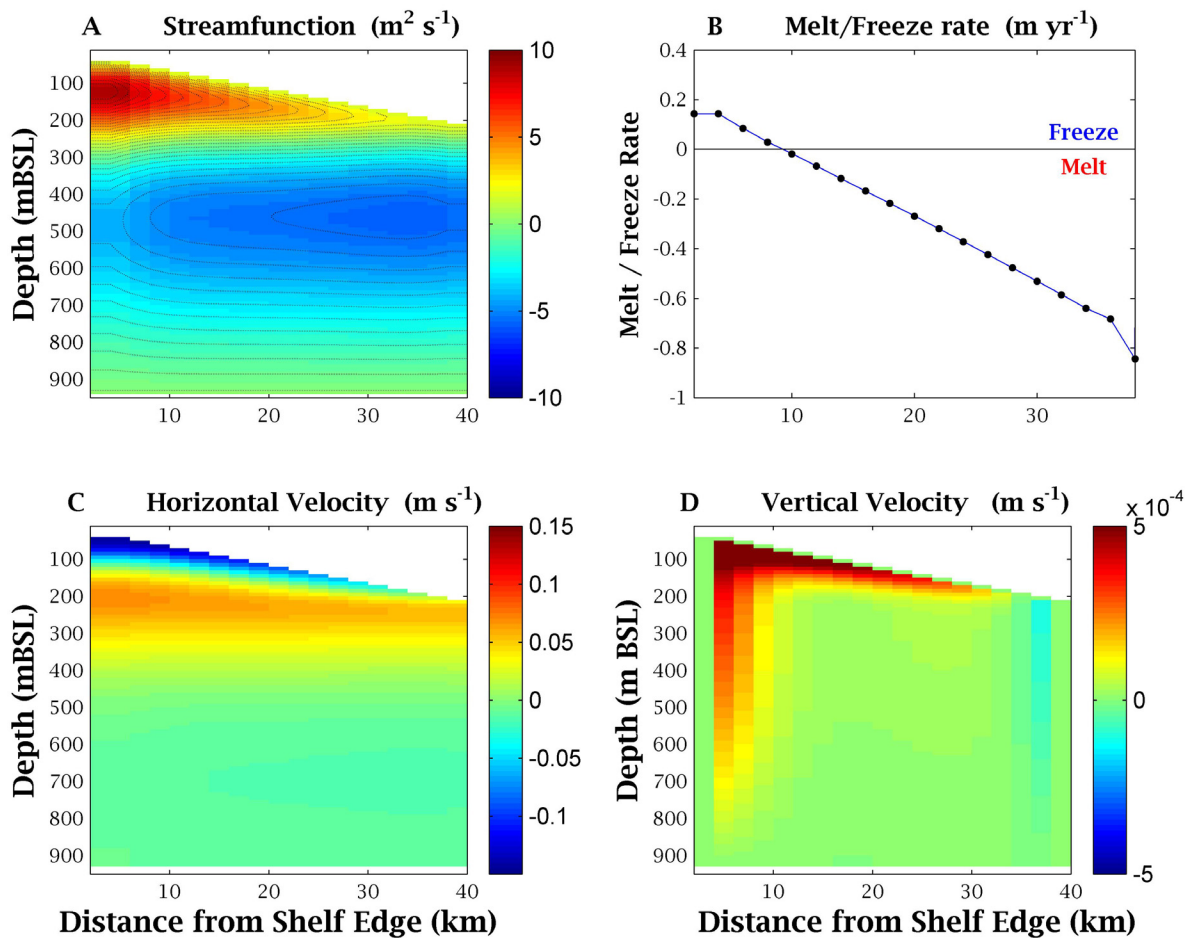


Figure 7.11: Plots of (A) streamfunction, (B) melt rate, (C) horizontal velocity and (D) vertical velocity after four weeks of the seasonal forcing model run with standard settings. The sloping ice shelf and flat seafloor are shown in white. The red circulation cell in the streamfunction at the base of the ice shelf represents anticlockwise flow, initiated by the continual flow of fresh meltwater up the base of the ice shelf.

Continual melting equivalent to  $\sim 0.6 \text{ m yr}^{-1}$  at the deep end of the ice shelf produced a steady supply of cool, fresh water which flowed up the base of the ice shelf. This caused, and was in turn maintained by, a cell of anticlockwise circulation attached to the ice shelf base (e.g., see fig. 7.11).

This cell resulted in a shallow zone of westward flow immediately adjacent to the ice shelf, underlain by a zone of eastwards flow. In most simulations, a second shear zone at  $\sim 500 \text{ m}$  marked the entrance into another zone of westwards flow, which produced flow to approximately offset the eastwards flow above it.

Changes in the streamfunction structure usually affected the entire water column simultaneously, and were therefore recorded in the time-series output of  $\gamma$ . For this reason, the evolution of  $\gamma$  over time clearly revealed whether or not the changes in streamfunction structure were seasonal.

The introduction of shape to the seafloor affected the circulation more than the seasonal forcing. The sloped seafloor of SF-Sloped-Out and SF-Sloped-In, dominated the overall flow by promoting the continual flow of the densest waters down the benthic slope. The underlying seasonal variation became lost, as it was completely overwhelmed by the flow parallel to the seafloor. The SF-Flat configuration, without the seafloor slope to dominate the thermohaline circulation pattern, was highly sensitive to the seasonal forcing.

The basin structure affected circulation in a different way, which appeared most likely to be an artificial feature due to the details of the model formulation. With the change in seafloor gradient from negative to positive in the middle of the domain, the calculations resulted in a shift in  $\phi$ , the throughflow part of the total streamfunction (see fig. 7.12).  $\phi$  was the vertical distribution of  $\gamma$  through the water column, with equal assignment to each spatial increment  $\Delta Z$  (see Appendix A). Where the slope of the seafloor changed, a horizontal shift in  $\phi$  resulted. This may have fed back into  $\theta$ , the circulating part of the streamfunction, as it adjusted to compensate.

The shift in streamfunction values near the middle of the domain produced a region of down-welling there, through the relationship  $w = -\Psi_y$ . As newly-formed meltwater was being continually drawn away from the ice shelf by this feature, a significant division at this point was seen in the usually smooth gradients of temperature and salinity at the base of the ice shelf.

### **Response of different seafloor configurations to seasonal forcing**

With annual forcing by monthly profiles, seasonality was apparent in all variables and, to different degrees, for all domain configurations (see fig. 7.10).

For the SF-Basin configuration (experiment 13 on the CD), the seafloor shape caused a horizontal shift in the streamfunction (see fig. 7.12), which in turn caused a division in the gradients of temperature and salinity at the base of the ice shelf (as described in

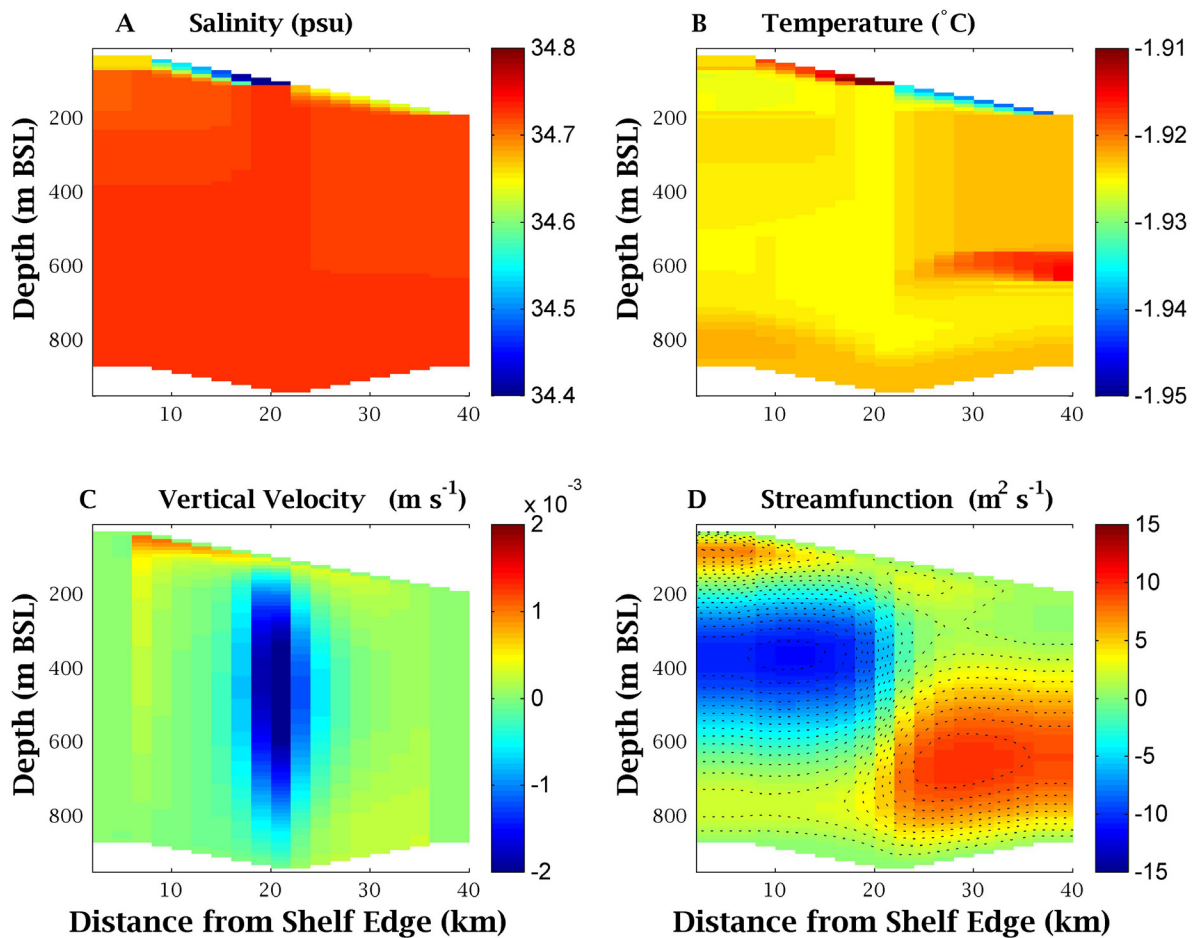


Figure 7.12: (A) Salinity, (B) Temperature, (C) Vertical Velocity and (D) Streamfunction after 20 weeks of seasonal forcing with ‘SF-Basin’ configuration. This shows the shift in streamfunction caused by the change in seafloor gradient, and the resulting region of down-welling over the central basin. This continual downwards flow drew fresh melt water away from the ice shelf in the centre of the domain, causing a division in the gradients of temperature and salinity at the ice-ocean interface. The warm feature to the right of the domain at 600 m BSL was probably an artefact of the model formulation, as it was seen only with this domain configuration.

7.3.1). This feature dominated the circulation, so that the effects of the seasonal forcing were apparent but slight.

With the SF-Sloped-In configuration (experiment 14 on the CD), the shape of the streamfunction followed the contour of the seafloor shape, and so retained the same structure throughout the experiment. This fed back into the other variables so that, although an-

nual variation could be seen, basic structure was stable throughout.

For the SF-Sloped-Out configuration (experiment 15 on the CD), seasonality was apparent in all variables except for temperature. The most significant feature of the temperature was the continual flow of relatively warm water down the benthic slope, drawn down in the region of down-welling at the eastern end of the domain. The structure of the streamfunction was again primarily determined by the seafloor shape, with the stability in structure being fed back into all other variables.

Without seafloor slope to dominate circulation, the SF-Flat configuration was particularly responsive to seasonal forcing. Seasonality was established in all variables within the first year, and was maintained for the remaining six years of model time (e.g., see fig. 7.1).

### 7.3.2 Sedimentation environment

For these seasonal forcing experiments, four sediment types were incorporated, defined by their settling velocity and source. From the open water of McMurdo Sound, three types were sourced, representing pellets (compacted biogenic debris, mainly broken diatoms), algal flocs (loosely bound biogenic debris) and terrigenous fine mud. Open water source concentrations were scaled so that in SF-Flat simulations, 55%, 30% and 15% of the mass delivered to the seafloor close to McMurdo Sound was in the form of pellets, algal flocs and fine mud, respectively. This ratio was determined to be in approximate agreement with observations from McMurdo Sound (Dunbar et al., 1998).

The possibility of another type of sediment - terrigenous fine sand - sourced from basal melting of the shelf ice, was also investigated. This sediment type was added because the mineralogy of the sand from the Hot Water Drill (HWD) sites suggests such an origin (Barrett et al., 2004). In these experiments, the flux of sediment into the water column was determined by the concentration in the modelled ice shelf, which was adjusted to provide sediment accumulation at the seafloor equivalent to 5% of the open water source accumulation. The rate of sediment released at points along the transect was determined by the local basal melt rate.

In the cores recovered from HWD-1, approximately 30 cm of sediment had accumulated in  $\sim 20,000$  years. The source concentrations in the model were again scaled so that the

mass delivered to the seafloor from the open water source corresponded to the observed accumulation rate at HWD-1. This was achieved using the relationship of Dunbar and Leventer (1987) that a flux of  $1000 \text{ mg m}^{-2} \text{ d}^{-1}$  in deep water equates to  $\sim 4 \text{ mm}$  accumulation per year.

For all experiments and all sediment types, two years of model time were allocated at the beginning to allow the concentrations of material within the domain to stabilise. At this point, deposition experiments were effectively begun by resetting the accumulation to zero. After this, seasonal experiments were run for a further five years of model time.

### General patterns of sedimentation

The main factor affecting the seasonality of deposition patterns was the settling velocity. The pellets (high settling velocity) were forced to drop out of the water column quickly, and therefore deposition occurred for only a short time after their introduction at the western end. In contrast, fine mud (low settling velocity), was maintained in suspension for much longer, so that deposition occurred throughout the year. Figure 7.13 shows the accumulation patterns of the pellets, algal flocs and mud for the flat seafloor configuration.

The effect of the model dynamics on depositional patterns was most easily seen for the ‘SF-Basin’ configuration. The fine mud was most susceptible to the circulation patterns of the model dynamics. As a region of down-welling was consistently located over the central basin (see subfigure 7.12c), exceptionally high accumulation rates of fine mud were seen there (see fig. 7.14). The sand was also preferentially deposited within the basin. A significant drop in the accumulation rate of algal flocs was seen within the basin. This material was assigned a settling velocity which allowed it to avoid both of the previous effects, so it flowed across the rim of the basin and was preferentially deposited elsewhere (fig. 7.14).

### Pellets sourced from McMurdo Sound

The pellets, considered to be around  $300 \mu\text{m}$  in diameter, were defined by a settling velocity of  $1.7 \times 10^{-3} \text{ m s}^{-1}$  and constant source concentration at McMurdo Sound, of  $25 \text{ g m}^{-3}$ . This material was supplied to only the upper 300 m at the western boundary (see section 5.3 for details). Seasonality was not applied to the boundary profile, as it was not required to produce seasonal variation in this type.

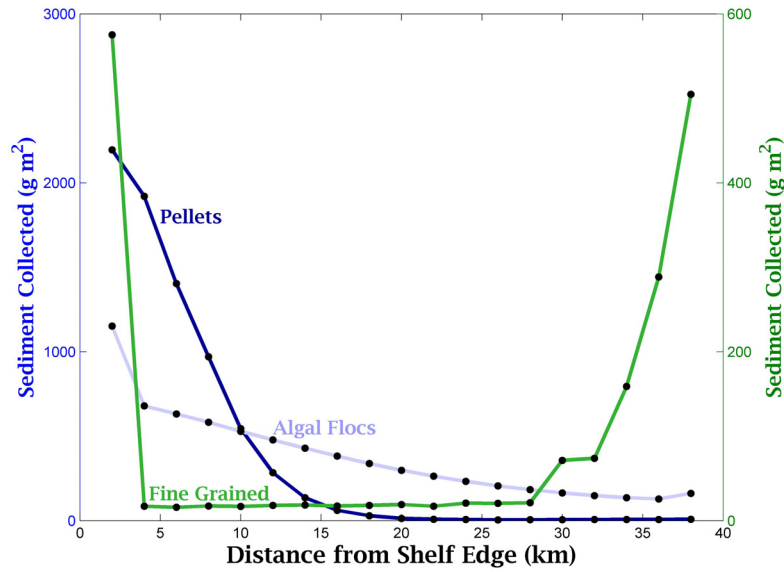


Figure 7.13: Patterns of deposition after five years of seasonal forcing with SF-Flat configuration. Blue (pellets and algal flocs) are read with the scale to the left, and green (fine mud) is read with the scale to the right.

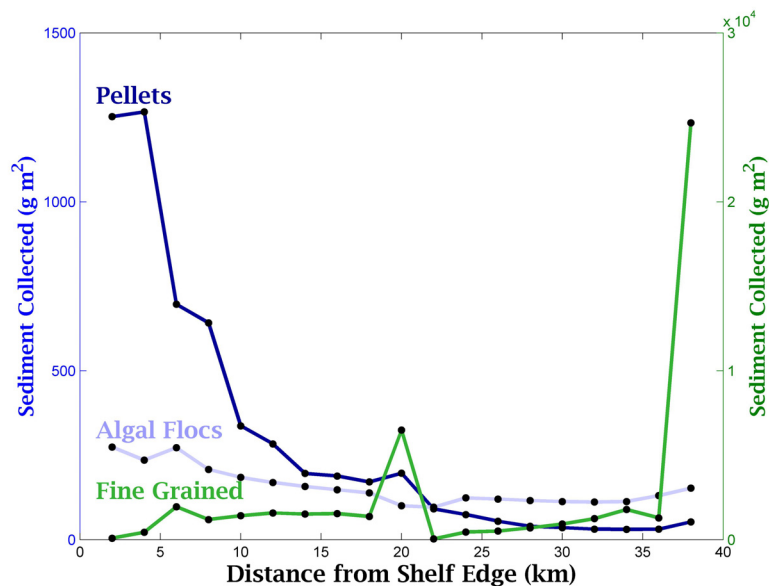


Figure 7.14: Patterns of deposition after five years of seasonal forcing with SF-Basin configuration. Blue (pellets and algal flocs) are read with the scale to the left, and green (fine mud) is read with the scale to the right.

Allowing the seasonality to be defined by the model dynamics resulted in a clear annual signal within the domain. The material drawn in from the western end was concentrated at approximately half the depth of the water column there, which depended on the particular seafloor configuration. For all simulations, the model domain was nearly emptied once per year, defining the annual cycle.

The highest rates of accumulation occurred close to the source, at the McMurdo Sound end of the domain. While deposition decreased smoothly with distance from McMurdo Sound, significant accumulation was seen across the entire width of the domain.

### **Algal flocs sourced from McMurdo Sound**

Algal flocs were sourced from McMurdo Sound, and were represented by a settling velocity of  $8.7 \times 10^{-4} \text{ m s}^{-1}$ . Replicating the higher fluxes observed at the seafloor (Dunbar et al., 1991, 1998; Langone et al., 2003), this material was supplied to all depths. The concentration of the boundary profile was varied seasonally, with maximum source concentration of  $40 \text{ g m}^{-3}$  in the summer months, and none supplied over winter.

The seasonality in both deposition at the seafloor and concentration within the domain was highly related to the annual pattern of the model dynamics. Significant deposition occurred across the entire width of the domain, with the highest rates typically closest to McMurdo Sound.

### **Fine mud sourced from McMurdo Sound**

The third sediment type sourced from the open water of McMurdo Sound was fine mud, represented by a settling velocity of  $7 \times 10^{-6} \text{ m s}^{-1}$ . Again this material was supplied through the whole depth of the water column to allow realistic fluxes near the seafloor. The boundary profiles were varied annually, with concentration up to  $18 \text{ g m}^{-3}$  in the summer, and none supplied over winter.

The material flowed into the domain from the western end in a layer  $\sim 300 \text{ m}$  thick immediately beneath the ice shelf. Although sediment was supplied close to the seafloor, only very low concentrations were seen there. A seasonal signal was seen in the concentration within the domain for all experiments, with the annual pattern established within the first year. Transitions between seasons was quite smooth, so that seasonality in the deposition pattern was not apparent.

The fine mud acted as a passive tracer, being descriptive of the circulation pattern. Highest accumulation rates were seen at the eastern end of the domain, deep under the ice shelf, reminiscent of the region of down-welling located there. A peak in deposition was seen in the centre of the basin in the experiments for the SF-Basin configuration. This was associated with a second region of down-welling resulting from the changing slope of the seafloor (described in section 7.3.1).

### **Sand sourced through the ice shelf**

The fourth sediment type was sourced within the ice shelf, assumed to have been blown onto the ice shelf surface from the Transantarctic Mountains to the east and south. This material was defined by the same settling velocity ( $1.7 \times 10^{-3} \text{ m s}^{-1}$ ) as was used for the pellets sourced at McMurdo Sound. The rate at which this sediment type was released from the ice shelf depended on the local basal melt rate. The concentration of sediment within the ice shelf, assumed to be constant, was set to  $1 \times 10^{-5} \text{ g m}^{-3}$ , tuned to deliver mass equivalent to 5% of the open water source - the upper limit observed at the Windless Bight sites (Barrett et al., 2004).

The relatively high settling velocity meant that the deposition pattern was strongly related to the release rate of sediment at the ice shelf base. As the melt rate was highest for the deepest part of the ice shelf, the accumulation was likewise highest there, with a smooth decrease back towards the western boundary. Since the local melt rate was quite stable for each cell along the base of the ice shelf, local release rates were likewise stable throughout the experiment.

Seasonality was not observed in either the concentrations of sediment in the water column or in the accumulation rates at the seafloor, since both of these relied on the rate of release at the ice shelf base. With annual forcing, the melt rate was only slightly seasonal, and this did not translate into a signal at the seafloor.

### **7.3.3 Conclusions**

Year-long observations of temperature and salinity from McMurdo Sound were available (Littlepage, 1965), and were used to force the model seasonally at the western open boundary. From the observations, mean profiles of temperature and salinity appropriate for the location were extracted, as well as the seasonal behaviour of these characteristics.

Persistent features associated with fluxes of heat and salt across the ice-ocean boundary were similar for all domain configurations, and apparent throughout the modelled year. This demonstrated that these were largely disconnected from the forcing at the open boundary and independent of seasonal variation within the domain. Results from seasonal forcing showed significant annual cyclicity in all variables, with smooth transitions between the seasons.

Seafloor shape was found to have a significant effect on overall circulation. With a constant slope, the densest water flowed down the seafloor surface, dominating the general flow by adding to or subtracting from the thermohaline circulation. The SF-Basin shape produced a region of downwelling over the centre of the basin, an artifact of the numerical calculations for those parts of the streamfunction. With a flat seafloor, the shape did not actively influence the circulation, and this configuration was found to be particularly sensitive to the seasonal forcing.

Sediment transport and deposition was introduced by means of passive tracers, with settling velocities imposed to represent different grain sizes. Transport and deposition patterns appropriate for each grain size were identified. Three sediment types, representing pellets, algal flocs and fine mud, were sourced from the McMurdo Sound end of the domain. This open water source provided the majority of the mass delivered to the seafloor, consistent with surface sediments recovered from the HWD sites. The ice shelf was a second possible source of sand, assumed to have been trapped in the ice. The amount of sediment released to the water column from this source depended on the prescribed concentration within the ice shelf, and on the local melt rate at the ice shelf base.

In general, the behaviour of each sediment type was consistent for different domain configurations. The pellets and sand dropped out of the water column and were deposited at the seafloor. When this was sourced from McMurdo Sound, accumulation was greatest near this open boundary, with a smooth decrease across the width of the domain. It was transported into the domain with annual cyclicity determined by the model dynamics. When it was sourced through the ice shelf, cyclicity was lost, as there was very little seasonal signal in the local melt rates at the ice shelf base. Fastest accumulation occurred beneath the deep end of the ice shelf. This was related to the higher melt rate there, and hence the greater sediment flux.

The fine mud was entrained into the circulation, and was descriptive of the general circulation pattern. A seasonal signal was imposed on the supply of this material, resulting in a strong signal in concentration within the domain. Annual patterns of deposition were not very apparent as this material remained in suspension long enough to be deposited throughout the year. Accumulation tended to be concentrated beneath local regions of downwelling, frequently located at the deep end of the ice shelf. A second region of downwelling was located over the centre of the basin, accompanied by a peak in the deposition of fine mud.

The algal flocs, having settling velocities between that of the pellets and fine mud, behaved in an intermediate manner with seasonality apparent in concentration and deposition patterns. Significant mass was delivered across the whole width of the domain, although greatest accumulation was closest to the source at McMurdo Sound. This type was influenced by the seafloor gradient, and flowed down the benthic slope, under the influence of the general circulation.

## Chapter 8

# Summary of this study and comparison of methods

This study forms part of a site survey conducted at Windless Bight on the McMurdo Ice Shelf, Antarctica, which will be the first site drilled by the multi-national project, ANDRILL (<http://andrift-server.unl.edu>). In order to interpret the core to be recovered, it was important to have a better knowledge of the local flow regime, as well as its context within the regional circulation. While currents in the open water near Ross Island have been measured and are fairly well-understood (reviewed in chapter 2), they have not previously been directly measured beneath the McMurdo Ice Shelf. To investigate the sub-ice shelf circulation at Windless Bight, three sites were occupied during January and February 2003. At one of these sites, a single current meter (ADCP) was moored at the edge of the McMurdo Ice Shelf, where it surveyed the upper 300 m of the water column continuously for 23 days.

The other two sites were located on the McMurdo Ice Shelf, through which a hot water drill was used to access the ocean cavity beneath. At each of these sites, an array of three ADCPs was used to survey  $\sim 300$  m of the 920 m of water column over periods of 2 - 3 days. In addition, at least ten profiles of temperature and salinity were collected through the entire water column over one diurnal tidal cycle at each site with a Seabird CTD (Conductivity-Temperature-Depth) profiler.

The spatial separation of the sites allowed connection between the new sub-ice shelf observations, and the previously studied area of McMurdo Sound. It also allowed comparison of the current regimes beneath the sea ice and the ice shelf in the same season.

## 8.1 Analysis of data from study sites

### Current meter measurements from the edge of the McMurdo Ice Shelf

The 23-day ADCP current meter mooring from the sea ice platform was long enough to allow comparison of flow during spring and neap tides. During the spring tide, flow was strongly oscillating along a narrow, well-defined SE-NW direction, and yet there was net throughflow of  $0.09 \text{ m s}^{-1}$  to the southeast, under the McMurdo Ice Shelf. Maximum flows were observed within the top 100 m of the water column, with the peak flow of  $0.7 \text{ m s}^{-1}$  recorded at 70 m during the middle of the spring tide. The flow in the top and middle sections of the water column was highly correlated over the spring tide, demonstrating a similar response to the tidal height variation.

In contrast, over the neap tide correlation of flow between the top and middle sections was much lower. The top section (to  $\sim 50 \text{ m}$ ) was observed to vary in much the same way as it had during the spring tide. However, in mid-water ( $\sim 75 \text{ m} - 300 \text{ m}$ ), the tidal signal was virtually non-existent, with flow fairly consistent towards the southeast. This demonstrated that the much weaker tidal forcing was able to affect only the surface waters. With the more consistent flow to the southeast, a much higher average throughflow of  $0.20 \text{ m s}^{-1}$  was observed over neap tide.

### Current meter measurements along the channel at spring tide

Together, data from the three sites revealed a picture of the flow in the channel over the spring tide. The tidal height signal was clearly evident in all records, and coherent throughout the whole depth surveyed at each site. Maximum speeds from all sites and all depths were recorded at flood tide. The peak flow at the two ice shelf sites was  $0.22 \text{ m s}^{-1}$ , recorded in the boundary layer beneath the ice shelf the first Hot Water Drill site, HWD-1.

Flow past each site was approximately parallel to the local direction of the channel around Ross Island - south-east at the sea-ice site, east at HWD-1, and north-east at HWD-2 - with shearing towards north amounting to  $\sim 30^\circ$  down the water column observed at each of the HWD sites.

The base of the ice shelf and the seafloor influenced flow beneath the ice shelf measurably. Flow along the base of the ice shelf was consistently higher (by up to 20%) than over the rest of the water column. Flow along the seafloor and ice shelf base appeared to

lag the simultaneous measurements from the sea ice by about 1 hour, whereas no phase shift was observed in the middle of the water column.

Flow over the spring tide at the three sites was consistent with strongly oscillating flow along the channel south of Ross Island, and net transport eastwards from McMurdo Sound. Strong oscillations in the eastwards velocity component existed for all three sites, but the tidal signal in the northward velocity component was progressively lost with distance from McMurdo Sound. The presence of Ross Island immediately to the north restricted flow in the N-S direction, damping the tidal signal in this component of velocity.

Based on the behaviour observed at the sea ice site, slightly higher peak current speeds and throughflow could be expected at the two HWD sites during neap tides, compared to those found during the spring tides.

### **Profiles of temperature and salinity beneath the McMurdo Ice Shelf**

Similar structure for both temperature and salinity was observed at the two HWD sites on the McMurdo Ice Shelf. Salinity increased monotonically to a value of 34.72 psu at the seafloor, with a steeper gradient within  $\sim 200$  m of the ice shelf base. A tongue of relatively warm water near the base of the ice shelf appeared and was modified through successive casts. Further down, a cold tongue extended for  $\sim 200$  m, within which the coldest water,  $-1.94^{\circ}\text{C}$ , was observed. The temperature gradually increased to  $-1.91^{\circ}\text{C}$  at the seafloor.

At HWD-1, the temperature and salinity at the base of the ice shelf indicated that the water there was supercooled by  $0.02^{\circ}\text{C}$ . The extent of this cooling was equivalent to freezing on to the ice shelf at a rate of  $0.88\text{ m yr}^{-1}$ . Significant variation was observed in both temperature and salinity down to  $\sim 300$  metres below sea level (m BSL), although this could not be related to the diurnal tidal cycle.

At HWD-2, the variation in the surface waters was considerably less than at HWD-1. This was associated with the greater distance to the open water of McMurdo Sound. The temperature at the base of the ice shelf was on average  $0.05^{\circ}\text{C}$  above the *in-situ* freezing temperature, implying melting at a rate of  $2.15\text{ m yr}^{-1}$ . The change in regime from freezing to melting between the two HWD sites reflects the classic picture of sub-ice shelf circulation, with melting deep under the ice shelf and freezing at shallower drafts.

The sub-ice shelf profiles were compared to others from the open water to either side of Ross Island, and from deep under the Ross Ice Shelf at station ‘J9’ (Clough and Hansen, 1979). In the open water, surface salinity and temperature values varied on a much larger scale than was observed beneath the ice shelf. Below  $\sim 250$  m, however, the two sub-ice shelf profiles closely resembled those of the open water on both sides of Ross Island, as well as those from station ‘J9’.

High Salinity Shelf Water (HSSW) was identified in profiles from the open water on both sides of Ross Island, filling the lower section of the water column. HSSW was not observed beneath the ice shelf in this study, although the variability of the temperature and salinity profiles indicated an open water source. Water of an appropriate temperature, but fresher than HSSW was observed beneath the ice shelf, perhaps formed from HSSW mixing with melt water at the surface freezing temperature. The direct supply of HSSW to the ice shelf cavity was most likely blocked by the sill at the southern end of McMurdo Sound, preventing its transport from the west. No such sill exists to block direct transport of HSSW from the open water to the east of Ross Island. The lack of identifiable HSSW indicates that supply to the sub-ice shelf ocean was from McMurdo Sound, supporting the conclusions drawn from analysis of the current meter data.

## 8.2 Modelling study

The Antarctic ice shelves insulate about 40% of the water on the continental shelf from direct atmospheric forcing, resulting in a unique oceanic environment. Numerical models have been used to gain increased understanding of the sub-ice shelf ocean processes, as the thick ice shelves make direct access difficult.

To model the flow in a curved channel beneath the McMurdo Ice Shelf at Windless Bight, an adaptation of the two-dimensional Hellmer and Olbers (1991) model has been used. This formulation required net throughflow to be calculated, and this parameter was used to diagnose the model’s stability over time. Profiles of temperature and salinity from southern McMurdo Sound, collected over one year (Littlepage, 1965), were used to seasonally force the model at the McMurdo Sound end of the channel. At the other end, also open to the ocean, constant profiles were used with weaker forcing to keep values there within a reasonable range. The model was found to be stable, with repeating an-

nual signals, which were set up within the first year of the experiments.

A new feature for this adaptation was the addition of sediment as a passive tracer. Sediment of various types and grain sizes, parameterised by settling velocity, was sourced from the open boundary at McMurdo Sound and through the ice shelf. Although this method was simple, it was found to be effective. Behaviour within the water column, and deposition at the seafloor of the various grain sizes were found to relate well to observations from McMurdo Sound and Windless Bight.

Some features of the circulation were largely independent of the processes at the open boundary, and were largely unconnected to the seasonal forcing. They included the continual transport of fresh meltwater up the slope of the ice shelf base, and down-welling towards the deep end of the ice shelf. At the deep end of the ice shelf the model showed melting equivalent to  $\sim 0.6 \text{ m yr}^{-1}$ , with this rate decreasing monotonically towards the open water. Freezing on equivalent to  $0.16 \text{ m yr}^{-1}$  was seen near the western end of the domain, with the location of the melt/freeze boundary moving in response to seasonal forcing. During winter months of model time, the melt/freeze transition was located deeper under the ice shelf, moving to shallower depths during summer months.

With a series of experiments to test the model response to various parameters, it was established that the standard settings, incorporated as the model was being built, were the most appropriate. With these parameters controlling the general circulation, further experiments were run to test the behaviour of sediment within the water column with settling velocity representing grain size. As expected, the sedimentation environment was found to be highly sensitive to prescribed settling velocity, with pellets and fine sand (settling velocity of  $1.7 \times 10^{-3} \text{ m s}^{-1}$ ) depositing quickly. Fine mud (settling velocity of  $7 \times 10^{-6} \text{ m s}^{-1}$ ) was entrained into the circulation and carried large distances before being deposited. They were transported to the seafloor in regions of downwelling rather than by settling out of the water column.

Using the results from these tests, the depositional environment was tuned to match observations from cores collected through the ice shelf at Windless Bight. Pellets, algal flocs and fine mud were sourced from the McMurdo Sound end of the domain. The pellets were preferentially deposited close to the source, with a smooth drop-off in accumulation rate with distance from McMurdo Sound. The fine mud became entrained and described

the overall circulation. This was primarily deposited by regions of down-welling, with peaks in the accumulation generally observed towards either end of the domain.

Sand blown onto the surface of the ice shelf was also considered as a further source of sand, with the amount released dependent on the local melt rate. With the relatively high settling velocity, sand deposition was strongly related to the release rate at the ice shelf base. Greatest accumulation was seen towards the deep end of the ice shelf, where the melt rate was highest, with a smooth drop in accumulation back towards the McMurdo Sound end of the domain. Slight seasonal signals in melt/freeze rates were seen, but this did not translate into a seasonal signal either within the domain, or in the deposition pattern.

Adding shape to the seafloor was found to dominate the circulation by promoting continual flow of the densest waters down the seafloor slope. When these slopes combined to form a basin, a region of down-welling was consistently located over the center of the basin. This was interpreted as an artefact of the model. Of the four seafloor configurations trialled, the domain with a flat seafloor was found to be the most responsive to seasonal forcing.

### 8.3 Comparison of methods

For this adaptation of a thermohaline circulation model to the cavity at Windless Bight, seasonal forcing was applied using year-long observations of temperature and salinity from southern McMurdo Sound (Littlepage, 1965). This was different to the method of sinusoidal variation on average profiles used in Hellmer and Olbers (1991), although the main features of the sub-ice shelf circulation were reproduced. As with Hellmer and Olbers (1991), the fluxes of heat and salt across the ice-ocean interface were sufficient to drive circulation, seen here in the first spin-up phase.

Once exchange with the ocean was allowed through the open boundaries, melting of the ice shelf at depth, and the resulting flow of cool, fresh water up the base of the ice shelf, were seen. This was continual and steady with time-independent forcing in the second spin-up phase. A seasonal signal within the domain was only seen once this was applied at the McMurdo Sound open boundary. The highest melt rates of  $\sim 0.6 \text{ m yr}^{-1}$  were seen at the deep end of the ice shelf, and were of a similar magnitude to those implied from

observed temperatures at HWD-2. A monotonic decrease in melt rate towards the open water resulted in a change to a freezing regime closer to the western boundary, corresponding to observations at the HWD sites. Both the HWD observations and the model results fitted the classic picture of sub-ice shelf thermohaline circulation, which melts ice at depth, and has refreezing of ice at shallower ice shelf drafts.

Ice Shelf Water (ISW) was created by the model and was present throughout the year due to the low ranges of temperature and salinity values within the model domain. The ISW was not formed deep enough to become neutrally buoyant as it traversed the basal slope, so unlike the behaviour in Hellmer and Olbers (1991), it did not detach from the ice shelf to flow toward the open boundary in plumes.

As with Hellmer and Olbers (1991), convection was a major feature of this model, with the most consistent region of downwelling located towards the deep end of the ice shelf. The effect of this cell was seen in the accumulation pattern of fine mud, transported to the seafloor within this cell.

This model formulation, with application to a channel open at both ends, required the calculation of net throughflow at each timestep. Generally, transport within the model was only slightly lower than that observed at the HWD sites. Differences were expected, as the HWD sites were occupied for only short periods, with tidal variation the dominant feature in the data, as opposed to the annual forcing applied in the model.

An adaptation of this model has also been applied to the ocean cavity beneath the eastern Ross Ice Shelf (Hellmer and Jacobs, 1995), using a two-dimensional channel, curved around Roosevelt Island. Year-long observations of salinity and temperature were used to force the model annually at the front of the ice shelf, producing seasonal variation within the model domain. The rates of basal melting,  $0.18 - 0.27 \text{ m yr}^{-1}$  found by Hellmer and Jacobs (1995), were much lower than were seen in this study. This difference may be attributable to the proximity of the Windless Bight sites to the highly variable waters of McMurdo Sound.

Peak velocities seen in the adaptation by Hellmer and Jacobs (1995) were less than half of those seen in this study. This may have been related to the different volumes of meltwater produced by the two adaptations, as the highest velocities in this study were associated

with the buoyant flow of meltwater up the ice shelf base. The slope of the ice shelf base was an order of magnitude higher in this study, which would have increased the speed of the flow there. The difference may also have been due to the different model configurations, with flow assumed to follow paths of constant water column thickness in the adaptation by Hellmer and Jacobs (1995). They achieved different model domain shapes by maintaining a standard ice shelf topography and adjusting the seafloor bathymetry to produce the required water column thickness. The introduction of shape to the seafloor was seen in this study to have an influence on the general circulation far greater than the seasonal variation of salinity and temperature at the open boundary.

In their adaptation, meltwater exited the eastern cavity year-round, corresponding to the continual flow of fresh meltwater up the ice base seen in this study. For the western cavity, those times of the year when the meltwater plume was not present coincided with a weak counterflow near the seafloor, driven by a reverse density gradient at the ice shelf front. A similar feature was seen periodically throughout the year in this study. This benthic flow was responsible for drawing significant volumes of sediment into the model.

The adaptation of the sub-ice shelf thermohaline ocean model of Hellmer and Olbers (1991) used in this study for the cavity beneath the McMurdo Ice Shelf incorporated some changes. These were mostly related to the shape of the model domain, better representing bathymetry and ice shelf topography at Windless Bight. Spatial resolution was higher, possible because of the smaller spatial extent of this study. In addition, sediment transport and deposition was investigated through the addition of passive tracers onto which settling velocities, representing grain size, were imposed. This method, although simple, was found to be effective, with behaviours of the sediment types consistent throughout the experiments, and corresponding to observed depositional patterns.

To improve on this investigation, the effect of tidal height variation could be incorporated, observed at the HWD sites to affect the entire water column simultaneously and to a similar degree. With strongly oscillating flow near the seafloor, sedimentary material in the benthic layer may be re-entrained several times before it is eventually deposited, perhaps at great distance from the original source. Higher vertical resolution near the seafloor would be required in order to understand this process better. This could be achieved by coupling the thermohaline general circulation ocean model to a high resolution turbulence model applied near the seafloor.

# Appendix A

## Formulation of numerical model

### A.1 Derivation of vorticity equation in 2-dimensions

Motion of an incompressible sub-ice shelf ocean can be described by the Boussinesq and hydrostatic approximations of the momentum balance:

$$u_t + uu_x + vv_y + ww_z - fv = -p_x + A_H(u_{xx} + u_{yy}) + A_V u_{zz}, \quad (\text{A.1})$$

$$v_t + uv_x + vv_y + ww_z + fu = -p_y + A_H(v_{xx} + v_{yy}) + A_V v_{zz}, \quad (\text{A.2})$$

$$0 = -p_z - g\rho; \quad (\text{A.3})$$

and the continuity equation:

$$u_x + v_y + w_z = 0, \quad (\text{A.4})$$

where  $u$ ,  $v$ ,  $w$  are velocities in the  $x$ ,  $y$  and  $z$  directions respectively, and subscripts represent the finite difference derivatives in time and space of the variables.

The circulation is assumed to be predominantly two-dimensional, with  $u \ll v$ , so  $x$ -velocities,  $x$ -gradients and Coriolis terms are neglected. Equation A.1 is thus redundant. In two-dimensions, equation A.2 becomes

$$v_t + vv_y + ww_z = -p_y + A_H v_{yy} + A_V v_{zz}; \quad (\text{A.5})$$

and the continuity equation in two-dimensions becomes

$$v_y + w_z = 0. \quad (\text{A.6})$$

With the streamfunction defined by

$$v = \Psi_z \text{ and } w = -\Psi_y, \quad (\text{A.7})$$

equation A.5 becomes

$$\Psi_{zzt} + (v\Psi_{zz})_y + (w\Psi_{zz})_z = g\rho_y + A_H\Psi_{zzyy} + A_V\Psi_{zzzz}. \quad (\text{A.8})$$

Thermohaline processes enter via the density torque  $g\rho_y$  where the density  $\rho$  is a function of potential temperature  $\Theta$ , salinity  $S$  and pressure (depth).

## A.2 Extension of two-dimensional channel flow to allow net transport

The formulation of the previous section was used by Hellmer and Olbers (1989) for flow in a channel closed at one end by the grounded ice shelf. In that case, the boundary conditions of the streamfunction were satisfied by setting  $\Psi$  equal to an arbitrary constant on the boundary. For a channel open at both ends (as in Hellmer and Olbers (1991)), we may set

$$\Psi = 0 \text{ at the seafloor } (z = -h_B), \quad (\text{A.9})$$

$$\Psi = \gamma(t) \text{ at the ice shelf base } (z = -h_I) \quad (\text{A.10})$$

with the function  $\gamma(t)$  yet to be determined, but actually equalling the total transport through the channel. In order to solve the vorticity equation (eq. A.8) and determine  $\gamma(t)$  we redefine  $\Psi$  as

$$\Psi = \theta + \phi, \quad (\text{A.11})$$

where  $\theta$  represents the circulating part of the streamfunction, and hence has no flow across the open boundaries.  $\phi$  represents the net transport of the streamfunction with the result that on the boundary  $\theta = 0$  and  $\Psi = \phi$ . We also set  $\theta_{zz} = \Psi_{zz}$  everywhere, a known function of values from the previous timestep. i.e.,

$$\theta_{zz}^{i+1} = \Psi_{zz}^{i+1} = f(\Psi^i). \quad (\text{A.12})$$

Hence

$$\phi_{zz}^{i+1} = 0, \quad (\text{A.13})$$

$$\Rightarrow \phi_z = K(y), \quad (\text{A.14})$$

$$\Rightarrow \phi = Kz + C \quad (\text{A.15})$$

and since on the open boundaries,  $\phi = \Psi = 0$  at  $z = -h_B$  and  $\phi = \Psi = \gamma(t)$  at  $z = -h_I$ , we have (from equation A.15)

$$\phi_{(z=-h_B)} = K \cdot (-h_B) + C = 0, \quad (\text{A.16})$$

$$\text{and } \phi_{(z=-h_I)} = K \cdot (-h_I) + C = \gamma(t), \quad (\text{A.17})$$

$$\Rightarrow C = Kh_B. \quad (\text{A.18})$$

$$\gamma(t) = -Kh_I + Kh_B = K\Delta h \quad (\text{A.19})$$

$$\Rightarrow K = \phi_z = \frac{\gamma(t)}{\Delta h} \quad (\text{A.20})$$

Now, use the known conditions on the open boundary to determine  $\gamma(t)$ . From equation A.15:

$$\phi = Kz + C \quad (\text{A.21})$$

$$= Kz + Kh_B \quad (\text{A.22})$$

$$= K(z + h_B) \quad (\text{A.23})$$

$$= \frac{\gamma(t)}{\Delta h}(z + h_B) \text{ (from eq. A.20)} \quad (\text{A.24})$$

$$\Rightarrow \phi_z^{i+1} = \frac{\gamma^{i+1}}{(\Delta h)} \quad (\text{A.25})$$

This allows calculation of  $\phi_z^{i+1}$  everywhere as a function of  $\Delta h$ , since  $\gamma(t)^{i+1}$ , the net flow through the channel, does not change in space. We can now calculate the updated  $\frac{\delta v}{\delta t}$  everywhere, from

$$v_t^{i+1} = \Psi_{zt}^{i+1} = \frac{\theta_z^{i+1} + \phi_z^{i+1} - (\theta_z^i + \phi_z^i)}{\Delta t}, \quad (\text{A.26})$$

since all terms other than  $\phi_z^{i+1}$  are known functions of values from the previous time-step. ( $\theta_z^{i+1} = f(\Psi^i)$  and  $\theta = 0$  on boundary.) This can then be used to calculate the pressure difference at the two open ends of the channel from

$$p_2 - p_1 = \int_{\Gamma} \underline{\nabla} p \cdot d\underline{s} = \int_Z^{\xi} g\rho dz'|_2 - \int_Z^{\xi} g\rho dz'|_1 \quad (\text{A.27})$$

where

$$-\underline{\nabla} p = -(p_y, p_z) = (v_t + vv_y + ww_z - A_H v_{yy} - A_V v_{zz}, g\rho) \quad (\text{A.28})$$

The choice of  $\Gamma$  is arbitrary, so choosing  $\Gamma$  to be a horizontal path along the channel removes the  $z$ -component. Using equation A.28, A.27 then becomes

$$p_2 - p_1 = \int_{\Gamma} \underline{\nabla} p \cdot d\underline{s} = \int_{y=a}^{y=b} (v_t + vv_y + ww_z - A_H v_{yy} - A_V v_{zz}) dy, \quad (\text{A.29})$$

which can be directly calculated. New values for  $v, w$  and their derivatives can be used, calculated from the definition of the streamfunction (eq. A.7). Discretizing, equation A.29 becomes

$$p_2 - p_1 = \int \nabla p = \sum_{j=a}^b \left( \frac{\gamma}{\Delta h_j} + A_j \right) \Delta y. \quad (\text{A.30})$$

Using the difference of hydrostatic pressure between the open ends of the channel ( $p_2 - p_1$ ), this yields  $\gamma(t)$ , the net throughflow.  $\gamma$  is used as a boundary condition for  $\phi$ , connecting the streamfunction to the pressure gradient between the ends of the channel.

### A.3 Calculating $\gamma(t)$ - net throughflow

Using the streamfunction split into its circulating and throughflow parts,

$$\Psi = \theta + \phi \Rightarrow \Psi_z = \theta_z + \phi_z, \quad (\text{A.31})$$

and applying equations A.15 and A.20, so that  $\phi_y = 0$  and  $\phi_{zz} = 0$ , the following relationships for the terms in A.29 are found:

$$v = \Psi_z = \theta_z + \phi_z = \theta_z + \frac{\gamma}{\Delta h}; \quad (\text{A.32})$$

$$v_{zz} = \Psi_{zzz} = \theta_{zzz}; \quad (\text{A.33})$$

$$v_{yy} = \Psi_{zyy} = \theta_{zyy}; \quad (\text{A.34})$$

$$\text{and } w = -\Psi_y = -\theta_y - \phi_y = -\theta_y \quad (\text{A.35})$$

Rewriting equation A.29 in these terms yields

$$p_1 - p_2 = \int_{\Gamma} \left[ \left( \theta_z + \frac{\gamma}{\Delta h} \right)_t + \left( \theta_z + \frac{\gamma}{\Delta h} \right) \theta_{zy} - \theta_y \theta_{zz} - A_H \theta_{zyy} - A_V \theta_{zzz} \right] dy \quad (\text{A.36})$$

$$= \int_{\Gamma} \left( \left( \frac{\gamma}{\Delta h} \right)_t + \left( \frac{\gamma}{\Delta h} \right) \theta_{zy} \right) dy + \int_{\Gamma} (\theta_{zt} + \theta_z \theta_{zy} - \theta_y \theta_{zz} - A_H \theta_{zyy} - A_V \theta_{zzz}) dy \quad (\text{A.37})$$

$$p_1 - p_2 - \int_{\Gamma} (\theta_{zt} + \theta_z \theta_{zy} - \theta_y \theta_{zz} - A_H \theta_{zyy} - A_V \theta_{zzz}) dy = \int_{y=a}^{y=b} \left( \frac{\gamma}{\Delta h} \right)_t dy + \int_{y=a}^{y=b} \left( \frac{\gamma}{\Delta h} \right) \theta_{zy} dy \quad (\text{A.38})$$

$$= \left( \frac{\gamma}{\Delta h} \right)_t (b - a) + \left( \frac{\gamma}{\Delta h} \right) \theta_z \Big|_a^b \quad (\text{A.39})$$

$$= \frac{\gamma^t}{\Delta h} (b - a) + \left( \frac{\gamma}{\Delta h} \right) \theta_z \Big|_a^b \quad (\text{A.40})$$

$$= \frac{\gamma^{t+1} - \gamma^t}{\Delta t \Delta h} (b - a) + \left( \frac{\gamma^t}{\Delta h} \right) \theta_z \Big|_a^b \quad (\text{A.41})$$

$$= \frac{\gamma^{t+1}}{\Delta t \Delta h} (b - a) - \frac{\gamma^t}{\Delta t \Delta h} (b - a) + \left( \frac{\gamma^t}{\Delta h} \right) \theta_z \Big|_a^b \quad (\text{A.42})$$

$$\Rightarrow \frac{\gamma^{t+1}}{\Delta t \Delta h} (b-a) = p_1 - p_2 - \int_{\Gamma} (\theta_{zt} + \theta_z \theta_{zy} - \theta_y \theta_{zz} - A_H \theta_{zyy} - A_V \theta_{zzz}) dy + \frac{\gamma^t}{\Delta t \Delta h} (b-a) - \frac{\gamma^t}{\Delta h} \theta_z \Big|_a^b \quad (\text{A.43})$$

This implies that

$$\gamma^{t+1} = \frac{\Delta t \Delta h}{b-a} \left[ \frac{\gamma^t}{\Delta t \Delta h} (b-a) - \frac{\gamma^t}{\Delta h} \theta_z \Big|_a^b + p_1 - p_2 - \int_{\Gamma} (\theta_{zt} + \theta_z \theta_{zy} - \theta_y \theta_{zz} - A_H \theta_{zyy} - A_V \theta_{zzz}) dy \right] \quad (\text{A.44})$$

$$= \gamma^t - \frac{\Delta t \gamma^t}{b-a} \theta_z \Big|_a^b + \frac{\Delta t \Delta h}{b-a} \left[ p_1 - p_2 - \int_{\Gamma} (\theta_{zt} + \theta_z \theta_{zy} - \theta_y \theta_{zz} - A_H \theta_{zyy} - A_V \theta_{zzz}) dy \right] \quad (\text{A.45})$$

Thus  $\gamma$  can be found at the next timestep.

# Appendix B

Water column current profile analysis from beneath  
the McMurdo Ice Shelf at Windless Bight and under  
the sea ice in Granite Harbour, Antarctica

Natalie Robinson and Alex Pyne  
Antarctic Research Centre  
Victoria University of Wellington  
P.O. Box 600  
WELLINGTON 6001

November 2003

## Contents

<b>1</b>	<b>McMurdo Ice Shelf: Water Current Velocity Profiles from S4 and ADCP data</b>	<b>110</b>
1.1	Background . . . . .	110
1.2	The Data Sets . . . . .	110
1.3	How Profiles Were Created . . . . .	113
1.3.1	Mooring Data - ADCPs + S4 . . . . .	113
1.3.2	S4 Casts . . . . .	117
1.4	Discussion of Data . . . . .	117
1.5	Resultant Profiles . . . . .	120
1.6	Acknowledgement . . . . .	120
<b>2</b>	<b>Granite Harbour: Water Current Velocity Profiles from ADCP data</b>	<b>122</b>
2.1	Background . . . . .	122
2.2	Moorings . . . . .	122
2.2.1	Magnetic deviation . . . . .	124
2.3	Acknowledgement . . . . .	126
<b>3</b>	<b>Appendices</b>	<b>131</b>
3.1	Appendix 1 - Windless Bight . . . . .	131
3.2	Appendix 2 - Granite Harbour . . . . .	139

## List of Figures

1	Bathymetry map of Windless Bight area . . . . .	111
2	Tidal data measured at Scott Base . . . . .	111
3	Mooring Diagram for Windless Bight Sites . . . . .	112
4	Comparison of ADCP and S4 data at HWD-1 and HWD-2 . . . . .	114
5	Current Speed and Direction measured at HWD-1 . . . . .	115
6	Current Speed and Direction measured at HWD-2 . . . . .	116
7	Current Speed for every cast at sites HWD-1 and HWD-2 measured with S4 instrument . . . . .	118
8	Representative S4 casts overlaid with ADCP data for producing maximum current profiles at sites HWD-1 and HWD-2 . . . . .	119
9	Synthetic maximum speed profiles for sites HWD-1 and HWD-2 . . . . .	121
10	Bathymetry map of Granite Harbour Area . . . . .	122
11	Tidal data measured at Cape Roberts . . . . .	124
12	Mooring Diagram for Granite Harbour sites . . . . .	125
13	Current Speed and Direction measured at GH-1 . . . . .	127
14	Current Speed and Direction measured at GH-2 . . . . .	128
15	Synthetic maximum speed profiles for sites GH-1 and GH-2 overlaid with ADCP data . . . . .	129
16	Synthetic maximum speed profiles for sites GH-1 and GH-2 . . . . .	130

## List of Tables

1	Locations of Granite Harbour Sites . . . . .	123
2	Windless Bight Site HWD-1; ADCP and S4 setup data . . . . .	131
3	Windless Bight Site HWD-2; ADCP and S4 setup data . . . . .	132
4	Sample numbers defining ‘Up’ and ‘Down’ casts at HWD-1 . . . . .	133
5	Sample numbers defining ‘Up’ and ‘Down’ casts at HWD-2 . . . . .	133
6	Vertical velocity of S4 instrument through the water column at HWD-1 . . . . .	134
7	Vertical velocity of S4 instrument through the water column at HWD-2 . . . . .	134
8	Synthetic Profile for Windless Bight site HWD-1 . . . . .	135
9	Synthetic Profile for Windless Bight site HWD-2 . . . . .	136
10	Synthetic Profile for site GH-1 . . . . .	137
11	Synthetic Profile for site GH-2 . . . . .	138
12	Granite Harbour Site GH-1; ADCP and S4 setup data . . . . .	139
13	Granite Harbour Site GH-2; ADCP and S4 setup data . . . . .	140

This analysis and report has been prepared primarily for engineering modelling of the sea riser casing for the ANDRILL (McMurdo portfolio) drilling operation.

## **1 McMurdo Ice Shelf: Water Current Velocity Profiles from S4 and ADCP data**

### **1.1 Background**

In January 2003, two Hot Water Drill (HWD) holes were made through the McMurdo Ice Shelf approximately 6 and 12 km from Scott Base, Antarctica (See figure 1). Water samples were taken from different depths beneath the Ice Shelf in addition to the deployment of various instruments through the holes in the ice shelf. Profiling the water column beneath the ice shelf was achieved with casts of a current meter (Inter-Ocean S4) and a Seabird CTD (Conductivity-Temperature-Depth).

Longer term current data was obtained with a mooring of 3 Acoustic Doppler Current Profilers (ADCPs) deployed for a few diurnal tidal cycles, approximately covering the spring periods, figure 2. Two of the ADCPs were Sentinels, (Sentinel 327, Sentinel 600), used for observing large sections of the water column at once, while the third was a Navigator, used for observing the benthic boundary layer, especially for understanding sediment transport near the seafloor. (See figure 3 for diagram of mooring array.)

The two sites were located on seismic lines that will be used to define ANDRILL drilling targets, to be drilled from the ice shelf platform and coring 1000m into the sea floor.

This report details analysis of the measurements completed with the aim of deriving water column profiles during periods of maximum flow. The maximum flow profiles will be used for modelling and engineering for a steel sea riser, which will be the initial drill casing from the ice shelf surface to the sea floor.

### **1.2 The Data Sets**

The maximum flow profiles are created from 3 basic data sets for each of the two sites.

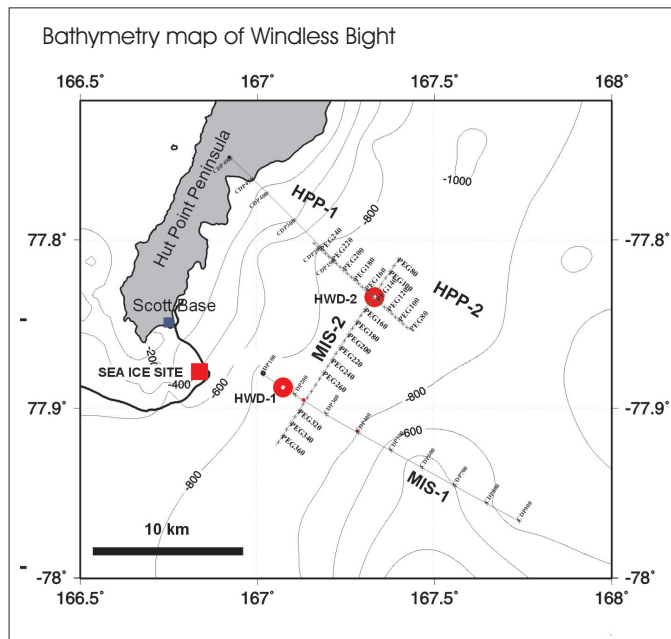


Figure 1: Bathymetry map of Windless Bight area showing location of seismic lines MIS-1, MIS-2, HPP-1, HPP-2. Also shown are the locations of moorings set in sea ice - Sea Ice Site - and shelf ice - HWD-1, HWD-2.

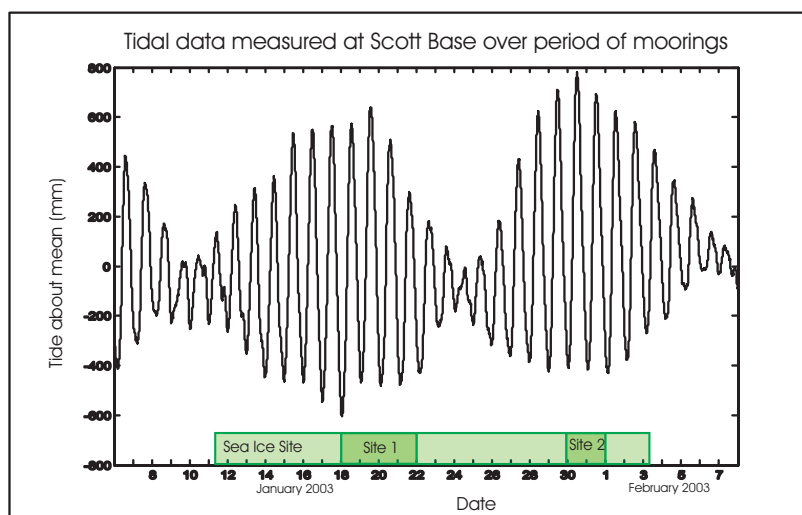


Figure 2: Tidal data measured at Scott Base (*Goring, personal communication 2003*). Tides corresponding to the timing of the moorings are shown. The two ice shelf moorings were timed to coincide with the maximum spring tides.

Site 1

Location	77°53.308'S, 167°05.067'E
Ice Thickness	70.5 m
Water Depth	918 m
Freeboard	17 m

12 x S4 current meter casts run every 2 - 2 ½ hours over a 30 hour period and 3 x Acoustic Doppler Current Profiler (ADCP) mooring of 86 hours.

Site 2

Location	77°50.111'S, 167°20.209'E
Ice Thickness	144 m
Water Depth	923 m
Freeboard	23 m

10 x S4 current meter casts run every 2 - 2 ½ hours over a 24 hour period and S4 mooring + ADCP mooring of 47 hours.

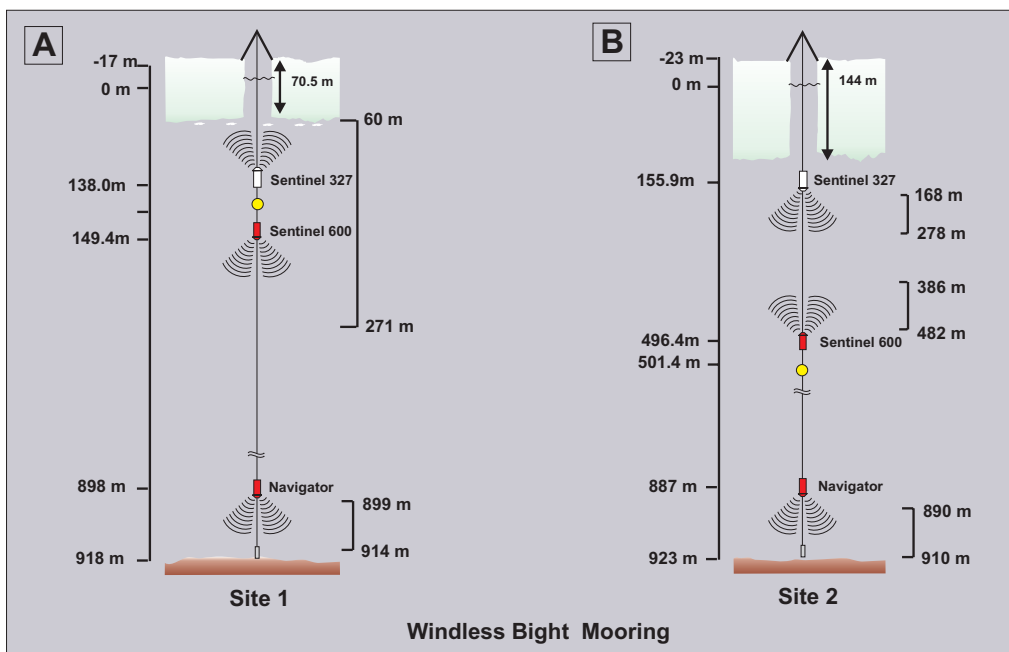


Figure 3: Diagram showing the mooring array at (A), HWD-1 and (B), HWD-2. The scale to the left indicates the depth below sea level at which each instrument was deployed. The ranges to the right indicate the sections of the water column observed by the ADCPs.

ADCP instruments measure currents (speed and direction) by sending out a burst of sound at a fixed frequency, periodically (every 2 seconds) and measuring the Doppler shift on the return signal after the sound is reflected from particulate in the water column. The instrument receives this return signal in a continuous stream, but can be set up to integrate over short time periods, relating directly to different depths (bins), effectively surveying a large depth range simultaneously. The S4 instrument measures currents (speed and direction) by creating a magnetic field and sensing the voltage induced by the movement of water through the field. When this instrument is used in profiling mode it is moved vertically through the water column.

In general, the data from the ADCPs are more reliable than that from the S4 for several reasons:

- The technology and instruments are newer;
- Measurements are taken at a number of depths simultaneously rather than just a single fixed point;
- Every measurement is an average of four instantaneous measurements separated spatially;
- The S4 profiles are obtained by “towing” the instrument vertically through the water column (‘down’ and ‘up’ casts), and although it measures current velocity in the horizontal plane, this vertical movement creates turbulence which has horizontal as well as vertical components. The data indicates that the S4 records current velocities higher than actual during profiling at the vertical speeds used, see tables 6 and 7.
- The S4 was the first of two instruments plus two water sampling bottles on the line being cast at the same time, so that, especially for up casts, there is potential for extraneous disturbance in the water column due to these other objects.

However, the combined ADCP data sets cover less than half of the available water column, and because of this, the S4 profiling data sets were used to ‘fill the gaps’, with the simultaneous mooring alongside the ADCP used as a reference for correlation.

### 1.3 How Profiles Were Created

#### 1.3.1 Mooring Data - ADCPs + S4

The S4 mooring data was taken every  $\frac{1}{2}$  second for one minute at the start of every 10 minutes. For purposes of comparison with ADCP data, these 120 samples were averaged

into a single measurement at the start of every 10 minute interval.

Initially, the S4 mooring speed data was directly compared with an average of ADCP data from the two bins closest to the S4. (For comparison of these two instruments, see figure 4.) This showed good correlation between the two instruments where high velocities ( $> 10\text{cms}^{-1}$ ) were recorded by the ADCP, but the S4 did not record velocities less than  $\sim 6\text{cms}^{-1}$ , and consequently there were long periods where the instruments did not agree.

In preparation for creating the maximum flow profiles, the periods of maximum current speed, as seen in the ADCP record were identified - 2 periods in each record. The vertical stripes, seen in figures 5 and 6, represent these periods of maximum flow, which are nearly simultaneous through the water column. These sub-sets of data were then extracted from the whole record, and plotted as a function of depth, figure 8. The black dots represent the first period, with red for the second period. The one set of green data is from a third period selected from Sn327 record (site 1), and was included because the other regions did not capture the highest currents immediately below the ice shelf.

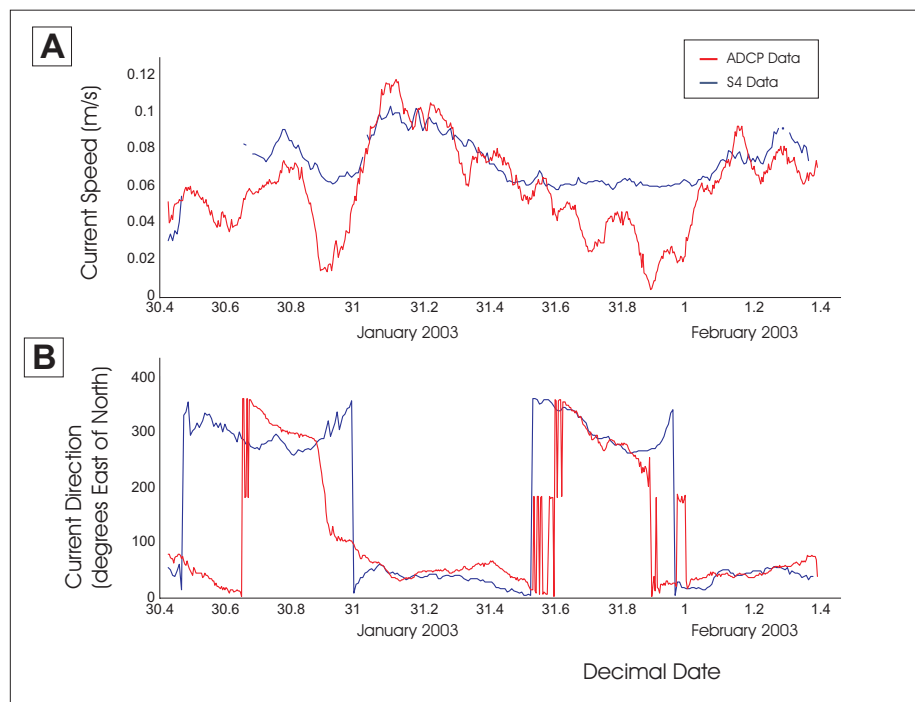


Figure 4: Comparison of (A), current speed and (B), current direction data from ADCP moored at 496.4m and S4. Good correspondence between the two instruments is seen for current speeds above  $\sim 0.06\text{ms}^{-1}$ . Below this value, the S4 data plateaus, indicating insufficient response from the instrument.

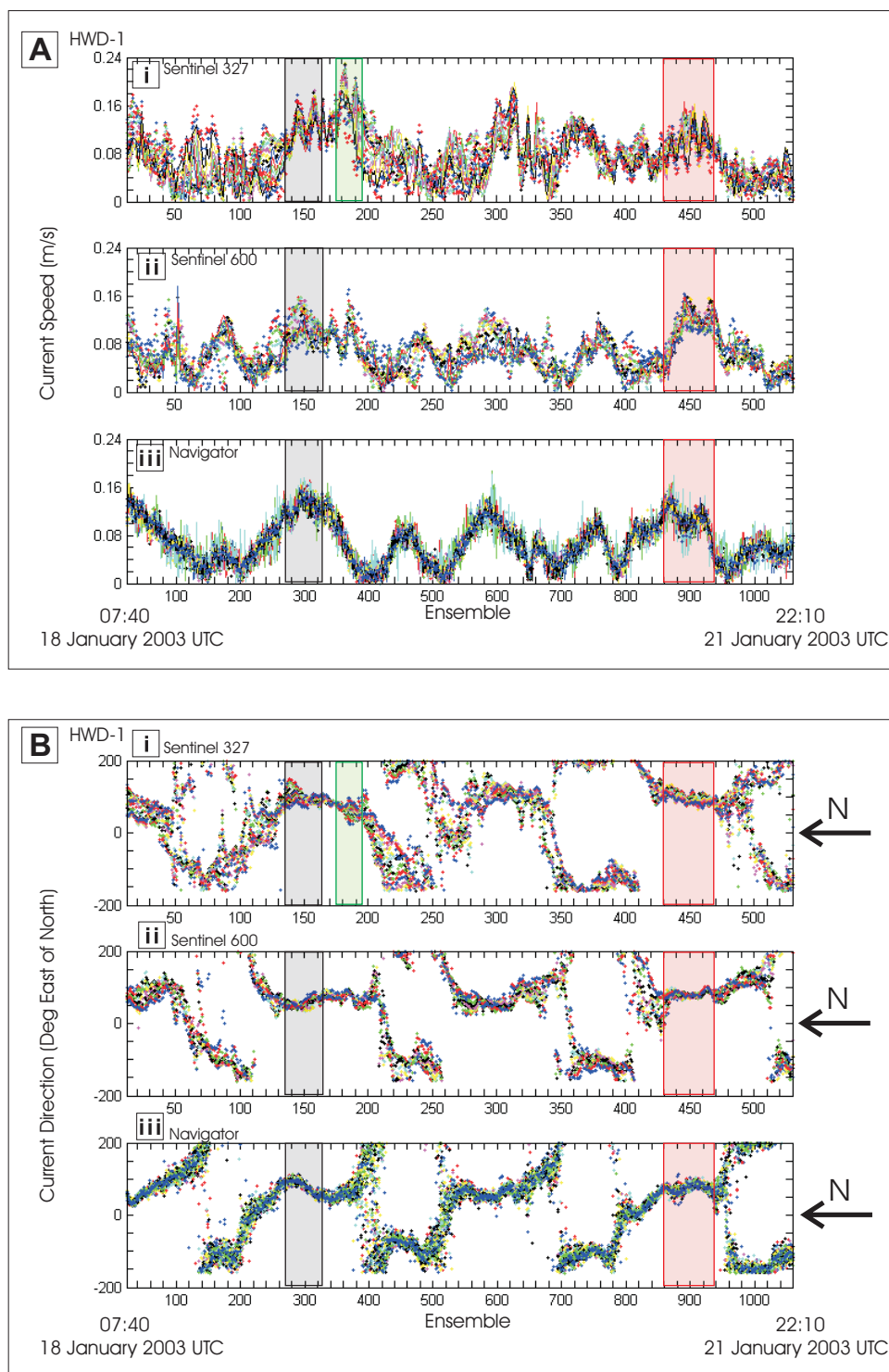


Figure 5: (A) Current speed and (B) current direction data from the three ADCP instruments at HWD-1. Time series (i) is from the Sentinel 327, (ii) Sentinel 600 and (iii) Navigator. Also shown are the short periods from which data were extracted for construction of maximum current profiles - Black, region 1, Green, region 1b, Red, region 2. The maximum current speed at each depth were captured, so the regions were not quite synchronous through the water column.

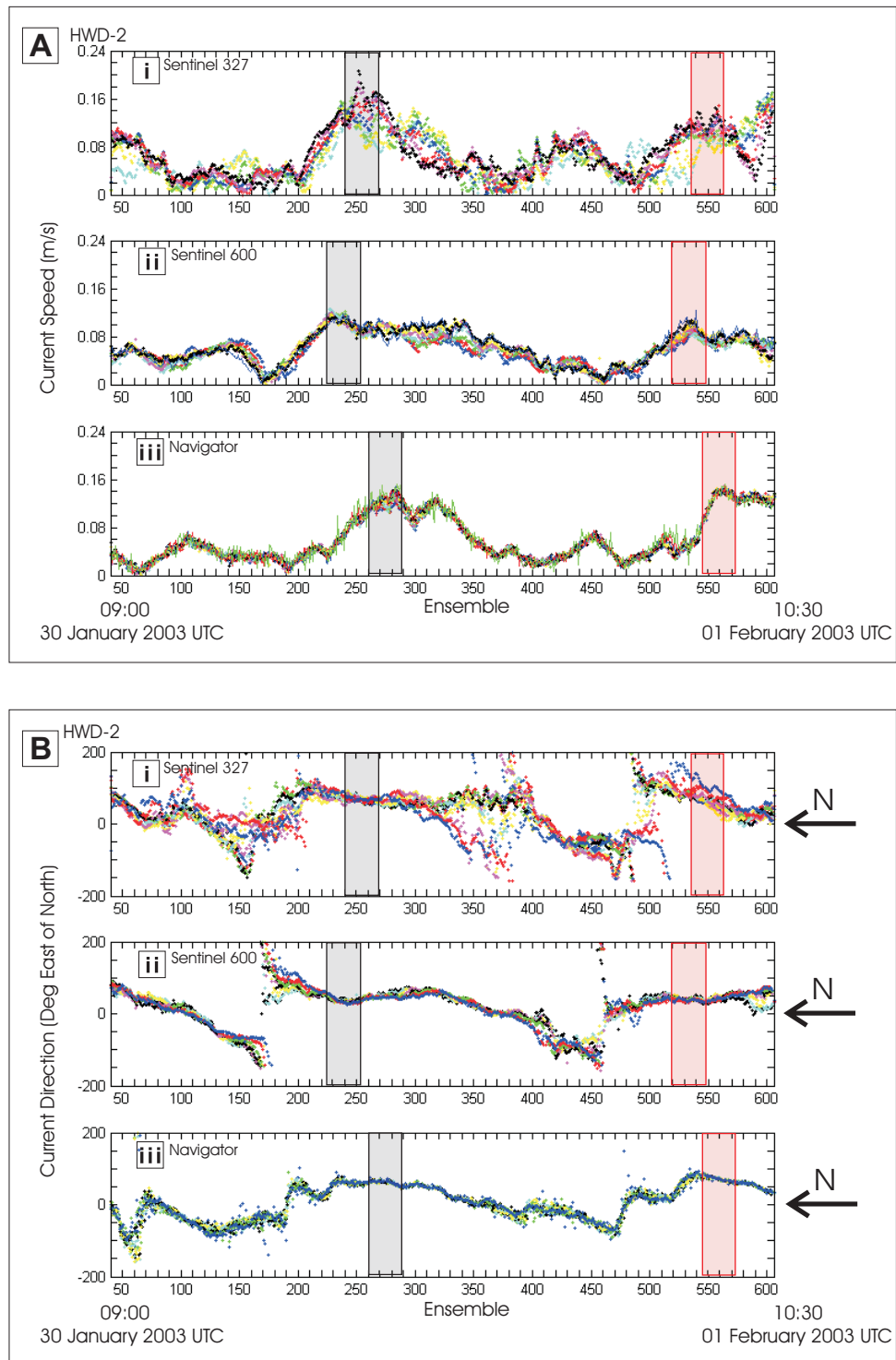


Figure 6: (A) Current speed and (B) current direction data from the three ADCP instruments at HWD-2. Time series (i) is from the Sentinel 327, (ii) Sentinel 600 and (iii) Navigator. Also shown are the short periods from which data were extracted for construction of maximum current profiles - Black, region 1, Green, region 1b, Red, region 2. The maximum current speed at each depth were captured, so the regions were not quite synchronous through the water column.

### 1.3.2 S4 Casts

The S4 profiles are acknowledged to be less accurate than the ADCP data, but can be considered to represent the ‘shape’ of the water column profile, and are used here to show that current speed and direction are probably reasonably consistent in the depth intervals of the water column not surveyed by the ADCP instruments. Each cast was separated into up and down casts, and considered separately. The up casts were smoother, even though velocity of the instrument through the water column was lower on the down casts. It was decided that the up casts seemed to provide more consistent profiles, so representative casts were all ‘up casts’, figure 7.

Again, for each site, all up casts were considered side by side in order to determine which was the ‘most representative’ cast, in terms of general shape through the water column. Since data had been collected every  $\frac{1}{2}$  second for the duration of each cast, a 10 second ‘running mean’ was applied before the comparison, in order to reveal the trend of the data, and to remove outlying points.

For Site 1 Cast #6 was selected.

For Site 2 Cast #2 and #4 were selected.

To produce a realistic profile, the chosen casts were then superimposed onto the data from the ADCPs at the previously determined periods of maximum current speeds. Overlaying the data sets showed that the S4 and ADCP data reveal the same general shape for the velocity profiles, but also that the S4 recorded much higher velocities. It is not likely that this difference results from the timing - the ADCP mooring followed the S4 casts - and so an appropriate offset was applied to the S4 data.

No offset was applied to the S4 data for Cast #6 data from Site 1, while offsets of  $0.17 \text{ ms}^{-1}$  and  $0.04 \text{ cms}^{-1}$  were applied to Cast #2 and Cast #4 respectively from Site 2. All three sets of data are shown on figure 8.

## 1.4 Discussion of Data

The ADCP instruments were programmed for a magnetic declination correction of  $155^\circ$  east of north prior to deployment and the S4 data corrected during post processing by subtracting  $145^\circ$  from each data point in the resultant series after averaging the 120 measurements taken in the first minute of every 10. When the direction data were compared

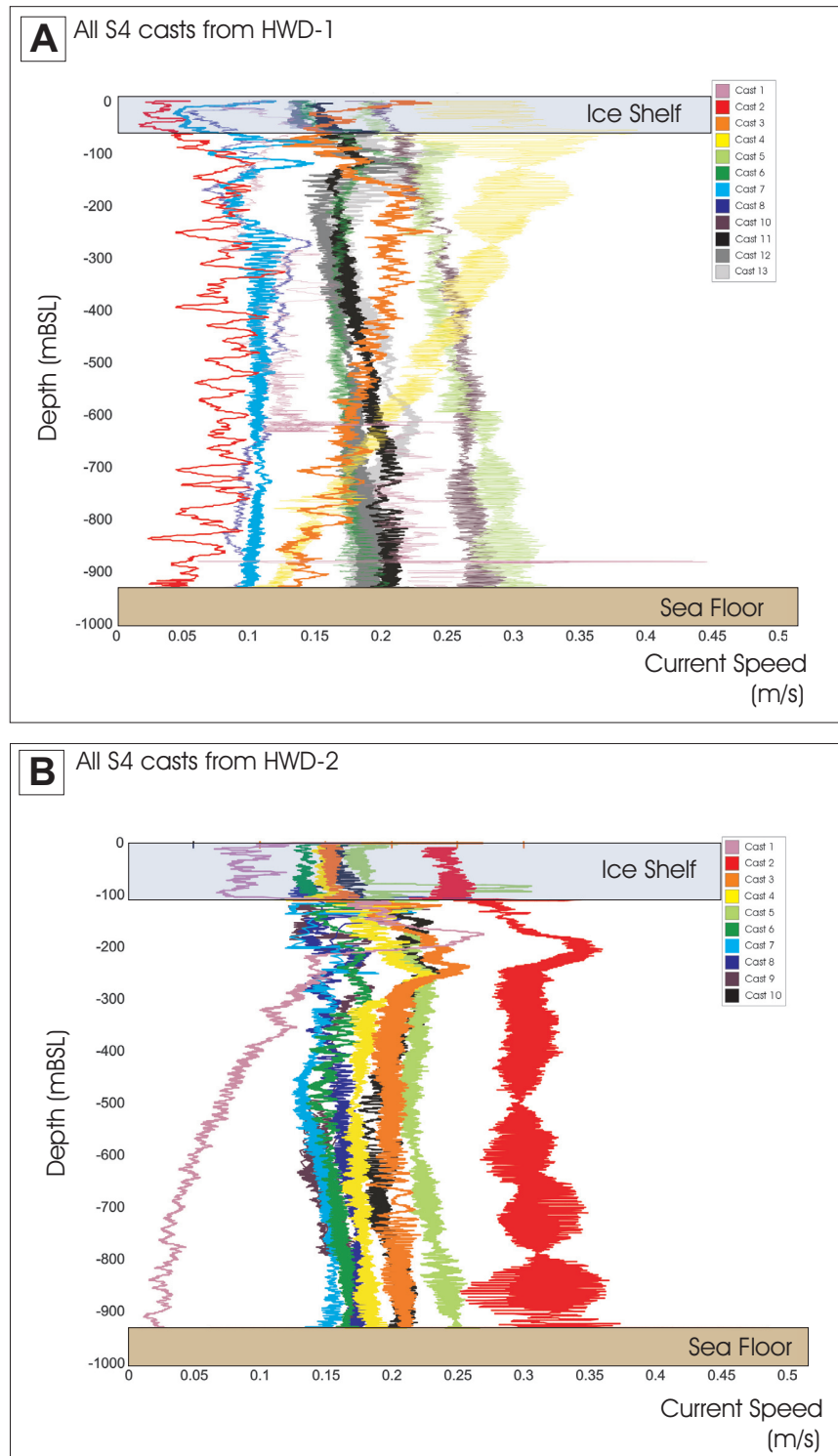


Figure 7: Current speed data from every cast at (A) HWD-1 and (B) HWD-2. This demonstrates that the selected casts, Cast 6 at Site 1 and Casts 2 and 4 at Site 2 are representative of the shape of the velocity profile as recorded by the S4 casts.

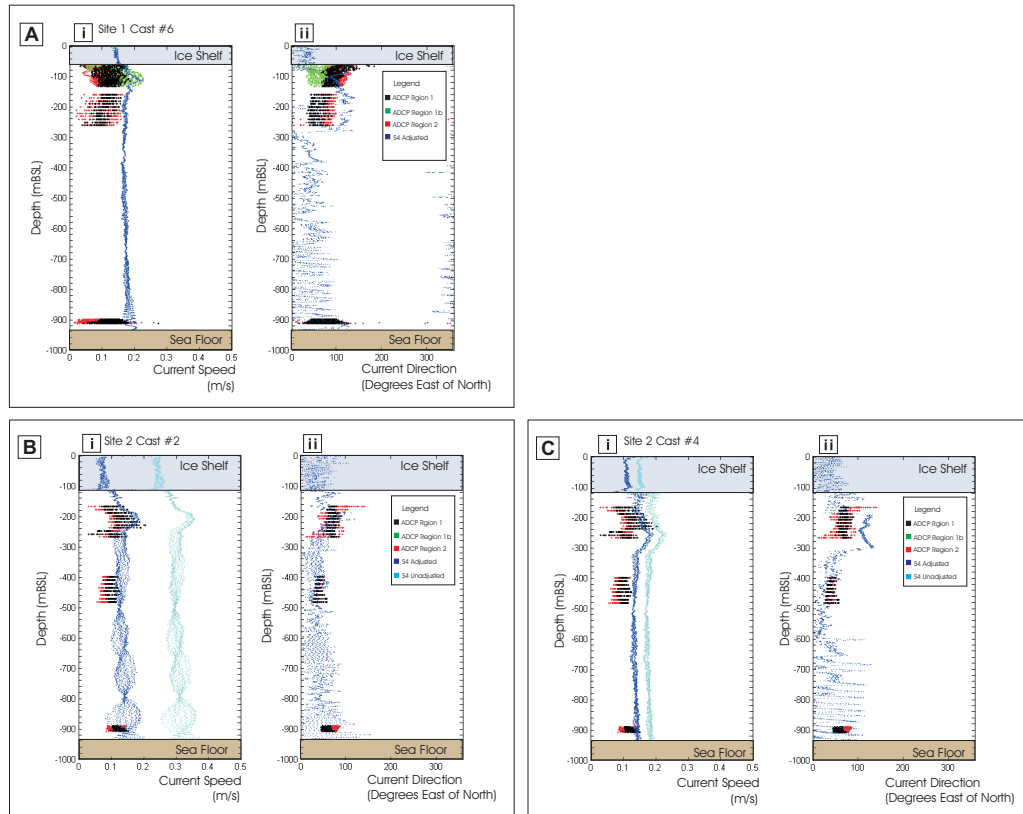


Figure 8: (i) Current speed and (ii) current direction data from representative S4 casts used to create maximum speed profiles. These data are overlaid with the appropriate ADCP data from the selected regions. Where necessary, an offset has been applied to the S4 current speed data in order to make it consistent with the more reliable ADCP data. No offset has been applied to (A) Site 1, Cast 6 while offsets of  $0.17 \text{ ms}^{-1}$  and  $0.04 \text{ ms}^{-1}$  were applied to (B) Site 2, Cast 2 and (C) Site 2, Cast 4 respectively.

in the manner described above for speed, acceptable agreement between the instruments were observed for the whole period of the mooring.

### **1.5 Resultant Profiles**

To create a synthetic velocity profile, the ‘representative’ S4 casts with the appropriate speed offset applied were plotted, and a smoothed curve constructed encompassing the maximum speeds at each depth. These were then read off every 10 metres of depth, creating a series of well-spaced data points.

### **1.6 Acknowledgement**

The data collection and analysis was funded by NZ FORST Paleoclimate grant to Prof. Peter Barrett, Antarctic research centre, Victoria University of Wellington: K042 Antarctic field program 2002/2003, (Natalie Robinson, part of an MSc scholarship) and Antarctica NZ contract with VUW (Alex Pyne, ANDRILL Drilling Science Coordinator).

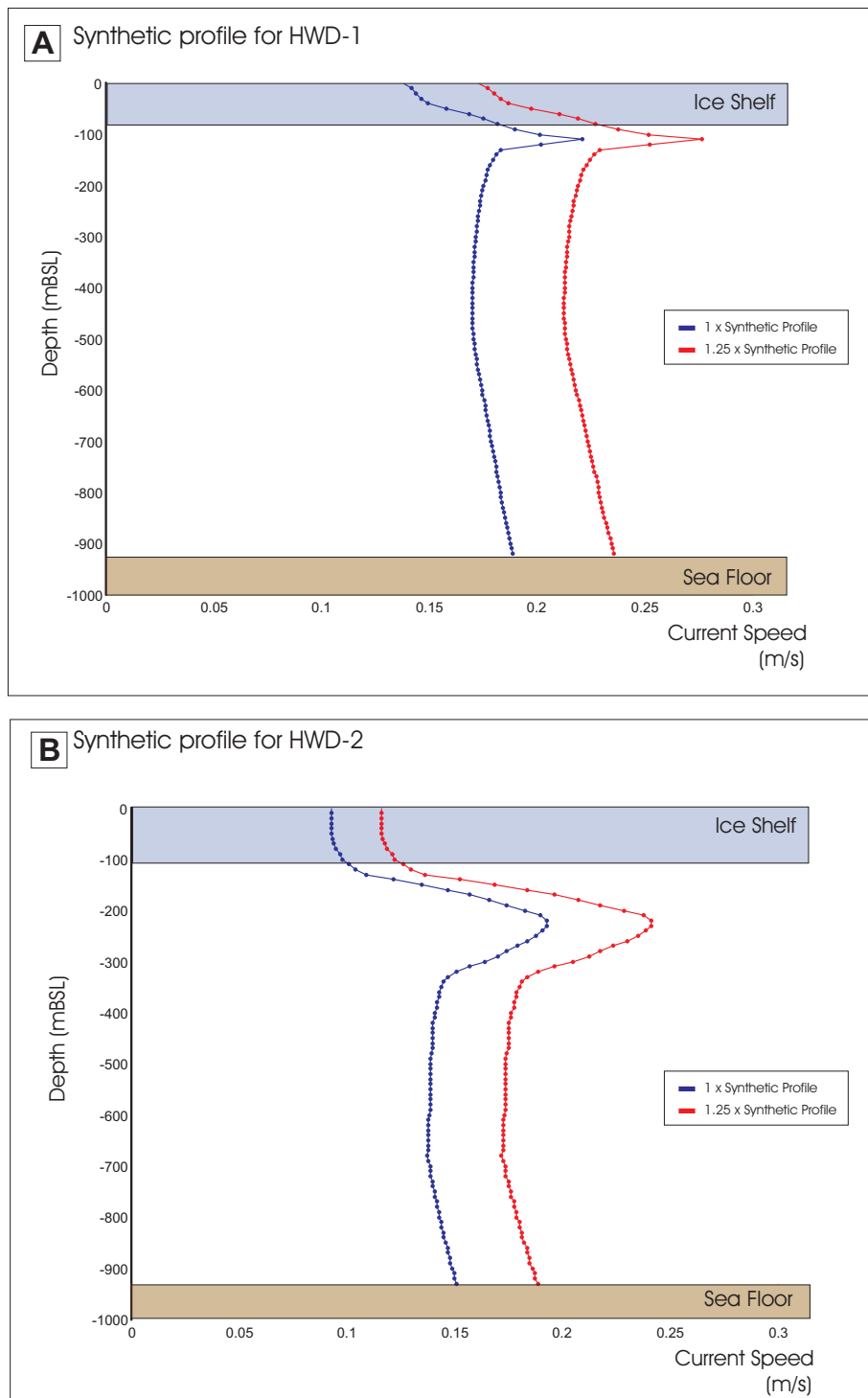


Figure 9: Synthetic maximum speed profiles created for (A) HWD-1 and (B) HWD-2 from ADCP and S4 data. x 1 profiles are shown in blue, with x 1.25 in red.

## 2 Granite Harbour: Water Current Velocity Profiles from ADCP data

### 2.1 Background

Current velocity survey has been undertaken on behalf of Dr Ross Powell (Northern Illinois University) by McMurdo Station Crary Lab staff in the 2000/2001 season as part of site survey preparation for ANDRILL. Moorings were deployed at two sites in Granite Harbour from the sea ice during the period 5 December 2000 to 4 January 2001, figure 10. The GH-1 site is approximately 5 km north of Couloir Cliffs in approximately 800 m of water. The GH-2 site is in the mid-outer harbour in approximately 900 to 950 m of water.

### 2.2 Moorings

Each mooring (GH-1 and GH-2) was in the water for approximately 15 and 14 days respectively and consisted of three downward looking ADCP RDI sentinel instruments set just below the sea ice, at 250 m and at 500m depth. An S4 instrument was also set on the mooring just above the ADCP at 250 m, figure 12.

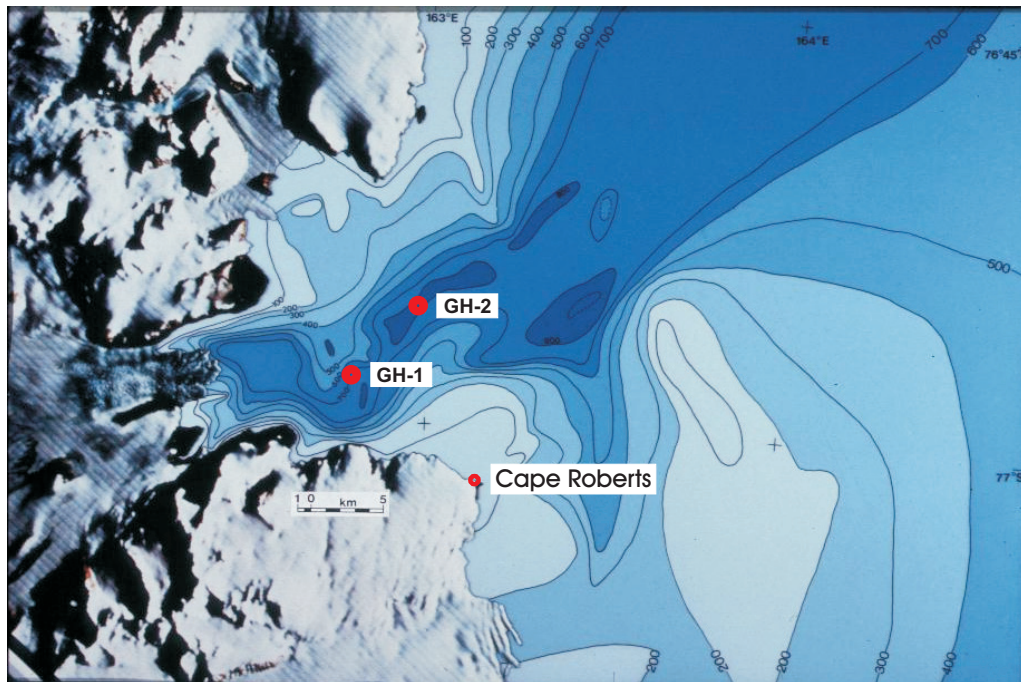


Figure 10: Bathymetry map of Granite Harbour area (*Pyne unpublished*) showing locations of moorings set in sea ice at GH-1, GH-2.

STATION	LATITUDE*	LONGITUDE*	GEOID ELEVATION <sup>+</sup>	CORR- ECTION	MSL
ROB-0	77.0356590 S	163.1782096 E	-53.643	-55.310	1.667
GH1-339 (12 - 05 - 00)	76.9750482 S	162.7503070 E	-55.274	-55.461	0.187
GH1-354 12 - 20 - 00	76.9750252 S	162.7505520 E	-57.236	-55.462	-1.774
GH2-355 12 - 21 - 00	76.9338021 S	162.9506571 E	-57.260	-55.693	-1.567
GH2-004 01 - 04 - 01	76.9338086 S	162.9506676 E	-54.871	-55.693	0.822

Table 1: MACKAY SEA VALLEY SEA ICE MOTION STUDY - The sea ice positions of the two different sites (GH-1 and GH-2) were checked at two different times to determine lateral sea ice motion: GH1-339, GH1-354 and GH2-355, GH2-004 where -xxx is day of the year.

\* Coordinates are in decimal degrees, WGS-84

<sup>+</sup> Elevations are 40-70 cm too high. (Source: Chuck Kurnik, UNAVCO, 03 - 13 - 01)

The period of each mooring encompasses the maximum tidal period range as indicated in figure 11, from the tide gauge at Cape Roberts 10 - 13 km away.

The analysis of the mooring data generally follows the methodology detailed in section one for the McMurdo ice Shelf except that no S4 casts are available to “fill in the gaps” between the ADCP data. The setup data for three sentinel instruments and two S4 are shown in Appendix 2, Tables 12 and 13.

### 2.2.1 Magnetic deviation

Both the ADCP and S4 data were recorded without any correction for the magnetic deviation in the area. A value of  $+150^{\circ}$  (east of North) has been applied to the processed directional data for all instruments to correct magnetic azimuth to true azimuth. The resulting current direction measured by the S4s and the uppermost data bin of the ADCP moored at 250 m depth agree within  $\pm 10$  degrees at both sites.

For each site the ADCP speed and directions are shown in figure 13 and figure 14. To develop the synthetic maximum current profile, two periods of maximum flow for each

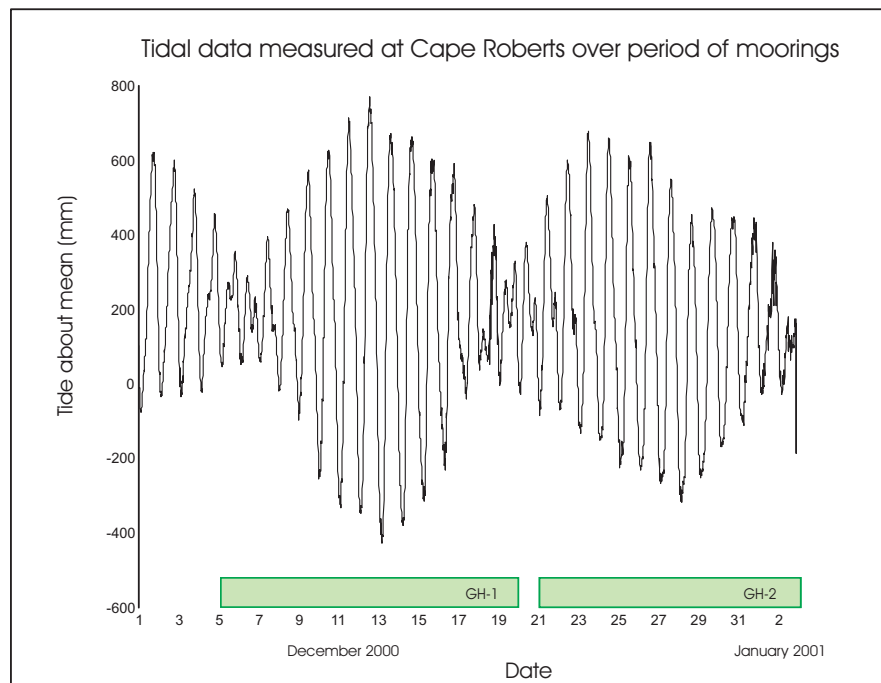


Figure 11: Tidal data measured at Cape Roberts (*Pyne personal communication*). Tides corresponding to the timing of the moorings are shown.

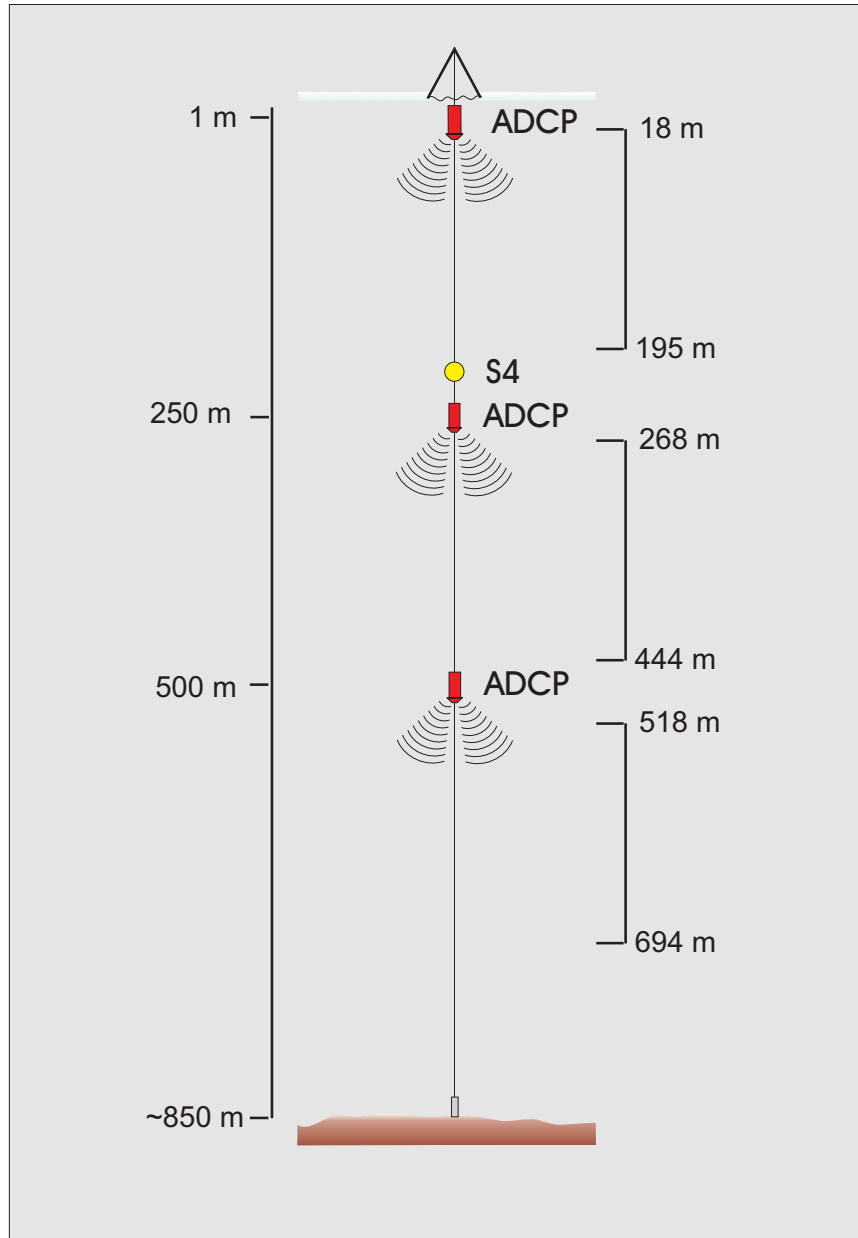


Figure 12: Diagram showing the mooring array at both GH-1 and GH-2 with 3 ADCPs and one S4 instrument. The scale to the left indicates the depth below sea level at which each instrument was deployed. The ranges to the right indicate the sections of the water column observed by the ADCPs.

instrument were selected and plotted against depth for the two sites, see figure 15. The synthetic water profiles were then constructed and are shown in figure 16. The calculated data is shown in Appendix 2, tables 10 and 11.

### **2.3 Acknowledgement**

The data collection was funded by NSF grant OPP-0003607 to Prof. Ross Powell, Northern Illinois University. The data analysis was funded by NZ FORST Paleoclimate grant to Prof. Peter Barrett, Victoria University of Wellington, (Natalie Robinson, part of an MSc scholarship) and Antarctica NZ contract with VUW (Alex Pyne, ANDRILL Drilling Science Coordinator).

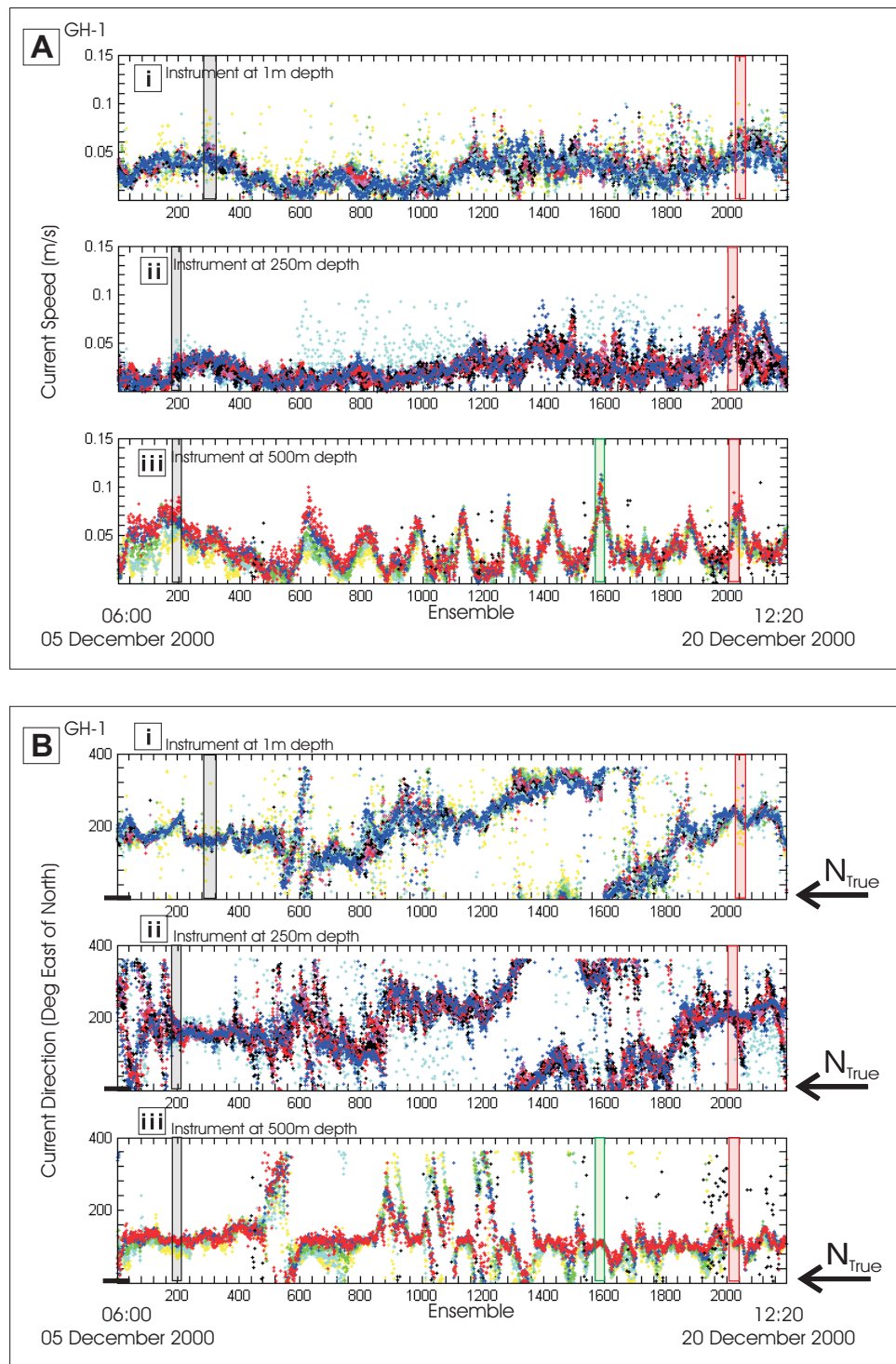


Figure 13: (A) Current speed and (B) current direction data from the three ADCP instruments at GH-1. Time series (i) is from the instrument at 1m BSL, (ii) 250m BSL and (iii) 500m BSL. Also shown are the short periods from which data was extracted for construction of maximum current profiles - Black, region 1, Green, region 1b, Red, region 2. The maximum current speeds at each depth were captured, so the regions were not quite synchronous through the water column.

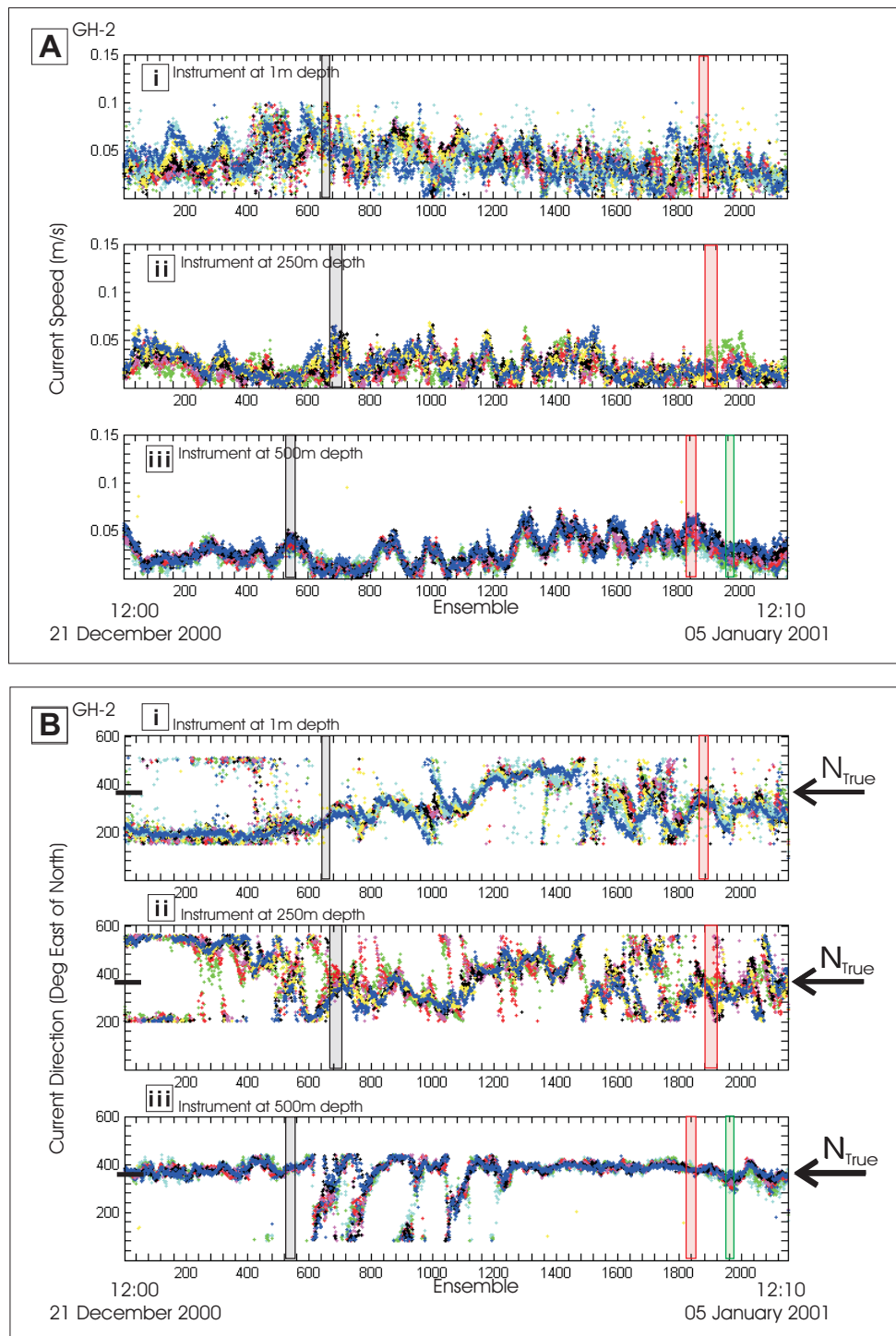


Figure 14: (A) Current speed and (B) current direction data from the three ADCP instruments at GH-2. Time series (i) is from the instrument at 1m BSL, (ii) 250m BSL and (iii) 500m BSL. Also shown are the short periods from which data was extracted for construction of maximum current profiles - Black, region 1, Red, region 2, Green, region 2b. The maximum current speeds at each depth were captured, so the regions were not quite synchronous through the water column.

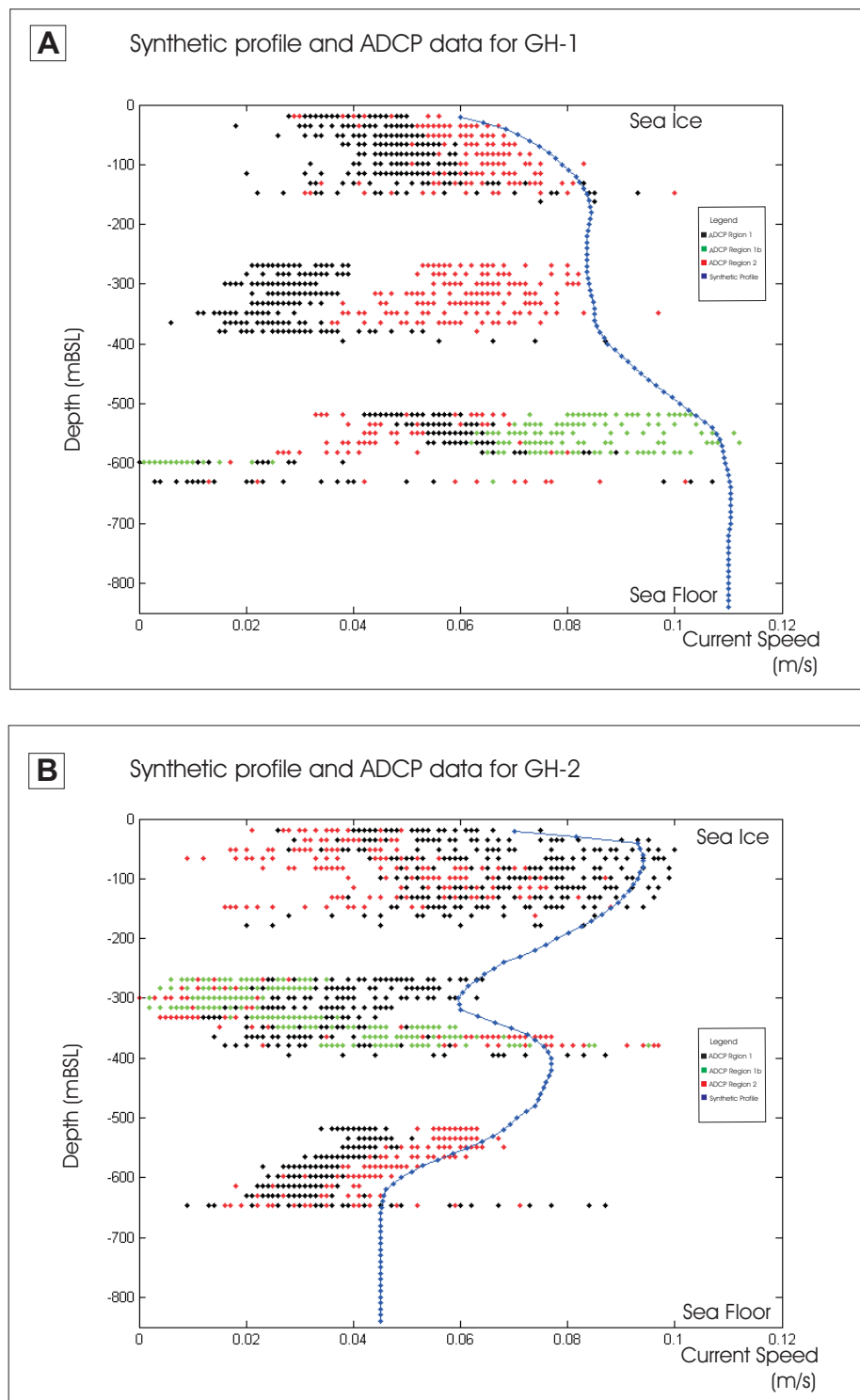


Figure 15: Synthetic maximum speed profiles created for (A) GH-1 and (B) GH-2 shown overlaid with the ADCP data.

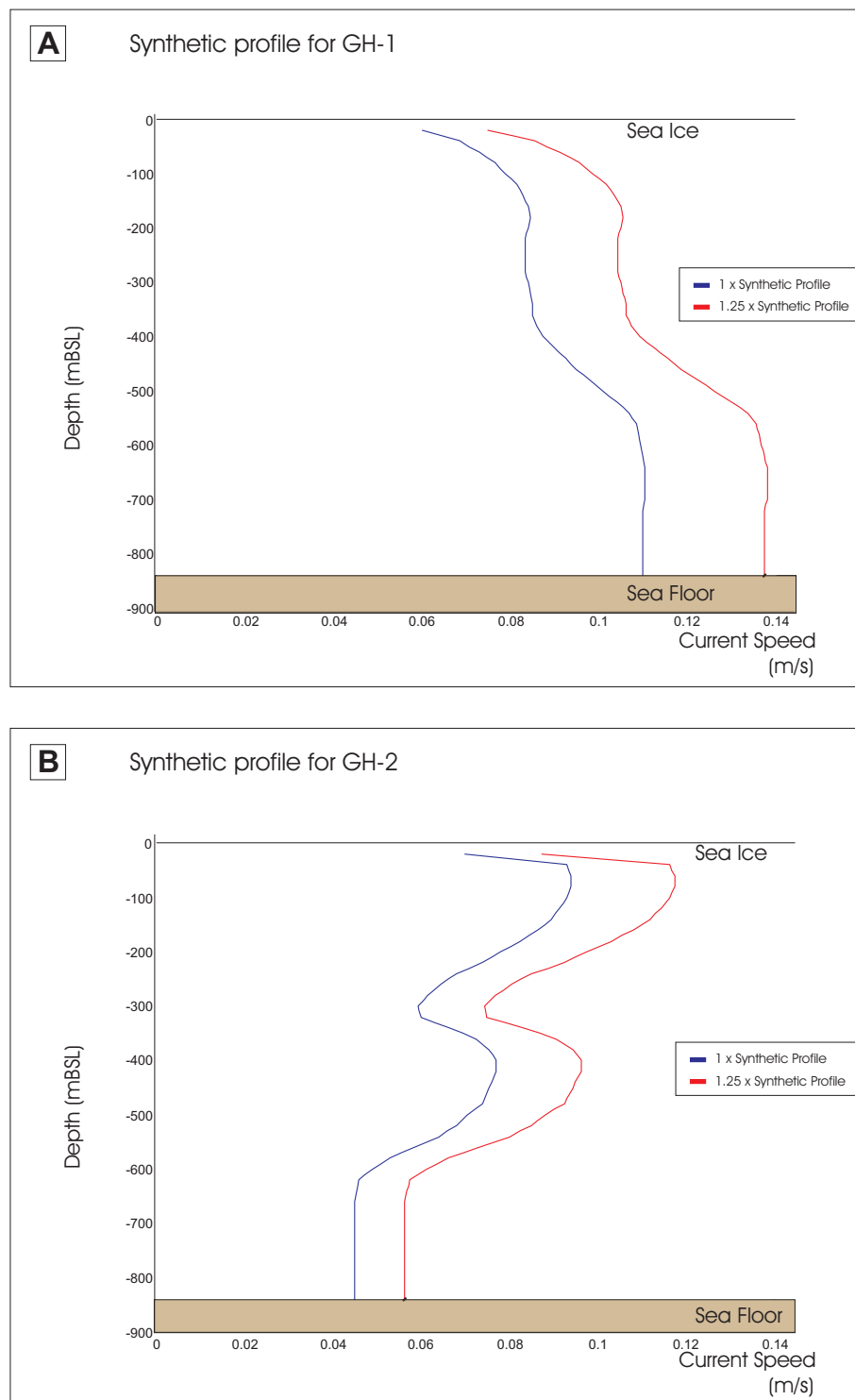


Figure 16: Synthetic maximum speed profiles created for (A) GH-1 and (B) GH-2 from ADCP data. x 1 profiles are shown in blue, with x 1.25 in red.

### 3 Appendices

#### 3.1 Appendix 1 - Windless Bight

<b>HWD-1 Instrument</b>	RDI Sentinel 327	InterOcean S4 SN 04911042	RDI Sentinel 600	RDI Navigator
<b>Water Depth</b>	138.0m	143.0m	149.4m	898m
<b>System Frequency</b>	307.2 kHz		307.2 kHz	614.4 kHz
<b>1st Bin Below Instrument</b>	+6.03m		-12.05m	-1.44m
<b>Bin Size</b>	4.00m		10.00m	0.5m
<b>No. of bins</b>	30		13	90
<b>Time per Ping</b>	3.00 sec		3.00 sec	0.62 sec
<b>Time (S4)</b>		0.5 sec		
<b>Pings per ensemble</b>	200		200	175
<b>Average Count (S4)</b>		Did not Operate		
<b>On Time (S4)</b>				
<b>Cycle Time (S4)</b>				
<b>Average Ensemble Interval</b>	00 : 10 : 00.00		00 : 10 : 00.00	00 : 05 : 00.00
<b>Start Date (Ensemble)</b>	18-01-2003		18-01-2003	18-01-2003
<b>Time</b>	06 : 00 : 00.00		06 : 00 : 00.00	06 : 00 : 00.00
<b>End Date (Ensemble)</b>	22-01-2003		22-01-2003	22-01-2003
<b>Time</b>	02 : 10 : 00.00		02 : 10 : 00.00	2 : 05 : 00.00

Table 2: Windless Bight Site HWD-1; ADCP and S4 setup data

<b>HWD-2 Instrument</b>	RDI Sentinel 327	RDI Sentinel 600	InterOcean S4 SN 08291863	RDI Navigator
<b>Water Depth</b>	155.9m	496.4m	501.4m	887m
<b>System Frequency</b>	307.2 kHz	307.2kHz		614.4 kHz
<b>1st Bin Below Instrument</b>	-12.09m	14.13m		-2.99m
<b>Bin Size</b>	10.00m	12.00m		2.00m
<b>No. of bins</b>	14	13		20
<b>Time per Ping</b>	2.00 sec	2.00 sec		0.62 sec
<b>Time (S4)</b>			0.5 sec	
<b>Pings per ensemble</b>	150	150		130
<b>Average Count (S4)</b>			120	
<b>On Time (S4)</b>			00 : 01 : 00	
<b>Cycle Time (S4)</b>			00 : 10 : 00	
<b>Average Ensemble Interval</b>	00 : 05 : 00.00	00 : 05 : 00.00		00 : 05 : 00.00
<b>Start Date (Ensemble)</b>	30-01-2003	30-01-2003	30-01-2003	30-01-2003
<b>Time</b>	07 : 00 : 00.00	07 : 00 : 00.00	07 : 00 : 00.00	07 : 00 : 00.00
<b>End Date (Ensemble)</b>	01-02-2003	01-02-2003	01-02-2003	01-02-2003
<b>Time</b>	11 : 10 : 00.00	10 : 55 : 00.00	11 : 30 : 00.00	10 : 50 : 00.00

Table 3: Windless Bight Site HWD-2; ADCP and S4 setup data

Cast No.	Start	Mid	End
<b>1</b>	3607	12680	38878
<b>2</b>	2092	5389	8654
<b>3</b>	2130	8511	10530
<b>4</b>	1909	5974	11996
<b>5</b>	1397	9526	15035
<b>6</b>	1161	7574	11620
<b>7</b>	2775	9355	13308
<b>8</b>	3053	9650	13832
<b>9</b>	DID	NOT	OPERATE
<b>10</b>	1572	8343	12834
<b>11</b>	2153	8761	13408
<b>12</b>	2302	9330	13631
<b>13</b>	1226	7786	12017

Table 4: Sample numbers defining ‘Up’ and ‘Down’ casts at HWD-1

Cast No.	Start	Mid	End
<b>1</b>	2800	11375	15422
<b>2</b>	1836	10230	14807
<b>3</b>	1461	10290	15147
<b>4</b>	1492	9441	14036
<b>5</b>	2010	10447	15090
<b>6</b>	1885	9738	14363
<b>7</b>	1576	9228	13948
<b>8</b>	2225	9581	14614
<b>9</b>	1787	10083	15044
<b>10</b>	1409	9745	13866

Table 5: Sample numbers defining ‘Up’ and ‘Down’ casts at HWD-2

<b>Site 1</b>		Depth = 933m		
<b>Cast No.</b>	Down (min)	Av Vel Down $ms^{-1}$	Up (min)	Av Vel Up $ms^{-1}$
2	26	0.598	17	0.915
3	50	0.311	16	0.972
4	33	0.471	49	0.317
5	55	0.283	45	0.346
6	51	0.305	33	0.471
7	52	0.299	32	0.486
8	51	0.305	32	0.486
10	54	0.288	33	0.471
11	52	0.305	33	0.471
12	52	0.305	33	0.471
13	52	0.305	32	0.486

Table 6: Vertical velocity of S4 instrument through the water column at HWD-1

<b>Site 2</b>		Depth = 870m		
<b>Cast No.</b>	Down (min)	Av Vel Down $ms^{-1}$	Up (min)	Av Vel Up $ms^{-1}$
1	62	0.234	30	0.483
2	60	0.242	31	0.468
3	64	0.227	37	0.392
4	59	0.246	32	0.453
5	61	0.238	34	0.426
6	58	0.250	32	0.453
7	58	0.250	32	0.453
8	55	0.264	32	0.453
9	62	0.234	32	0.453
10	60	0.242	32	0.453

Table 7: Vertical velocity of S4 instrument through the water column at HWD-2

Depth m	Speed ms <sup>-1</sup>						
0	0.1385	240	0.1735	480	0.1704	720	0.1797
10	0.1418	250	0.1732	490	0.1706	730	0.1801
20	0.1442	260	0.1728	500	0.1708	740	0.1806
30	0.1466	270	0.1725	510	0.1711	750	0.1811
40	0.1495	280	0.1722	520	0.1714	760	0.1815
50	0.1580	290	0.1721	530	0.1717	770	0.1820
60	0.1685	300	0.1719	540	0.1721	780	0.1825
70	0.1753	310	0.1717	550	0.1724	790	0.1828
80	0.1817	320	0.1714	560	0.1728	800	0.1831
90	0.1900	330	0.1712	570	0.1732	810	0.1833
100	0.2014	340	0.1711	580	0.1737	820	0.1837
110	0.2212	350	0.1709	590	0.1741	830	0.1842
120	0.2017	360	0.1708	600	0.1745	840	0.1847
130	0.1833	370	0.1706	610	0.1749	850	0.1851
140	0.1813	380	0.1705	620	0.1755	860	0.1857
150	0.1797	390	0.1704	630	0.1760	870	0.1862
160	0.1784	400	0.1703	640	0.1764	880	0.1867
170	0.1774	410	0.1703	650	0.1768	890	0.1872
180	0.1766	420	0.1702	660	0.1772	900	0.1876
190	0.1760	430	0.1702	670	0.1777	910	0.1881
200	0.1753	440	0.1701	680	0.1780	920	0.1887
210	0.1747	450	0.1701	690	0.1783		
220	0.1743	460	0.1702	700	0.1788		
230	0.1738	470	0.1703	710	0.1792		

Table 8: Synthetic Profile for Windless Bight site HWD-1

Depth m	Speed ms <sup>-1</sup>						
0	0.0930	240	0.1910	480	0.1395	720	0.1390
10	0.0930	250	0.1880	490	0.1390	730	0.1400
20	0.0930	260	0.1840	500	0.1390	740	0.1400
30	0.0930	270	0.1790	510	0.1390	750	0.1410
40	0.0930	280	0.1740	520	0.1390	760	0.1410
50	0.0930	290	0.1700	530	0.1390	770	0.1420
60	0.0935	300	0.1640	540	0.1390	780	0.1420
70	0.0940	310	0.1570	550	0.1390	790	0.1430
80	0.0950	320	0.1510	560	0.1390	800	0.1430
90	0.0970	330	0.1470	570	0.1390	810	0.1440
100	0.0980	340	0.1450	580	0.1390	820	0.1440
110	0.1010	350	0.1440	590	0.1390	830	0.1450
120	0.1040	360	0.1430	600	0.1385	840	0.1450
130	0.1090	370	0.1430	610	0.1380	850	0.1460
140	0.1220	380	0.1420	620	0.1380	860	0.1470
150	0.1350	390	0.1420	630	0.1380	870	0.1470
160	0.1470	400	0.1410	640	0.1380	880	0.1480
170	0.1570	410	0.1410	650	0.1380	890	0.1480
180	0.1660	420	0.1400	660	0.1380	900	0.1490
190	0.1740	430	0.1400	670	0.1380	910	0.1500
200	0.1830	440	0.1400	680	0.1375	920	0.1500
210	0.1900	450	0.1400	690	0.1380	930	0.1510
220	0.1930	460	0.1400	700	0.1390		
230	0.1930	470	0.1400	710	0.1390		

Table 9: Synthetic Profile for Windless Bight site HWD-2

Depth m	Speed cms <sup>-1</sup>						
		220	0.0835	430	0.0913	640	0.1105
20	0.0600	230	0.0835	440	0.0925	650	0.1105
30	0.0643	240	0.0835	450	0.0938	660	0.1105
40	0.0685	250	0.0835	460	0.0950	670	0.1105
50	0.0708	260	0.0835	470	0.0965	680	0.1105
60	0.0730	270	0.0835	480	0.0980	690	0.1105
70	0.0748	280	0.0835	490	0.0995	700	0.1105
80	0.0765	290	0.0838	500	0.1010	710	0.1103
90	0.0778	300	0.0840	510	0.1025	720	0.1100
100	0.0790	310	0.0843	520	0.1040	730	0.1100
110	0.0803	320	0.0845	530	0.1055	740	0.1100
120	0.0815	330	0.0848	540	0.1070	750	0.1100
130	0.0823	340	0.0850	550	0.1078	760	0.1100
140	0.0830	350	0.0850	560	0.1085	770	0.1100
150	0.0835	360	0.0850	570	0.1088	780	0.1100
160	0.0840	370	0.0855	580	0.1090	790	0.1100
170	0.0843	380	0.0860	590	0.1093	800	0.1100
180	0.0845	390	0.0868	600	0.1095	810	0.1100
190	0.0843	400	0.0875	610	0.1098	820	0.1100
200	0.0840	410	0.0888	620	0.1100	830	0.1100
210	0.0838	420	0.0900	630	0.1103	840	0.1100

Table 10: Synthetic Profile for site GH-1

Depth m	Speed cms <sup>-1</sup>						
		220	7.400	430	7.650	640	4.550
20	7.000	230	7.100	440	7.600	650	4.525
30	8.150	240	6.800	450	7.550	660	4.525
40	9.300	250	6.625	460	7.500	670	4.500
50	9.350	260	6.450	470	7.450	680	4.500
60	9.400	270	6.300	480	7.400	690	4.500
70	9.400	280	6.150	490	7.225	700	4.500
80	9.400	290	6.050	500	7.050	710	4.500
90	9.350	300	5.950	510	6.925	720	4.500
100	9.300	310	5.975	520	6.800	730	4.500
110	9.225	320	6.000	530	6.600	740	4.500
120	9.150	330	6.325	540	6.400	750	4.500
130	9.050	340	6.650	550	6.125	760	4.500
140	8.950	350	6.950	560	5.850	770	4.500
150	8.800	360	7.250	570	5.575	780	4.500
160	8.650	370	7.400	580	5.300	790	4.500
170	8.450	380	7.550	590	5.100	800	4.500
180	8.250	390	7.625	600	4.900	810	4.500
190	8.025	400	7.700	610	4.750	820	4.500
200	7.800	410	7.700	620	4.600	830	4.500
210	7.600	420	7.700	630	4.575	840	4.500

Table 11: Synthetic Profile for site GH-2

3.2 Appendix 2 - Granite Harbour

<b>GH-1 Instrument</b>	76.9750482 S RDI Sentinel	InterOcean S4 SN 08291863	162.7503070E RDI Sentinel	RDI Sentinel
<b>Water Depth</b>	1m	250m	250m	500m
<b>System Frequency</b>	307.2 kHz		307.2kHz	307.2KHz
<b>1st Bin Below Instrument</b>	-17.76m		-17.75m	-17.74m
<b>Bin Size</b>	16.00m		16.00m	16.00m
<b>No. of bins</b>	11		11	11
<b>Time per Ping</b>	9.23 sec		9.23 sec	9.23 sec
<b>Time (S4)</b>		0.5 sec		
<b>Pings per ensemble</b>	65		65	65
<b>Average Count (S4)</b>		120		
<b>On Time (S4)</b>		00 : 03 : 00		
<b>Cycle Time (S4)</b>		00 : 12 : 00		
<b>Average Ensemble Interval</b>	00 : 10 : 00.00		00 : 10 : 00.00	00 : 10 : 00.00
<b>Start Date (Ensemble)</b>	5-12-2000	5-12-2000	5-12-2000	5-12-2000
<b>Time</b>	06 : 00 : 00.00	06 : 00 : 00.00	06 : 00 : 00.00	06 : 00 : 00.00
<b>End Date (Ensemble)</b>	20-12-2000	22-12-2000	20-12-2000	20-12-2000
<b>Time</b>	14 : 20 : 00.00	07 : 39 : 00.00	15 : 10 : 00.00	17 : 20 : 00.00

Table 12: Granite Harbour Site GH-1; ADCP and S4 setup data

<b>GH-1</b>	76.9750482 S		162.7503070E	
<b>Instrument</b>	RDI Sentinel	InterOcean S4 SN 08291863	RDI Sentinel	RDI Sentinel
<b>Water Depth</b>	1m	250m	250m	500m
<b>System Frequency</b>	307.2 kHz		307.2kHz	307.2KHz
<b>1st Bin Below Instrument</b>	-17.76m		-17.75m	-17.74m
<b>Bin Size</b>	16.00m		16.00m	16.00m
<b>No. of bins</b>	11		11	11
<b>Time per Ping</b>	9.23 sec		9.23 sec	9.23 sec
<b>Time (S4)</b>		0.5 sec		
<b>Pings per ensemble</b>	65		65	65
<b>Average Count (S4)</b>		120		
<b>On Time (S4)</b>		00 : 03 : 00		
<b>Cycle Time (S4)</b>		00 : 12 : 00		
<b>Average Ensemble Interval</b>	00 : 10 : 00.00		00 : 10 : 00.00	00 : 10 : 00.00
<b>Start Date (Ensemble)</b>	21-12-2000	21-12-2000	21-12-2000	21-12-2000
<b>Time</b>	12 : 00 : 00.00	12 : 00 : 00.00	12 : 00 : 00.00	12 : 00 : 00.00
<b>End Date (Ensemble)</b>	5-01-2001	5-01-2001	5-01-2001	5-01-2001
<b>Time</b>	15 : 20 : 00.00	16 : 51 : 00.00	15 : 30 : 00.00	15 : 40 : 00.00

Table 13: Granite Harbour Site GH-2; ADCP and S4 setup data

# Appendix C

## Index of model simulations on CD

Experiment Identifier	Short Description
Standard Experiment	7 years, standard settings, flat seafloor configuration
Experiment 2	5 years, $\Delta Y = 3,000$ m
Experiment 3	5 years, $\Delta Y = 4,000$ m
Experiment 4	5 years, $\Delta Y = 10,000$ m
Experiment 5	5 years, $\Delta T = 5$ minutes
Experiment 6	5 years, $\Delta T = 15$ minutes
Experiment 7	5 years, Low diffusion, normal boundary restoring
Experiment 8	5 years, Low diffusion, low boundary restoring
Experiment 9	5 years, Sediment supplied to all depths
Experiment 10	5 years, Settling velocities $5 \times 10^{-4}$ , $1 \times 10^{-4}$ , $5 \times 10^{-5}$ $1 \times 10^{-5}$ m s <sup>-1</sup>
Experiment 11	5 years, Settling velocities $5 \times 10^{-6}$ , $1 \times 10^{-6}$ , $5 \times 10^{-7}$ $1 \times 10^{-7}$ m s <sup>-1</sup>
Experiment 12	5 years, Settling velocities $5 \times 10^{-8}$ , $1 \times 10^{-8}$ , $5 \times 10^{-9}$ $1 \times 10^{-9}$ m s <sup>-1</sup>
Experiment 13	7 years, SF-Basin configuration
Experiment 14	7 years, SF-Sloped-In configuration
Experiment 15	7 years, SF-Sloped-Out configuration

# Bibliography

- Apel, J., *Principles of Ocean Physics*, 634. Academic Press, London, 1987.
- Barrett, P., The Antarctic paleoenvironment through Cenozoic times. *Terra Antarctica*, volume 3 (2), 103 – 119, 1996.
- Barrett, P., Carter, L., Dunbar, G., Dunker, E., Giorgetti, G., Niessen, F., Nixdorf, U., Pyne, A., Riesselman, C., Robinson, N., Hollis, C., and Strong, P., *Oceanography and sedimentation beneath the McMurdo Ice Shelf in Windless Bight, Antarctica*. Number 25 in Antarctic Data Series, Antarctic Research Centre, Victoria University of Wellington, 2004.
- Barrett, P., Pyne, A., and Ward, B., Modern sedimentation in McMurdo Sound, Antarctica. In R. Oliver, P. James, and J. Jago, eds., *Antarctic Earth Science*, 550 – 554, Australian Academy of Science, 1983.
- Barry, J. P. and Dayton, P. K., Current patterns in McMurdo Sound, Antarctica and their relationship to local biotic communities. *Polar Biology*, volume 8, 367 – 376, 1988.
- Barry, J. P., Dayton, P. K., Dunbar, R., and Leventer-Reed, A. R., Winter oceanographic observations in McMurdo Sound, Antarctica. *Antarctic Journal of the United States*, volume 25 (5), 106 – 107, 1990.
- Blankenship, D., Morse, D., and Holt, J., An airborne radioglaciological survey of iceberg B15a on November 23, 2001. In *Conference Proceedings*, Fall, American Geophysical Union, 2002.
- Clough, J. W. and Hansen, B. L., The Ross Ice Shelf Project. *Science*, volume 203, 433 – 434, 1979.
- Courant, R., Friedrichs, K., and Lewy, H., Über die partiellen differenzgleichungen der mathematischen Physik. *Mathematische Annalen*, volume 100, 32 – 74, 1928.

- Davey, F., Ross Sea Bathymetry, 1:2 000 000, version 1. Institute of Geological and Nuclear Sciences Geophysical map 16, 2004.
- Domack, E. M., Jacobson, A., Erik, Shipp, S., and Anderson, J. B., Late Pleistocene - Holocene retreat of the West Antarctic ice sheet in the Ross Sea: Part 2 - Sedimentologic and stratigraphic signature. *Geological Society of America Bulletin*, volume 111 (10), 1999.
- Dunbar, R. B., Anderson, J. B., and Domack, E. W., Oceanographic influences on sedimentation along the Antarctic Continental Shelf. In S. Jacobs, ed., *Oceanology of the Antarctic Continental Shelf*, volume 43 of *Antarctic Research Series*, 291–312, American Geophysical Union, Washington, D.C, 1985.
- Dunbar, R. B. and Leventer, A. R., Sediment fluxes beneath fast ice: October 1986 through February 1987. *Antarctic Journal of the United States*, volume 22, 112– 115, 1987.
- Dunbar, R. B., Leventer, A. R., and Mucciarone, D., Water column sediment fluxes in the Ross Sea, Antarctica: Atmospheric and sea ice forcing. *Journal of Geophysical Research*, volume 103 (C13), 30,741–30,759, 1998.
- Dunbar, R. B., Mucciarone, D., and Leventer, A. R., Sediment-trap experiments in the central and western Ross Sea, January and February 1990. *Antarctic Journal of the United States*, volume 26, 115–117, 1991.
- Foldvik, A. and Kvinge, T., Conditional instability of sea water at the freezing point. *Deep-Sea Research*, volume 21, 169 – 174, 1974.
- Gibbs, R. J., Matthews, M. D., and Link, D. A., The relationship between sphere size and settling velocity. *Journal of Sedimentary Petrology*, volume 41 (1), 7–18, 1971.
- Gilmour, A., Hydrological heat and mass transport across the boundary of the ice shelf in McMurdo Sound, Antarctica. *New Zealand Journal of Geology and Geophysics*, volume 6, 402–22, 1963.
- Gilmour, A., McMurdo Sound hydrological observations, 1972-73. *New Zealand Journal of Marine and Freshwater Research*, volume 9 (1), 75–95, 1975.
- Gilmour, A. E., Ross Ice Shelf sea temperatures. *Science*, volume 203, 438 – 439, 1979.
- Goring, D. G. and Pyne, A., Observations of sea-level variability in Ross Sea, Antarctica. *New Zealand Journal of Marine and Freshwater Research*, volume 37, 241 – 249, 2003.

- Heath, R. A., Circulation and hydrology under the seasonal ice in McMurdo Sound, Antarctica. *New Zealand Journal of Marine and Freshwater Research*, volume 5 (3 and 4), 497 – 515, 1971.
- Heath, R. A., Circulation across the ice shelf edge in McMurdo Sound, Antarctica. In M. J. Dunbar, ed., *Polar Oceans Conference*, Polar Oceans, 129 – 148, McGill University, 1977.
- Hellmer, H. and Jacobs, S. S., Seasonal circulation under the eastern Ross Ice Shelf, Antarctica. *Journal of Geophysical Research*, volume 100 (C6), 10,873 – 10,885, 1995.
- Hellmer, H. and Olbers, D., A two-dimensional model for the thermohaline circulation under an ice shelf. *Antarctic Science*, volume 1 (4), 325 – 336, 1989.
- Hellmer, H. and Olbers, D., On the thermohaline circulation beneath the Filchner-Ronne Ice Shelves. *Antarctic Science*, volume 3 (4), 433 – 442, 1991.
- Hobbs, P., *Ice Physics*. Oxford University Press, 1974.
- Holland, D. M., Jacobs, S. S., and Jenkins, A., Modeling the ocean circulation beneath the Ross Ice Shelf. *Antarctic Science*, volume 15 (1), 13 – 23, 2003.
- Holland, D. M. and Jenkins, A., Modeling thermodynamic ice-ocean interactions at the base of an ice shelf. *Journal of Physical Oceanography*, volume 29, 1787 – 1800, 1999.
- Horgan, H., Naish, T., Bannister, S., Balfour, N., and Wilson, G., Seismic stratigraphy of the plio-pleistocene Ross Island flexural moat-fill: A prognosis for ANDRILL program drilling beneath McMurdo-Ross Ice Shelf. *Global and Planetary Change*, in press.
- Jacobs, S. S., Fairbanks, R. G., and Horibe, Y., Origin and evolution of water masses near the Antarctic Continental Margin: Evidence from  $\text{H}_2^{18}\text{O}$  /  $\text{H}_2^{16}\text{O}$  ratios in seawater. *Antarctic Research Series*, volume 43 (Oceanology of the Antarctic Continental Shelf), 59 – 85, 1985.
- Jacobs, S. S., Gordon, A. L., and Jr., J. L. A., Circulation and melting beneath the Ross Ice Shelf. *Science*, volume 203, 439 – 443, 1979.
- Jenkins, A., A one-dimensional model of ice shelf-ocean interaction. *Journal of Geophysical Research*, volume 96 (C11), 20,671 – 20,677, 1991.
- Langone, L., Dunbar, R. B., Mucciarone, D., Ravaioli, M., Meloni, R., and Nittrouer, C., Rapid sinking of biogenic material during the late austral summer in the Ross Sea,

- Antarctica. In G. R. DiTullio and R. B. Dunbar, eds., *Biogeochemistry of the Ross Sea*, Antarctic Research Series, American Geophysical Union, Washington, D.C., 2003.
- Leventer, A. R., Dunbar, R., and Allen, M., Ice thickness in McMurdo Sound. *Antarctic Journal of the United States*, volume 22, 94–95, 1987.
- Leventer, A. R. and Dunbar, R. B., Recent diatom record of McMurdo Sound, Antarctica: Implications for history of sea ice extent. *Paleoceanography*, volume 3 (3), 259 – 274, 1988.
- Lewis, E. L. and Perkin, R. G., The winter oceanography of the McMurdo Sound, Antarctica. In S. S. Jacobs, ed., *Oceanology of the Antarctic Continental Shelf*, volume 43 of *Antarctic Research Series*, 145 – 165, American Geophysical Union, Washington, D.C., 1985.
- Littlepage, J. L., Oceanographic investigations in McMurdo Sound, Antarctica. In G. H. Llano, ed., *Biology of the Antarctic Seas II*, volume 5 of *Antarctic Research Series*, American Geophysical Union, Washington, D.C., 1965.
- MacAyeal, D., Padman, L., Drinkwater, M., Fahnestock, M., Gotis, T., Gray, L., Kerman, B., Lazzara, M., Rignot, E., Scambos, T., and Stearns, C., Effects of rigid body collisions and tide-forced drift on large tabular icebergs of the Antarctic, 2002, unpublished Manuscript.
- MacAyeal, D. R., Evolution of tidally triggered meltwater plumes below ice shelves. In S. S. Jacobs, ed., *Oceanology of the Antarctic Continental Shelf*, volume 43 of *Antarctic Research Series*, 133 – 143, American Geophysical Union, Washington, D.C., 1985.
- Mitchell, W. M. and Bye, J. A. T., Observations in the boundary layer under the sea ice in McMurdo Sound. In S. S. Jacobs, ed., *Oceanology of the Antarctic Continental Shelf*, volume 43 of *Antarctic Research Series*, 167 – 176, American Geophysical Union, Washington, D.C., 1985.
- Rahmstorf, S., A fast and complete convection scheme for ocean models. *Ocean Modelling*, volume 101, 9 – 11, 1993.
- Robin, G. d. Q., Formation, flow and disintegration of ice shelves. *Journal of Glaciology*, volume 24, 259 – 271, 1979.

- Scheduikat, M. and Olbers, D., A one-dimensional mixed layer model beneath the Ross Ice Shelf with tidally induced vertical mixing. *Antarctic Science*, volume 2 (1), 29 – 42, 1990.
- Schwerdtfeger, W., The climate of the Antarctic. *World Survey of Climatology*, volume 14, 253 – 355, 1970.
- Welander, P., Thermal oscillations in a fluid heated from below and cooled to freezing from above. *Dynamics of Atmospheres and Oceans*, volume I, 215 – 223, 1977.
- Whillans, I. M. and Merry, C. J., Kinematics of the shear zone between Ross Ice Shelf and McMurdo Ice Shelf. Technical report, Byrd Polar Research Center, 1996.
- Williams, R. T. and Robinson, E. S., The ocean tide in the Southern Ross Sea. *Journal of Geophysical Research*, volume 85, 6689 – 6696, 1980.